HYDROGEN PRODUCTION ON BIMETALLIC CATALYSTS AND LOCAL ACIDITY INVESTIGATION OF ALUMINOSILICATES AND MESOPOROUS SILICA VIA SINGLE MOLECULE SPECTROSCOPY

by

JINGYI XIE

B.S., Beijing University of Chemical Technology, 2005
Ph.D., Beijing University of Chemical Technology, 2011

AN ABSTRACT OF A DISSERTATION

submitted in partial fulfillment of the requirements for the degree

DOCTOR OF PHILOSOPHY

Department of Chemical Engineering
College of Engineering

KANSAS STATE UNIVERSITY
Manhattan, Kansas

2016

Abstract

The autothermal reforming and partial oxidation of hexadecane via Pt/Ni bimetallic nanoparticles on various ceria-based supports were investigated. Nanoparticles with Pt/Ni molar ratios ranging from 0/100 to 10/90 were loaded on ceria-based supports including cerium oxide, gadolinium-doped cerium oxide and cerium-doped zirconium oxide. The effect of the Pt/Ni molar ratio and the promotional effect of the support were studied by comparing the hydrogen yield. TPR and XPS analysis showed that there was a strong interaction between Ni and the CeO_2-ZrO_2 support, which led to enhancement of catalyst performance when the Pt/Ni ratio was low. The strong interaction between Ni and CeO_2-ZrO_2 support was induced by the formation of a solid solution between NiO and ZrO_2. In the case of bimetallic catalysts loaded on Gd_2O_3-CeO_2, no significant improvement in the catalytic activity of autothermal reforming was achieved until the Pt/Ni ratio reached 10/90.

With C-snarf-1 as a pH-sensitive fluorescent probe, the local acidity on the surface of gradient aluminosilicate thin films and in the pore structure of mesoporous silicate films was explored. The single molecule emission ratio (I_{580}/I_{640}) of C-snarf-1 on the gradient aluminosilicate films showed similar results as previously reported for aluminosilicate mesoporous films. As the Al/Si ratio increases, the emission ratio declines, indicative of increased material acidity. In the case the mesoporous silicate films, much broader distributions of emission ratios were observed and are suggestive of significant heterogeneity in the pore structure of these films. The average emission ratio increased with a rise in pH until pH 6 or 7. A further rise in pH leads to a decline in emission ratio. Molecules with high mobility showed a narrow distribution and slightly lower average emission ratio when compared to data from all detected molecules. This observation implies a reduced heterogeneity for mesopores in which

the molecules rapidly diffuse. The narrow distribution and lower average value of emission ratio at low pH, combined with the decrease in emission ratio induced by an increase in ionic strength may further indicate that the interaction between dye molecules and the pore surface impacts the emission ratio of the dye molecules.

HYDROGEN PRODUCTION ON BIMETALLIC CATALYSTS AND LOCAL ACIDITY INVESTIGATION OF ALUMINOSILICATES AND MESOPOROUS SILICA VIA SINGLE MOLECULE SPECTROSCOPY

by

JINGYI XIE

B.S., Beijing University of Chemical Technology, 2005
Ph.D., Beijing University of Chemical Technology, 2011

A DISSERTATION

submitted in partial fulfillment of the requirements for the degree

DOCTOR OF PHILOSOPHY

Department of Chemical Engineering
College of Engineering

KANSAS STATE UNIVERSITY
Manhattan, Kansas

2016

Approved by:

Major Professor
Keith L. Hohn

Copyright

Abstract

The autothermal reforming and partial oxidation of hexadecane via Pt/Ni bimetallic nanoparticles on various ceria-based supports were investigated. Nanoparticles with Pt/Ni molar ratios ranging from 0/100 to 10/90 were loaded on ceria-based supports including cerium oxide, gadolinium-doped cerium oxide and cerium-doped zirconium oxide. The effect of the Pt/Ni molar ratio and the promotional effect of the support were studied by comparing the hydrogen yield. TPR and XPS analysis showed that there was a strong interaction between Ni and the CeO_2-ZrO_2 support, which led to enhancement of catalyst performance when the Pt/Ni ratio was low. The strong interaction between Ni and CeO_2-ZrO_2 support was induced by the formation of a solid solution between NiO and ZrO_2. In the case of bimetallic catalysts loaded on Gd_2O_3-CeO_2, no significant improvement in the catalytic activity of autothermal reforming was achieved until the Pt/Ni ratio reached 10/90.

With C-snarf-1 as a pH-sensitive fluorescent probe, the local acidity on the surface of gradient aluminosilicate thin films and in the pore structure of mesoporous silicate films was explored. The single molecule emission ratio (I_{580}/I_{640}) of C-snarf-1 on the gradient aluminosilicate films showed similar results as previously reported for aluminosilicate mesoporous films. As the Al/Si ratio increases, the emission ratio declines, indicative of increased material acidity. In the case the mesoporous silicate films, much broader distributions of emission ratios were observed and are suggestive of significant heterogeneity in the pore structure of these films. The average emission ratio increased with a rise in pH until pH 6 or 7. A further rise in pH leads to a decline in emission ratio. Molecules with high mobility showed a narrow distribution and slightly lower average emission ratio when compared to data from all detected molecules. This observation implies a reduced heterogeneity for mesopores in which

the molecules rapidly diffuse. The narrow distribution and lower average value of emission ratio at low pH, combined with the decrease in emission ratio induced by an increase in ionic strength may further indicate that the interaction between dye molecules and the pore surface impacts the emission ratio of the dye molecules.

.

Table of Contents

List of Figures

List of Tables

Acknowledgements

I want to acknowledge my major advisor, Dr. Keith L. Hohn for his continuous support and contribution to my study and research. His knowledge, patience, motivation, encouragement and enthusiasm have helped me all the time throughout my Ph.D. program, which is probably the most challenging experience in my life.

I want to thank Dr. Daniel A. Higgins for being my co-advisor, who has provided me with enormous amount of information and lab resources towards the completion of the doctoral degree. I could not have accomplished the thesis without his support.

I would like to express my gratitude to my committee members: Dr. Jennifer L. Anthony, Dr. Christine Aikens, and Dr. Placidus B. Amama for their valuable advice and kindness during all the important phases of the Ph.D program. I also would like to express my gratitude to my outside chair, Dr. Vinod Kumarappan, who was willing to participate in the final evaluation of my work.

I am grateful to the members in Dr. Hohn's and Dr. Higgins's research group: Myles Ikenberry, Xiaojiao Sun, Quanxing Zheng, Fan Zhang, Hao Xu and Seok Chan Park. I appreciate the many scientific discussions with them.

I am in debt to the staff in the Department of Chemical Engineering: Florence Sperman, Karey DeBardeleben, Pat Nelson, Danita Deters, Karen Strathman, and David Threewit for their assistance and cooperation in events and activities related to my research.

I want to thank my wife, Huan Wang, my parents and my grandparents for their full love, encouragement and support.

I want to thank all the professors and students who were involved in my 5 years of study and training in Kansas State University.

Dedication

To my parents

Xinran Xie

Fengying Cao

To my grandparents

Guangyu Xie

Jianqiu Li

To my wife, life partner and best friend

Huan Wang

Chapter 1 - **Introduction**

1.1 Hydrogen production via autothermal reforming and partial oxidation of hydrocarbons

Hydrogen, which serves as a reactant in ammonia production and as a clean fuel of fuel cells, has attracted great interest recently.[1, 2] Although many renewable energy based methods of hydrogen production such as photocatalytic water-splitting[3] were developed during past decades, currently most hydrogen is produced from fossil fuels.[14]

The proton–exchange membrane (PEM) fuel cell, which was developed in recent decades, exhibits great advantages for mobile power applications or small stationary power units. As an alternative for the internal combustion engine, PEM showed slightly higher energy efficiency and produced less pollution even though hydrogen fuel is produced from hydrocarbons.[2] Moreover, fuel cell systems show advantages such as light weight, compactness, and low signature emission (acoustic, thermal, etc.). Therefore, a fuel cell system is considered an ideal power supply for military applications.[158, 159] However, hydrogen gas, the ideal fuel for PEM, is hard to store and transport. In contrast, liquid hydrocarbon fuels such as gasoline and diesel are easy to store and transport. Thus, developing highly efficient and compact processes for on-board production of hydrogen from liquid fuels plays a key role for the fuel cell application of hydrogen in the field.[2, 158, 159]

Steam reforming (SR), partial oxidation (POX) and autothermal reforming (ATR) are considered to be the three major processes of converting fossil fuels into hydrogen. SR is widely applied for hydrogen production in industry.[4, 5] However, SR is endothermic so that an external heat source is necessary for the reaction.[1, 4, 6] On the other hand, POX is exothermic so an

external heat source is unnecessary.[7, 8] As a result, the reaction setups for POX are more compact than that of SR. ATR can be considered as a combination reaction of POX, SR and the water-shift reaction.[9] The heat generated from POX is utilized for the reforming of fuels.[1] ATR reactors are compact and suitable for mobile applications while producing higher hydrogen yields than POX. Thus, the ATR reaction is quite attractive for on-board hydrogen production.

Various kinds of fossil fuel[10, 11] and biomass products,[12] including methane, propane, liquid hydrocarbons, methanol, and ethanol, were investigated as the reactants for hydrogen production. Because of the current fuel supply structure and the convenience for storage and transport, liquid fuels like gasoline, diesel and JP-8 fuels are more attractive choices for on-board hydrogen production.[1] For this reason, processes for converting heavy hydrocarbons, ranging from C8 to C16, to hydrogen have been researched with great effort in recent years.

1.1.1 Reaction mechanisms of SR，POX and ATR reactions

The basic reaction process of SR is showed in equation 1.1.[1] Two main reactions are involved in the SR process, which are the reaction of the fuel with steam (equation 1.1) and the water gas shift reaction (equation 1.2). Note that the reforming reaction is endothermic. Hence, an external heat source is necessary for the SR reaction. Currently steam reforming is widely applied in industry and is the most economic method for the production of hydrogen gas.

$$C_nH_m + nH_2O \rightarrow nCO + \left(n + \frac{m}{2}\right) H_2 \tag{1.1}$$

For n=1: $\Delta H^o_{298K} = +206.2\ kJ/mol$

$$CO + H_2O \rightarrow CO_2 + H_2 \quad \Delta H^o_{298K} = -41.2\ kJ/mol \tag{1.2}$$

The reaction stoichiometry of POX is described in equation 1.3:

$$C_nH_m + \frac{n}{2}O_2 \rightarrow nCO + \frac{m}{2}\ H_2 \quad (1.3)$$

For n=1: $\Delta H^o_{298K} = -35.6\ kJ/mol$

POX produces two moles of hydrogen from one mole of methane, a lower ratio than steam reforming, since steam reforming produces additional hydrogen from the steam added to the process.

Up to now, two mechanism of POX have been proposed. The "direct" mechanism hypothesizes that fuels decompose on the catalyst surface followed by the coupling of hydrogen atoms and the oxidation of carbon atoms. The "indirect" mechanism proposes that the fuels are first totally combusted into water and carbon dioxide. Then hydrogen is produced through steam reforming reactions.[13] POX is strongly exothermic and reaction can occur in only milliseconds at high temperatures. As a result, the whole reaction is mass transfer limited.[14]

The ATR process basically involves partial oxidation, steam reforming and water gas shift reactions. [1, 2]As mentioned above, POX is highly exothermic and fast, but produces less hydrogen than SR, while SR is endothermic and slow. By combining partial oxidation and steam reforming, the heat necessary for steam reforming can be provided by the partial oxidation reaction so that the whole reaction system is autothermal. Consequently, the hydrogen production efficiency of ATR is much higher than that of POX while no external heat source is necessary as SR reaction setup. Thus, ATR is more suitable for the design of a compact portable hydrogen generator.

1.1.2 The hot spot formation problem of ATR

During the ATR process, the POX process will be faster than SR.[15] Consequently, only POX occurs at the inlet of the catalyst bed until oxygen is totally consumed. Since POX is highly

exothermic, this results in the formation of hot spots at the front of the bed.[16] When oxygen is completely consumed, hydrogen is produced by the endothermic reforming process downstream at relatively low temperatures. When Ni is applied as a catalyst for ATR, Ni may be oxidized by oxygen to NiO in the oxygen enriched region. NiO is still active for POX, however, the reforming activity of NiO for SR is lost. Thus, the hot spot formation problem is more severe when Ni is applied as the catalyst.[17] When a hot spot is formed, the heat generated via POX cannot be utilized for SR simultaneously and the thermal efficiency of ATR will decrease.

1.1.3 Catalysts for ATR

The catalysts for ATR are similar to those for the SR and POX processes. Group 8-10 metals such as Ni, Pt, Pd, Rh, are the most commonly used catalysts for the ATR process. As shown in Figure 1.1, S. Ayabe et al. investigated the ATR reaction of methane with a 2% (wt) of metal catalyst on an alumina support. The activity sequence of catalysts is Rh > Pd > Ni > Pt > Co. When the load of Ni catalyst increases to 10% (wt), the activity of Ni catalyst is higher than that of 2% (wt) Rh catalyst. Because of the high price and rarity of noble metal, Ni is widely utilized as the catalyst of ATR process even though it is less active.[18]

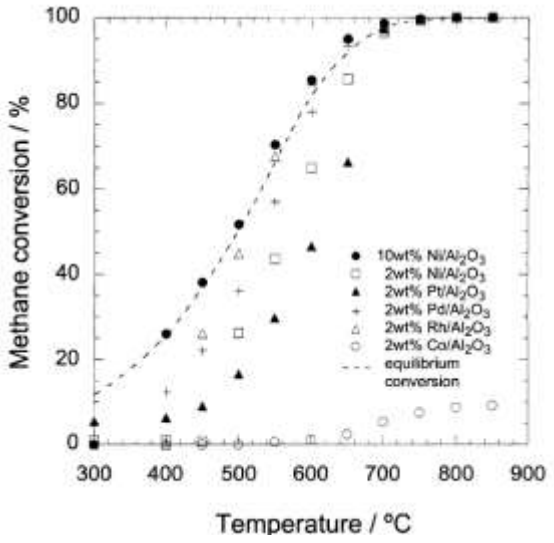

Figure 1.1 Temperature dependence of conversion for autothermal reforming of methane over various metal catalysts. Reaction conditions: CH_4, 16.7%; O_2, 1.7%; H_2O, 41.6%; N_2 (balance); S/C = 2.5; SV = 7200 h^{-1}; (- - -) equilibrium conversion.

1.1.4 Coke formation

During the reaction process, catalysts may deactivate by coke (carbon) formation. Claridge et al. demonstrated that the coke formation rate during the POX reaction follows the order of Ni > Pd >> Rh, Ru, Pt, Ir.[19] The reason for less carbon deposition on Rh, Ru, Pt, and Ir is attributed to the low carbon solubility of carbon in the bulk noble metals. In the case of Ni, however, three main carbon morphologies (carbon filaments, encapsulating carbon and pyrolytic carbon) may form at the nickel particle surface.[20] Figure 1.2 is an SEM image of carbon filaments deposited on Ni catalysts. The carbon filaments will not deactivate the nickel catalyst directly. Instead, the formation and growth of carbon filaments may lead to the mechanical breakdown of the catalyst pellet.[20]

Several methods were developed to reduce the coke formation on the surface of Ni catalyst, including control of the Ni particle size,[20] absorption of potassium or sulfur onto the catalyst surface, doping the catalysts with Au[21] and Ag,[22] and adding a promoter to the support.[23]

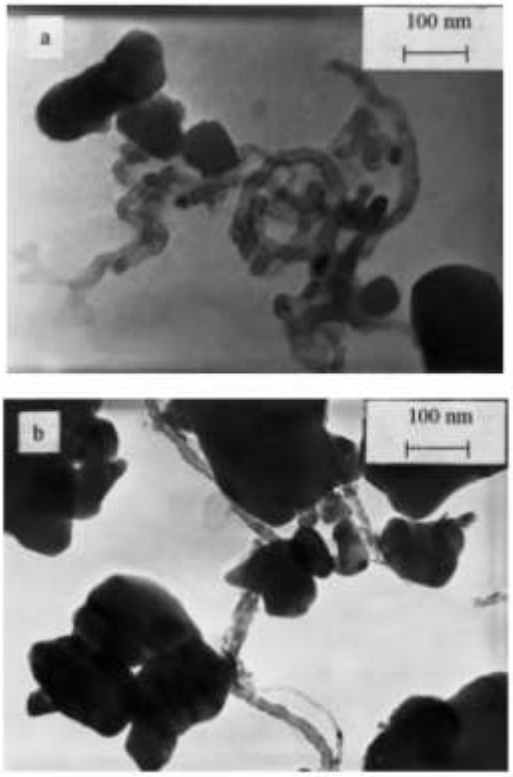

Figure 1.2 TEM micrographs of coke deposited on catalysts after the POX reaction.

1.1.5 Sulfur poisoning

The inherent sulfur content of liquid fuels greatly inhibits the catalyst performance in the ATR process. It is reported that the chemical absorption of sulfates/sulfites on active sites will induce the loss of activity for both Ni and noble metal catalysts.[18, 24-26] The catalyst tolerance for sulfates is higher than that for sulfites. As shown in Figure 1.3, the poisoning of a catalyst by sulfur is partly reversible.[27] When the sulfur-free feed was applied on the poisoned catalyst during the ATR process, the hydrogen yield gradually increased. However, the complete restoration of the original catalyst activity was not achieved.

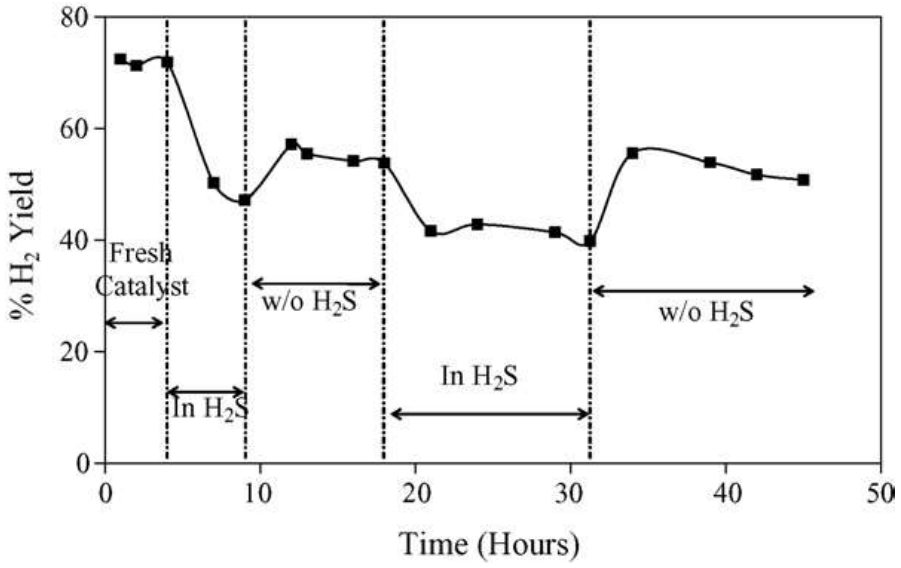

Figure 1.3 H_2 yield as a function of time in the presence of 150 ppm of H_2S during autothermal reforming of synthetic diesel fuel over the 1% Pt/ceria catalyst at $H_2O/O_2/C$ ratio of 2.5/0.5/1, reactor temperature = 400 °C.

1.1.6 Bimetallic catalysts

As mentioned above, the catalytic activity of Ni in the ATR process is not as high as noble metals. However, the low price of Ni, and the use of large Ni loadings enables the large-scale application of it as a catalyst for autothermal reforming.[28]

On the other hand, with the addition of noble metals, the catalytic activity of Ni is greatly enhanced. For example, Ni shows high activity in steam reforming reaction while Pt is active for the partial oxidation of hydrocarbons. The Ni-Pt bimetallic catalysts exhibit higher activity than the blends of separated Ni and Pt catalyst.[29] One possible explanation for this phenomenon is that the bimetallic system enhanced the heat transfer between the two reaction sites.[29, 30]

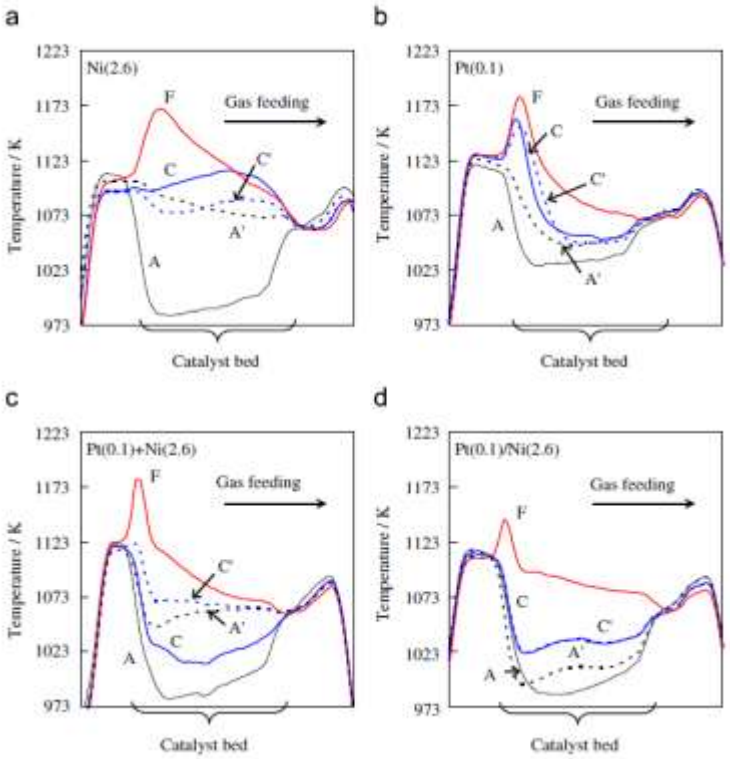

Figure 1.4 Effect of methane oxygen mixture (CH_4/O_2 =2/4) addition to methane steam reforming gas (CH_4/H_2O=30/30) (A → C → F) and the removal of the methane oxygen mixture from oxidative steam reforming of methane ($CH_4/H_2O/O_2$ =40/30/20) (F → C' → A') on the catalyst bed temperature profile. Partial pressure conditions: $CH_4/H_2O/O_2$/Ar = 30/30/0/40 (A,A'); 34/30/8/28 (C,C'); 40/30/20/10 (F).The x-axis is catalyst bed length while the y-axis is temperature(K).

In addition to the increase in Ni activity by adding a second metal, the reducibility of Ni catalyst can be maintained through the formation of a Ni-noble metal alloy in the presence of oxygen.[17] This, in turn, allows the reforming activity of the catalyst to be maintained. Preventing the formation of a hot spot may enhance the efficiency of heat transfer (Figure 1.4). Hence, the hydrogen yield and fuel conversion will be increased too.[31] As shown in Figure 1.4, When Ni is applied as catalysts for ATR (Figure 1.4 a curve F), an obvious hot spot can be observed. However, with the Pt/Ni alloy as the catalyst, the hot spots are suppressed significantly (Figure 1.4 d curve F). The suppression of the hot spot is not obvious if Pt and Ni catalysts are loaded at separate sites (Figure 1.4 c).

Even with the addition of a trace amount (<0.3% by weight) of noble metals (platinum, iridium or palladium), both the conversion and hydrogen yield of the ATR process of methane can be improved. According to Dias, the small amounts of noble metal added to nickel does not substantially affect the electronic properties of Ni, but does enhance the surface area of the catalyst.[32] This enhanced surface area is thought to allow NiO to be reduced to Ni by the noble metal additive during ATR.

Besides the Pt-Ni bimetallic catalyst, other alloy catalyst particles of different transition metals have been investigated. Strohm et al. investigated the low temperature autothermal reforming of jet fuel over Rh-Ni bimetallic catalysts. It is reported that the Ni addition into Rh catalyst greatly improved the sulfur resistance of catalysts.[33](Figure 1.5)

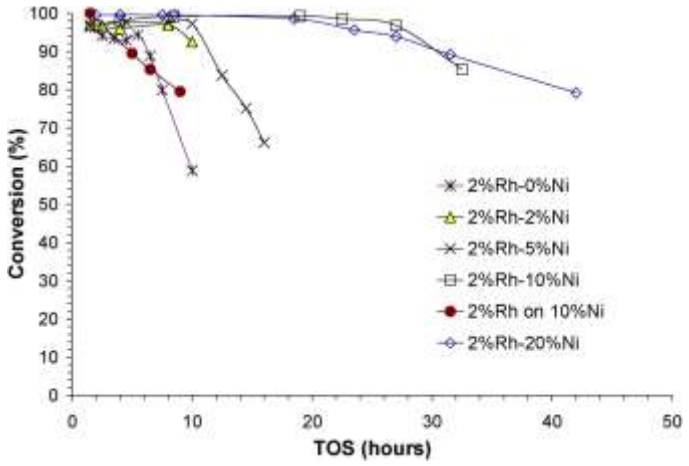

Figure 1.5 Catalytic conversion profiles for steam reforming of 100 ppmS NORPAR-13 and the effect of Ni loading level on the sulfur tolerance of 2% Rh–X% Ni/CeO_2–Al_2O_3 catalyst. X = 0, 2, 5, 10 and 20 wt%. For additional comparison, a catalyst with 2% Rh loaded on calcined 10% Ni/CeO_2–Al_2O_3 is also presented (2% Rh on 10% Ni).

Kaila et al. reported that addition of a small amount of Rh (0.1 wt%) enhanced the activity of the Pt catalyst markedly. In addition, bimetallic Rh-Pt catalysts showed better selectivity and stability than that of monometallic Rh or Pt catalysts.[34]

1.1.7 Catalyst supports for ATR

Alumina (Al_2O_3) and alkaline-earth based support

Gamma alumina is widely utilized as a catalysts support for ATR due to its high surface area and strong interactions with different metals. However, several drawbacks hinder its performance as an ATR catalyst support. First, the acidic sites on the surface of alumina catalyze the formation of ethylene, and the polymerization of ethylene leads to coke formation. Also, the porous structure of alumina cannot withstand the high temperatures at which ATR process is carried out.[35] In order to improve the thermal stability of alumina during high temperature reaction, additives based on alkaline-earth element such as magnesium and calcium or rare-earth element including cerium and lanthanum are introduced to modify the pore structure. The alkaline-earth metal oxides such as MgO and CaO can also be directly used as the ATR catalyst support. It is reported that Ni/MgO catalyst shows high resistance to coke formation due to the formation of an ideal solid solution between NiO and MgO.[36]

Ceria

Ceria exhibits high oxygen storage capacity and ionic conductivity and facile reducibility because of the favorable Ce III to Ce IV equilibrium. The role of ceria as an oxygen reservoir was fully demonstrated by the work of Wang's group.[37]As showed in Figure 1.6, Fe doped ceria particles were exposed to methane and steam at high temperature alternatively. In the first half cycle of reaction, methane was reformed by the oxygen stored in the catalyst to produce hydrogen and carbon monoxide without the presence of steam. In the second step of the cycle, ceria absorbs oxygen from steam to produce hydrogen.

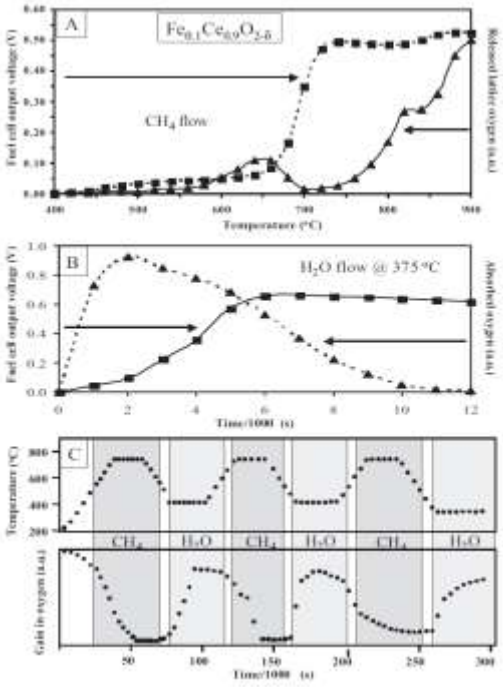

Figure 1.6 The two step reaction for the production of hydrogen from methane and water.

The morphology of nanocrystalline CeO_2 plays a crucial role in the performance of ceria-supported catalyst during the ATR process.[38] For instance, nanorods and nanocubes of ceria exhibit a greater capacity to store oxygen than spherical nanoparticles. The crystal plane of CeO_2 also impacts the reforming ability of catalysts. The {100}/{110}-dominant surface structures will lead to the enhancement of reforming reactions.[39] Recently, the high activity of catalysts loaded on doped CeO_2 nanocrystals[40] and extremely small ceria particles prepared by a template method [41] were also reported.

Perovskite oxides

Perovskite oxides, which show great promise in solid oxide fuel cell (SOFC) applications, are studied as catalysts for the ATR reaction[42-46] in recent years. The general formula of perovskite oxides are ABO_3, where A is a rare earth metal and B is a first-row transition metal (Cr, Mn, Fe, Ni, or Co). The excellent catalyst performance of perovskite oxides

comes from their outstanding thermal stability in a broad range of temperature as well as high oxygen storage capacity and oxygen ion conductivity.

1.1.8 Fuels

Fuels for ATR process are roughly divided into two groups: one is oxygen containing fuels, such as ethanol, methanol, and ether; the other is hydrocarbons such as natural gas, propane gas, gasoline, and diesel fuel.

Oxygen-containing fuels

Recently, a large amount of work regarding ATR of oxygen-containing fuels has been reported. Methanol and ethanol can be obtained from biomass feedstocks or from syngas derived from coal. The ATR reaction conditions for methanol and ethanol are mild compare to that of hydrocarbons.[47] In addition, methanol and ethanol are sulfur free, so no sulfur poisoning will occur during the reforming process. The conversion of ethanol by the ATR reaction can reach as high as 95% with 100% hydrogen selectivity.[48] In the case of methanol, carbon monoxides formed during the reforming process can be removed by preferential oxidation reaction[49] due to the low reforming temperature.

Hydrocarbons

Reforming of light hydrocarbons has been widely investigated for decades. However, the higher energy density and established distribution system for liquid hydrocarbons (such as gasoline and diesel fuel) make them more ideal fuels for in situ generation of hydrogen via ATR. When heavy hydrocarbons are utilized as fuels for ATR process, problems including the difficulty of vaporizing the fuels, severe coke formation and sulfur poison of catalysts.[9, 35, 50, 51]

Thus, precious metal or bimetallic catalysts loaded on ceria based supports or perovskite oxides are often applied for ATR of heavy hydrocarbons.

L. D Schmidt's group systematically investigated the POX and ATR process of higher hydrocarbons over Rh coated monolith. For the POX process, it is interesting to note that the CO and hydrogen selectivities decrease while the total olefins selectivity increase with the growth of molecular weight of hydrocarbon feeds.[15](Figure 1.7)

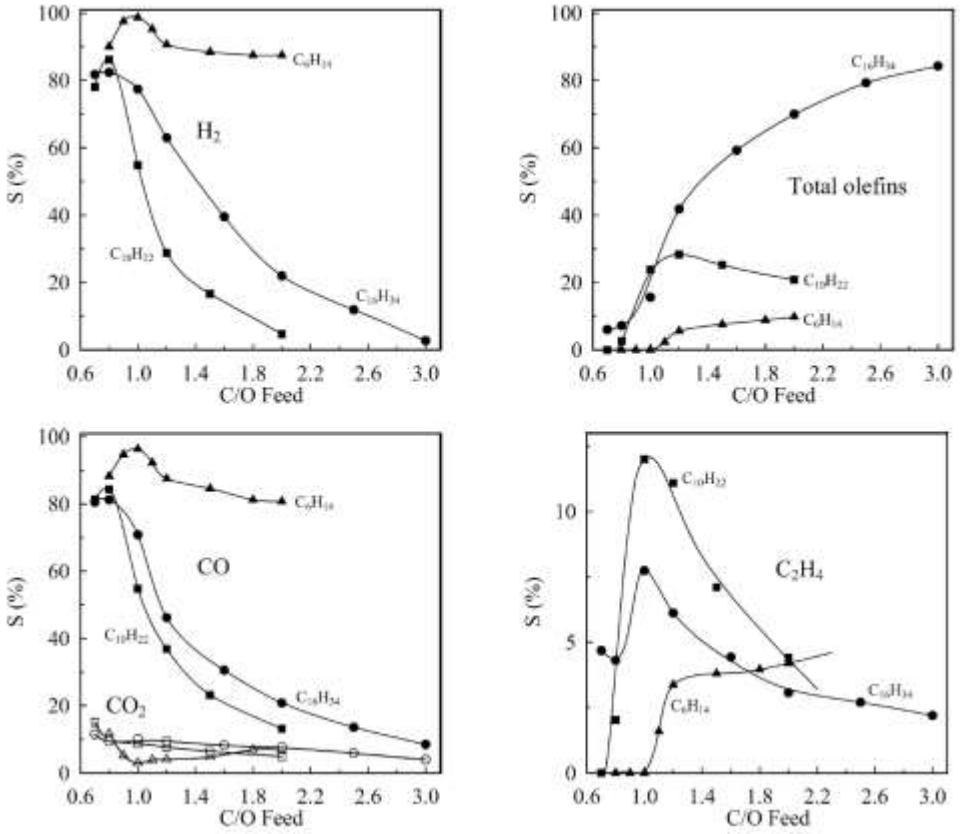

Figure 1.7 Comparison of the product distribution from n-hexane (2.5 standard liter per minute (SLPM)), n-dodecane (4 SLPM), and n-hexadecane (4 SLPM) during POX.

For ATR of heavy hydrocarbons, Dreyer et al. reported that adding steam greatly suppressed the production of olefins and enhanced the selectivity of synthesis gas.[52] Although a Rh catalyst was used in Dreyer's work, the hot spot formation phenomenon is obvious. Oxygen is consumed by partial oxidation and combustion of n-hexadecane in the initial 1mm layer of

monolith, while steam reforming dominated the remaining 9mm length of the monolith at lower temperatures.

Although Ni shows lower activity and less resistance to coke formation during ATR of higher hydrocarbons, with specific promoters, high activity can still be achieved and coke formation can be reduced. Nickel-Ceria-Zirconia based catalysts displayed high relative activity for ATR of dodecane and no severe deactivation was observed.[53] Ni/M/MgO/Al_2O_3(M=Fe, Co,Mo) also showed resistance to coke formation and relatively high activity during ATR of Iso-octane.[54] In the case of Ni/Al_2O_3-La_2O_3-CeO_2 catalysts, due to the greater activity of the metal-ceria interface, a much higher activity and resistance to coke deposition can be achieved compared to Pt/ Al_2O_3-La_2O_3-CeO_2.[50]

Pt/CeO_2 was also investigated for hydrogen production from higher hydrocarbons. Cheekatamarla et al. explored the ATR of diesel fuel and JP8 with Pt/CeO_2 as the catalyst.[24, 27] They found that hydrogen can be produced at a lower temperature (400^{o}C) compared to other studies (>700^{o}C). The Pt/CeO_2 catalysts showed high stability for synthetic diesel with less than 10 ppm sulfur, but the impact of higher levels of sulfur was not evaluated.

Pt showed strong interactions with a gadolinium-doped Ceria support. Pt-Gd_2O_3-CeO_2 catalysts displayed high efficiency for ATR of higher hydrocarbons.[55] In addition, Pt-Gd_2O_3-CeO_2 showed high resistance to sulfur poison.[56]

For both alumina and ceria supports, the application of bimetallic catalysts for the ATR of higher hydrocarbon exhibits higher activity and better sulfur resistance than their single metal counterparts.[57] As reported by Cheekatamarla et al.,[57] Pd-Pt catalysts (the impregnation order is Pd first, Pt second) showed higher activity when alumina is applied as the support while Pt-Pd achieved the highest hydrogen yield with ceria as the support. The XPS, temperature

programmed reduction (TPR) and temperature programmed desorption (TPD) showed that the formation of a Pt-Pd alloy led to electron deficiency in the Pt and the reduction of chemisorption of sulfur. Consequently, the performance of catalysts for diesel ATR was enhanced.

Erri et al. applied Ni and Ce doped lanthanum iron perovskites oxides for ATR of JP-8.[45] The catalysts showed higher stability with larger than 90% conversion. The hydrogen yield was near equilibrium. Doping Ni into perovskites oxides led to significant coke formation while doping Ce resulted in coking resistance. It was also reported that a small concentration of metal additives such as 2wt.% of potassium or 1wt.% of ruthenium enhanced the sulfur resistance of perovskites oxides.[46]

1.1.9 Summary

ATR shows great promise for the in-situ production of hydrogen for fuel cells, due to its high hydrogen production efficiency and modest energy requirements. In order to utilize liquid hydrocarbons, which are convenient to obtain and store as the fuel for the ATR process, several challenges must be overcome, including severe coke formation, sulfur poisoning and high yields of byproducts such as olefins.

Although it is reported that the disadvantages of ATR of heavy hydrocarbons can be reduced by the carefully selection and design of catalysts and supports, more work is necessary for optimization of the ATR catalyst.

1.2 Investigation of mesoporous solid acid catalysts thin film via single molecule spectroscopy

1.2.1 Heterogeneity of catalysts

Heterogeneous catalysis, which is involved in the production of more than 80% of all chemicals precursors and intermediates, is of great importance in the modern chemical industry.[58] Heterogeneous catalysts are complex, considering the distribution of active sites and porous structures of the catalysts.[59]

The ensemble average properties of heterogeneous catalysts have been well studied[58]. For example, the acidity of solid acid catalysts could be investigated via numerous methods, including TPD,[60] Fourier transform infrared spectroscopy (FTIR),[61] nuclear magnetic resonance (NMR) spectroscopy[60, 62] and even titration.[63] However, recent research demonstrated that the reaction sites are not distributed uniformly throughout the whole catalysts.[64] Thus, the investigation of local environments becomes essential. Figure 1.8 is a 2D photoemission electron microscopy (PEEM) image of catalytic CO oxidation with O_2 on a Pt (110) surface. Dark areas are O_2 covered regions while the bright areas are covered by CO. Spiral waves formed and propagated at the surface of Pt.[64]

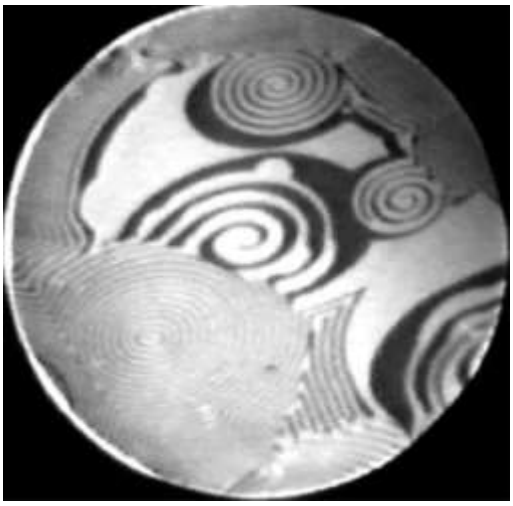

Figure 1.8 2D Photoemission electron microscopy (PEEM) image from a Pt(110) surface during catalytic CO oxidation (P_{CO}=4.3*10^{-4}, P_{O2} =4*10^{-5} mbar, T=175^{o}C). The diameter of the picture is 500 mm.

The heterogeneities of individual catalysts in space and time have been monitored by different spectroscopies, [65] such as scanning tunneling microscopy[66, 67] and tip enhanced Raman spectroscopy.[68] With fluorescent probes, single molecule spectroscopy (SMS) can be applied to visualize catalytic surfaces at the molecular level.[69] Via SMS, the polymerization of dicyclopentadiene by Grubbs catalysts, which has been reported to be a heterogeneous reaction, was proved to be a homogeneous reaction.[70] Roeffaers et al. investigated the trans-esterification and hydrolysis of 5-carboxyfluorescein diacetate (C-FDA) on a layered double hydroxide (LDH) surface.[71] The transesterification reaction of C-FDA occurred all over the catalysts while hydrolysis reaction only happened on {1010} facets at the edge of the catalysts where OH^- ion existed.

The crystal face dependence of catalysis was also monitored via SMS in several other systems.[72, 73] Resorufin, which is highly fluorescent, could be produced via reduction of the nonfluorescent reactant resazurin or the oxidation of the nonfluorescent reactant, amplex red.[74, 75]

Thus, precious metal-catalyzed reduction and oxidation reactions were also visualized via SMS. Chen and co-workers conducted a single turnover study of fluorogenic reaction catalyzed via precious metal nanoparticles.[73, 76] Typically, a fluorescent burst was observed when resorufin was generated on the surface of a metal nanostructure while the sudden extinction of the fluorescence signal was ascribed to the dissociation of resorufin from the nanoparticles and diffusion to the bulk phase. Therefore, τ_{off} is the waiting time before each resorufin formation while τ_{on} is the waiting time for resorufin detachment from nanocatalysts[73] (Figure 1.9). Via this method, the catalytic kinetics of a fluorogenic reaction on metal nanocatalysts including various structures of Au,[75] Pt[77] and Pd[78] could be explored and the activity difference along different nanostructures was mapped as well.[72, 79]

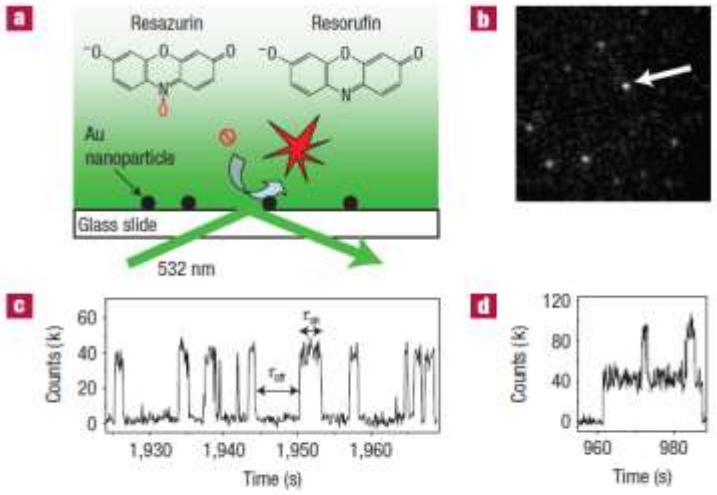

Figure 1.9 Single-turnover detection of single-Au-nanoparticle catalysis: (a) Experimental design using total internal reflection fluorescence microscopy: (b) A typical image (~18×18 μm2) of fluorescent products during catalysis taken at 100 ms per frame. The pixel size is ~270 nm, which results in the pixelated fluorescence spots; (c) A segment of the fluorescence trajectory from the fluorescence spot marked by the arrow in b at 0:05 μM resazurin and 1mM NH_2OH; (d), A segment of another fluorescence trajectory showing two on-levels at the same conditions.

In addition to the metal nanoparticles-catalyzed reduction and oxidation reactions, electrocatalysis was also studied via SMS with the assistance of the reduction reaction of nonfluorescent resazurin to resorufin[80] (Figure 1.10). Xu et al. reported the single molecule fluorescence study of electrocatalysis by single-walled carbon nanotubes (SWNTs). The electrocatalyzed reaction happened at discrete sites along the SWNTs instead of uniformly along the whole sidewall of the nanotubes. The single turnover investigation was also carried out on SWNT electrocatalysis systems.[81]

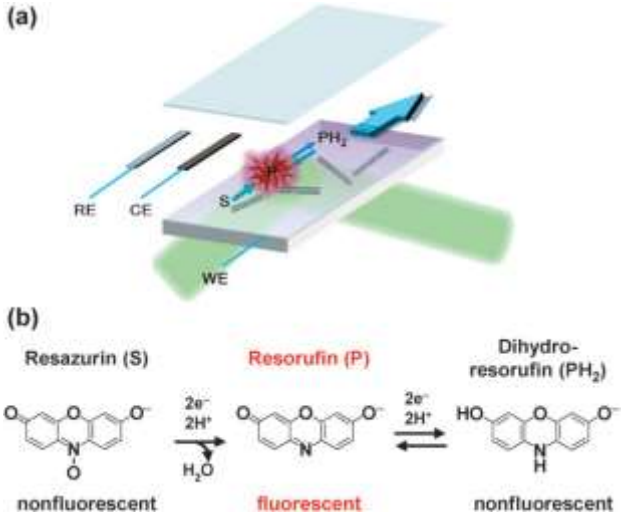

Figure 1.10 Single molecule fluorescence approach to carbon nanotube electrocatalysis. (a) Experimental design using an electrochemical flow cell made between an ITO-coated quartz slide and a coverslip, and total internal reflection fluorescence microscopy. WE, RE, CE: working, reference, and counter electrodes. (b) Redox chemistry of resazurin in aqueous solution.

The impact of molecular transport on the catalysis reaction in porous structures was also studied. Kazuya et al. investigated the photocatalytic reaction in TiO_2 nanotubes via single molecule observation. [82] The transport of reagent into macroporous and mesoporous TiO_2 pores were studied and compared and the whole reaction was found to be diffusion limited.

1.2.2 Mesoporous and microporous solid acid structure, application and single molecule microscopy investigation

Mesoporous and microporous solid acid catalysts are widely applied in various reactions including dehydration,[83] hydrolysis[84] and cracking.[85]

Lai et al. synthesized Fe_3O_4 nanoparticles embedded in a SBA-15 catalyst, which is the first magnetic solid acid with an ordered mesoporous structure. With further modification to attach sulfonic acid groups onto the surface of the mesoporous structure, the Fe_3O_4–SBA–SO_3H catalysts exhibited excellent activity for the hydrolysis of cellulose into glucose.[86]

The production of 5- hydroxymethylfurfural (HMF) from glucose plays a pivotal role in the further production of biofuels from cellulose or hemicellulose, which are two main components of biomass. With acid functionalized SBA-15 as catalysts, HMF can be produced both in the aqueous phase[87] and in ionic liquids.[88] Besides HMF production, dehydration of butanol has also been reported with functionalized silicate mesoporous structure such as MCM-41 and SBA 15.[89] It was also reported that butanone could be effectively synthesized from fermented 2,3 butanediol over boric acid modified HZSM-5 zeolites. Acid-base bifunctional catalysts can also be prepared via incorporation of both sulfonic acid and amine into SBA 15 during a one-pot synthesis. The bifunctional catalysts prepared in this way show high activity for the aldol condensation reaction of acetone with 4-nitrobenzaldehyde.[90]

The catalytic activity of mesoporous and microporous solid acid catalysts is significantly influenced by their acidity. Moreover, the acidity of modified mesoporous silica structures is not only influenced by the concentration and intrinsic strength of acid sites, but also the spatial distribution of these acid sites.[91] As reported by Isa et al., the acid strength of sulfonic acid

functionalized SBA-15 can be enhanced through incorporation of spatially organized sulfonic acid groups.[91]

Due to their large surface area, mesoporous and microporous silica or silica-alumina structures are also applied as supports for catalysts.[92] For instance, cobalt loaded SBA 15 showed excellent activity for the Fischer-Tropsch reaction because of the high metal dispersity.[92, 93]

Meso or micro porous structures such as zeolites are often reported to afford shape-selectivity due to the pore confinement effect.[94] Shape selective catalysts was been widely applied in oil refining,[95] biomass pyrolysis[96] and organic transformations.[97] Michiel et al. reported the highly selective synthesis of lactide from lactic acid with H-Beta zeolite as a catalyst.[98] In contrast, sulfuric acid or large porous zeolite catalysts such as H-Al-MCM-41 showed much less selectivity for lactide. Agirrezabal-Telleria et al. investigated functionalized SBA-15 as catalysts for converting xylose to furfural.[99] It was found that catalysts with a large pore size showed higher conversion but less selectivity, while catalysts with smaller pore size showed lower activity but higher selectivity for furfural production. Although most studies on shape selectivity focused on gas phase reactions with microporous zeolites as catalysts, Chen et al. reported a shape selective Suzuki coupling reaction catalyzed via a Pd loaded mesoporous catalyst.[100] The diffusion barrier generated by the mesoporous silica wall played a key role in governing the shape selectivity of the reaction. Molecules with larger diameters showed less selectivity even if their diameter is still smaller than the silica pore size. Monoglyceride can be synthesized from glycerol and fatty acids through an esterification reaction. However, since glycerol contains three functional groups, byproducts such as diester or triester can be produced. SBA-15 and MCM-41 supported sulfonic acid catalysts or tungsten oxide[101] are often applied for

monoglyceride synthesis with high selectivity.[102, 103] MCM-41 showed higher selectivity for monoglyceride synthesis due to the narrower pore diameter.[103]

In addition to applications in catalysis, mesoporous silica monoliths with sub 10-nm diameters are considered to be promising candidates for nanofluidic devices.[104-106] For a silica nanofluidic device, the deprotonation of silanol groups leads to a layer of surface charge along the wall of the mesopores. Therefore, an electrical double layer (EDL) will form at the silica surface. Moreover, because the diameter of the pores is comparable to the Debye length of the EDL, the EDL may overlap in the pores of nanofluidics when the pore diameter is less than the Debye length, especially for mesoporous silica or alumina monoliths with small pore size.[106-108] The overlap of the EDL in the nanopores leads to many interesting phenomena. For instance, counterions are enriched in the nanopores, while co-ions are driven out of the pores.[108, 109] The contribution of surface conductivity is enhanced while the contribution of bulk phase conductivity decreases.[104] As shown in Figure 1.11, Rong Fan et al. investigated the ion conduction of HCl and KCl in aligned SBA15 mesoporous thin films. At high ion concentration, bulk-like behavior of ion conduction is observed, which indicates that the electrical double layer is sufficiently suppressed. With a decrease in ion concentration, the contribution of surface charge becomes important.[104] Based on these specific phenomena caused by the EDL and nanoconfinement effects, applications regarding nanofluidic devices could be developed. When a pressure-gradient is applied along the aligned nano-pores, a streaming current and potential are generated, which offers the possibility of new battery design.[110] On the other hand, electroosmotic flow can be generated when a potential is applied along the nanochannels.[109] In addition, the proton conductance in nanochannels can be varied via application of a gate voltage,[107, 111, 112] which is similar to the performance of semiconductor transistors.[113, 114]

Electroosmotic flow has been applied in many bio-M/NEMS (Micro/Nano-electro-Mechanical-systems) for purposes such as separation[115] and sensing.[116]

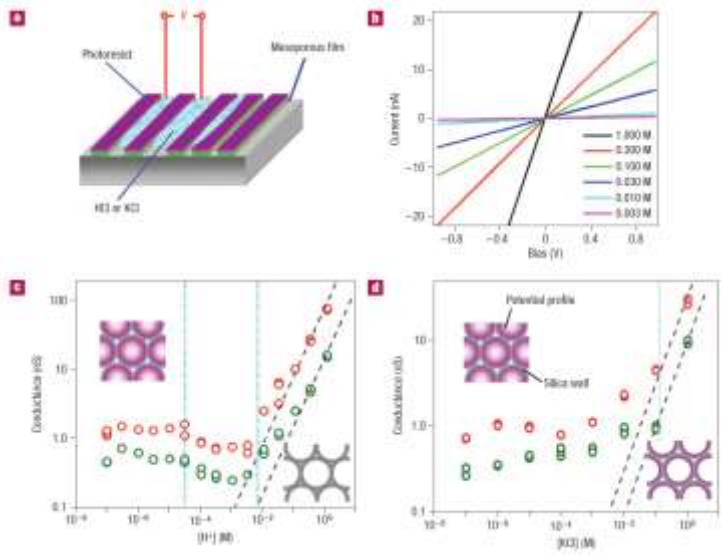

Figure 1.11 Concentration dependence of proton and ion transport: (a) Schematic diagram of the measurement of ionic current through coarse-patterned mesopore thin-film stripes; (b) Representative current/bias (I/V) curves recorded at different proton concentrations. (c) Proton concentration dependence of ionic conductance. It apparently deviates from bulk behavior (dashed lines) at lower concentration and changes to a surface-governed ion transport. Proton conduction exhibits three distinct regions—a surface-charge dominant zone (lowest [H^+]), a bulk concentration dominant zone (highest [H^+]) and an intermediate zone where surface charge density is significantly reduced by increasing proton concentration resulting in a minimum of ionic current. High [H^+] (beyond the isoelectric point, pH 2.6) results in a nearly zero surface potential owing to complete protonation. (d) KCl salt concentration dependence of ionic conductance. The insets schematically show the electrostatic potential (magenta) within nanochannels. It extends well into the nanochannels at low concentrations owing to the large screening length, but becomes shielded at [KCl] > 0.1 M. Red and green circles in c,d represent data taken from two independent devices.

Recently, many efforts to probe silica-based mesoporous structures via single molecule fluorescence spectroscopy have been reported. In particular, the diffusion properties of dye molecules in silica-based films have been well studied. Currently, two different methods have been applied for diffusion measurements of fluorescent molecules in the mesoporous structure. The first is fluorescence correlation spectroscopy (FCS). Basically, a small volume of sample is

illuminated and excited with a focused laser beam and the fluctuation of fluorescence intensity from dye molecules within this small volume is measured. The fluctuation of number of dye molecules and the fluorescence intensity will be less significant if a large number of dye molecules are applied for measurement. Thus, it is crucial to maintain a small exciting volume and low density of fluorescent dye molecules. The autocorrelation method is utilized for the analysis of fluorescence intensity fluctuations with time and the autocorrelation function used for FCS is calculated as follows:

$$G(\tau) = \frac{<\delta F(t)\delta F(t+\tau)>}{<F(t)^2>} \tag{1.4}$$

where δF(t) and δF(t+τ) are the fluorescence fluctuations at t and t+τ. Note that the fluctuation of dye molecule concentration at any spot within the measured volume at t will diffuse to other positions after certain time interval τ. The concentration fluctuations due to dye molecule diffusion can be depicted by Fick's second law.

$$\frac{d\delta c}{dt} = D\nabla^2\delta \tag{1.5}$$

The boundary condition for δc is equal to zero at infinity. Solving the diffusion equation via Fourier transform, a Gaussian like distribution of δc with respect to position is obtained.

$$\delta c(r,\tau) = \delta c_0 \frac{1}{4\pi D\tau^{\frac{3}{2}}} e^{-\frac{r^2}{4D\tau}} \tag{1.6}$$

The number density of the autocorrelation term $\langle \delta c(r,0)\delta c(r',\tau)\rangle$ can then be calculated as follows:

$$\langle \delta c(r,0)\delta(r^{'},\tau)\rangle = \langle c\rangle \frac{1}{(4\pi D\tau)^{\frac{3}{2}}} e^{-\frac{(r-r^{'})^2}{4D\tau}} \tag{1.7}$$

Note that $<\delta F(t)\delta F(t+\tau)>$ is then defined by two factors, $\langle \delta c(r,0)\delta c(r^{'},\tau)\rangle$ and the spatial distribution of the excitation laser profile, which is determined by the instrument. For the same reason, $<F(t)^2>$ is also a function of $\langle c\rangle$ and the spatial distribution of excitation light. Thus, G(τ) can be expressed as a function of D, which is the diffusion coefficient of the fluorescent molecule. In the case of single component diffusion, G(τ) is expressed as follows:

$$G(\tau) = \frac{1}{V_{eff}\langle c\rangle} \frac{1}{(1+\frac{\tau}{\tau_D})} \frac{1}{\sqrt{1+(\frac{r_0}{z_0})^2 \frac{\tau}{\tau_D}}} \tag{1.8}$$

where V_{eff} is the effective focal volume, τ_D is defined as the lateral diffusion time and $\boldsymbol{\tau_D = \frac{r_0^2}{4D}}$. Note that r_0 and z_0 is determined by calibration.

When it comes to the diffusion of dye molecules in mesoporous thin films, first, due to the small thickness of thin film, the requirement for the small focal volume will be satisfied; moreover, both surface adsorption and diffusion will happen and a modified model should be selected to fit the data. This model is given as follows:

$$G(\tau) = \frac{A_d}{(1+{D\tau}/{s^2})} + A_a\, e^{(-\tau k)} \tag{1.9}$$

where A_d is the amplitude of the correlation function decay due to diffusion and A_a is the amplitude due to adsorption, D is the diffusion coefficient for the probe dye, s^2 is the beam variance and k is the rate constant for desorption of adsorbed species. Yi Fu et al. investigated the diffusion of Nile Red molecules in calcined mesoporous silicate thin films. Mean diffusion coefficients of 2.4×10^{-10} and 2.6×10^{-10} cm^2/s were obtained and mean desorption times of

(1/K=25 and 40s) were also calculated.[117] Similar results are also observed in other work reported by S. M. Mahurin et al..[118] In addition to probing porous silicate structures, the FCS method is also applied for the analysis of other nano channel structures. Hao Xu et al. investigated the diffusion of negatively charged sulforhodamine B in organic nanotubes, in which the inner surface is terminated with amino groups.[119] The amino groups on the inner surface of the nano-channels carry a positive charge at relatively low pH. The motion of dye molecules is greatly affected by the charging of the nanochannels because both the pH and ionic strength of the solution filling the nanotubes had a significant impact on the diffusion coefficient of the dye molecules.

Another method for the study of single molecule diffusion in mesoporous silicate thin films is single molecule tracking (SMT). Although the resolution of an optical microscope is restricted by the diffraction of light, the precise location of individual dye molecules can be obtained by fitting the diffraction-limited emission pattern of the individual molecules. For most dye molecules, a Gaussian function is used to describe the diffraction pattern. For other cases, such as when terrylene diimide (TDI) dye molecules are perpendicularly embedded in laminar mesoporous silicate films, a donut shape diffraction pattern is observed.[120]

With the precise location of the dye molecules in the individual frames of a video, the diffusive behavior of the molecules can be investigated by measuring their mean-square displacement $\langle r^2 \rangle$ as a function of time. According to the Einstein-Smoluchowski relation, the relation between the mean-square displacement and time could be expressed as follows:

$$\langle r^2 \rangle = 2dD\mathrm{t} \tag{1.10}$$

where d=1, 2 or 3 corresponding to one-, two- or three-dimension diffusion, D is the diffusion coefficient and t is time.[121, 122] Note that the D determined via SMT is the diffusion

coefficient of single molecule self-diffusion. Due to the heterogeneity of mesoporous silicate structures, the diffusion coefficient obtained via SMT varies dramatically between different molecules.[120]

Christoph Bräuchle's group systematically explored the diffusion of single fluorescent dye molecules in mesoporous silicate films with different structures, including hexagonal and laminar structure with various pore sizes.[120, 123-126] TDI was applied as a fluorescent probe for the SMT study for all these mesoporous silicate films.[125] SMT data were correlated with structural data from TEM images of the same sample regions. For every micro domain with the same orientation of pore structure, TDI dye molecules were found to diffuse along the pore orientation. When the molecules crossed domain boundaries, the direction of diffusion changed accordingly. Thus, analysis of the movement of fluorescent single molecules can provide information on linear or strongly curved sections of the hexagonal channel system, domain boundaries, boundaries between ordered and disordered sections, and leaky channels that permit lateral travel.

When the mesoporous silicate thin film with mixed structure of hexagonal and laminar features are studied by SMT, due to the different diffraction pattern of TDI in these two phases, the trajectory and diffusion coefficient of dye molecules in different phases can be studied.[120] In addition, the diffusion of TDI through the boundary between hexagonal and laminar phases was observed.

The one-dimensional diffusion of TDI in well-aligned hexadecyltrimethylammonium bromide (CTAB) templated thin silicate films has also been studied.[123] The lateral diffusion between pores indicates defects of pore structure including dead ends or opening on the sidewalls

of the pores. The overall dynamics of the moving molecules was well described via the 1 D random walk model.

Besides the diffusion of fluorescent guest molecules in the pore structure of silicate thin films, other properties of mesoporous silicate structure have also been investigated via the single molecule method. With the assistance of polarized laser light for the excitation of dye molecules, Christian Seebacher et al. studied the orientation of pores in $AlPO_4$-5 crystals.[127] Oxazine dye molecules embedded in the pores of $AlPO_4$-5 crystals lead to their alignment along the pore orientation direction due to the confining effects of the pore structure. Moreover, the alignment of dye molecules results in an optically anisotropic system. Consequently, the fluorescence intensity varies as a function of the rotation of the polarized excitation light.

Nile red dye molecules, which are sensitive to the polarization of the environment around them, have also been applied to probe the polarity of the microenvironment in the mesopores of silicate thin films.[128]

1.2.3 Fluorescent dye molecules for pH measurement

In the last few decades, fluorescent dye molecules were developed as probes for pH measurements in biosystems.[129, 130] Many probes for pH are dual emission dyes which are excited by light with one fixed wavelength but emit fluorescence at two different wavelengths in a pH dependent manner.[131, 132] The ratio of intensity at these two different wavelengths can then be related to the pH value. The most widely used dual emission fluorescent probes for pH are based upon the C-snarf dye molecules.[129, 133] Figure 1.12 shows the structure of C-snarf-1((5' and 6')-carboxy-10-(dimethylamino)-3-hydroxy-spiro [7H-benzo-[c]xanthene-7,1'(3H)-isobenzofuran]-3'-one).[134, 135] With excitation at 532 nm, C-snarf-1 emits fluorescence with a peak at 580 nm for the pronated state and at 640 nm for the deprotonated state.[136] The

microenvironment pH of biofilms,[133] living cells[130, 132, 137-139] as well as protein crystals[140] could be analyzed with C-snarf as probes. For example, A.A.Venn mapped the intracellular pH in reef coral and symbiotic anemone via confocal microscopy with C-snarf-1 as the fluorescent probe.[137] Ryan C. Hunter et al. analyzed the local pH of biofilms via C-snarf-4.[133] The pKa of C-snarf-1 is 7.4, while the pKa of C-snarf-4 is 6.4. Thus, C-snarf-4 is more suitable as a pH indicator in acidic environments.[129, 133]

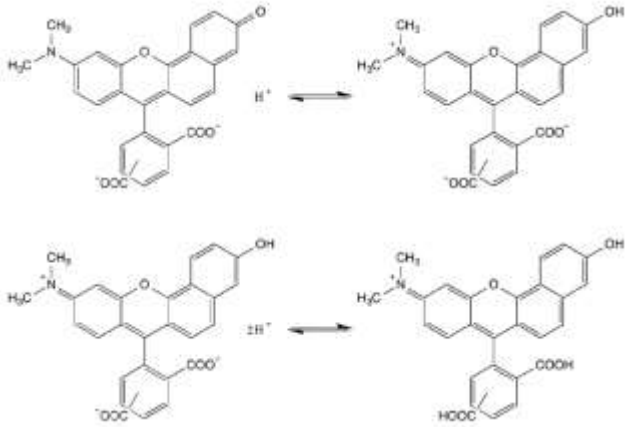

Figure 1.12 Chemical structures of C-snarf-1 in its protonated and deprotonated forms. (a) Structure of the first acid-base equilibrium (pKa ~ 7.6) and (b) Structure of the second acid-base equilibrium (pKa ~ 4.2).

The quantitative measurement of pH in individual microenvironments can be achieved via a modified Henderson-Hasselbalch equation.[136, 138, 141] The Henderson-Hasselbalch equation relates the pH of a solution to the concentrations of the relevant protonated and deprotonated species.

$$pH = pK_a + \log(\frac{[P]}{[D]}) \tag{1.11}$$

where Ka = $[D][H^+]/[P]$

D is the deprotonated state of the dye while P denotes its protonated state. Thus, [D]+[P] = C_T.

$$[D] = \frac{K_a}{K_a + [H]} C_T \tag{1.12}$$

$$[P] = \frac{[H]}{[H] + K_a} C_T \tag{1.13}$$

However, for most fluorescent probes, the emission at two different wavelengths cannot be separated completely. In the case of C-snarf-1, the 580 nm emission peak still showed a shoulder at 640 nm and vice versa. Consequently, [D]/[P] cannot be replaced directly by the ratio of intensity at two different wavelengths.

The intensity of fluorescent light from dye molecules at each wavelength can be expressed by:

$$I_D = g_D D + g_p \gamma_p P \tag{1.14}$$

$$I_P = g_P P + g_D \gamma_D D \tag{1.15}$$

where g_D and g_P are the product of quantum efficiency of the probe, the collection efficiency of the microscope, and the quantum efficiency of the detector, for the neutral and protonated states, respectively. γ_D is the fraction of intensity of the neutral emission collected in the protonated emission channel and γ_P is the fraction of intensity of the protonated emission collected in the neutral emission channel. By combining the equations above, the modified Henderson-Hasselbalch equation is derived.

$$pH = pK_a + \log\left(\frac{g_p}{g_D}\bar{R}_{max}\right) + \log\left(\frac{\bar{R} - \bar{R}_{min}}{\bar{R}_{max} - \bar{R}}\right) \tag{1.16}$$

$\bar{R}$ is the mean I_p/I_D ratio, $\bar{R}_{max}$ and $\bar{R}_{min}$ are the maximum and minimum limiting values of R, which could be used as an estimation of $\gamma_p$and γ_D.

The intracellular quenching of C-snarf-1 was also reported in a pH dependent manner.[142-144] It is reported that the spectrum in the deprotonated state was affected to a greater extent than in the protonated state.[143] Studies regarding the interaction of C-snarf dye molecules with protein, cell membranes and the impact of these interactions to fluorescence quenching and pK_a changing were conducted.[142-144] A nanoreactor that could be applied to encapsulate C-snarf dye molecules for probing of pH in cells without the influence from protein and other biomolecules was also reported. [145] To further investigate the intracellular pH value of cells under high hydrostatic pressures, the influence of pressure on the fluorescent pH probes was also explored.[146, 147]

In addition to C-snarf, other dual emission dye molecules were also explored as fluorescent pH probes. Junyan Han et al. developed a new ratiometic pH probe named Cassette 1 with lower pK_a(4.0-6.5) than that of C-snarf (Figure 1.13).[131]

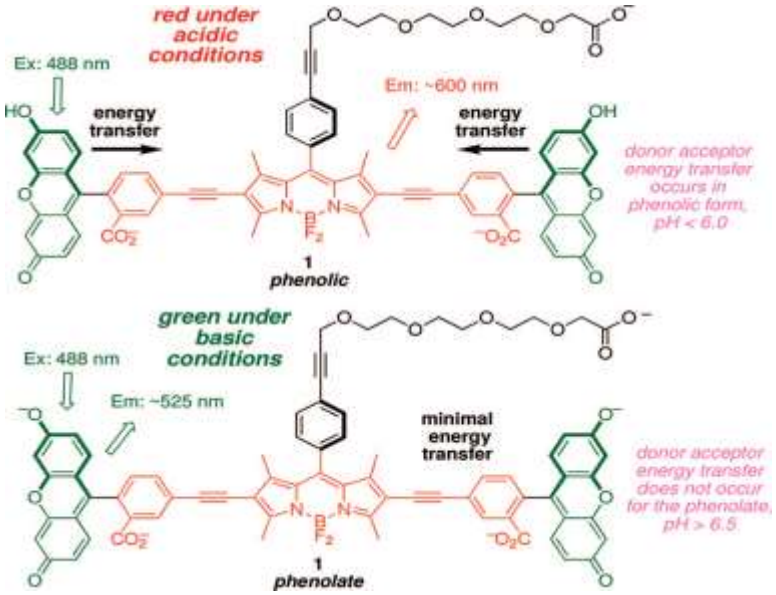

Figure 1.13 Chemical structures of Cassette 1

Unlike other dual emission pH sensitive dye molecules, Coumarin 6 showed different excitation and emission wavelengths for both protonated and deprotonated states. With simultaneous excitation of both protonated and deprotonated state of dyes via two distinct laser source, the intensity ratio R can also be achieved.[141, 148]

Besides radiometric dual emission dye molecules, another group of fluorescent pH probes only showed fluorescent emission at deprotonated or protonated state. Thus, the fluorescent intensity of pH probes will not only be determined by the pH value of environment but also other factors such as excitation light intensity and dye concentration. However, with the assistance of FCS method, the pH value of microenvironment could also be measured.[149, 150] Compared to probing the pH value of a microenvironment with a dual emission pH indicator as discussed above, the FCS method does not require the calibration curve of emission ratio versus pH value to access the local pH.[149] For example, the protonated state of enhanced green fluorescent protein (EGFP) emits fluorescent light upon 488 nm excitation. Protonation of the Tyrosine-66 hydroxyl group on the chromophore brings the EGFP molecule from a deprotonated state. Thus it could be

applied as a local pH probe with the assistance of the FCS method. The fluorescent emission of EGFP is also temperature dependent. Felix H. C. Wong et al. developed a method for the measurement of temperature in microenvironment with certain pH values base on EGFP and FCS method.[151]

Recently, pH sensitive fluorescent dye molecules were also widely applied for the local pH value measurement in the area of material science. The pH value and morphology of interstitial fluids in between ice polycrystalline containing rejected fluid could be indicated by adding low concentration C-snarf into freezing aqueous electrolyte solutions.[152]

The diffusion of acid also plays an important role in photolithography. During the post exposure bake, photo-acid diffused to the active sites within the photoresist film. However, the nanoscale diffusion of acid on the nanoscale is difficult to investigate. Mason et al. explored the local pH as well as single molecule acid-base kinetics and thermodynamics of polymer photo resist films.[141, 148]

The local pH changes in microfluidic devices can also be indicated via fluorescent probes. Mai et al. investigated the impact of concentration polarization induced pH distribution via the assistance of C-snarf-1.[153] As showed in Figure 1.14, a nanoporous polyacrylamide constriction was fabricated inside a microfluidic device through photo polymerization. An electric field was applied across the nanoporous constriction and PBS buffers were placed in the microfluidic device at the beginning. The dynamic on-chip pH change across the nanoporous constriction could be mapped by the dye molecules loaded in the microfluidic channels.

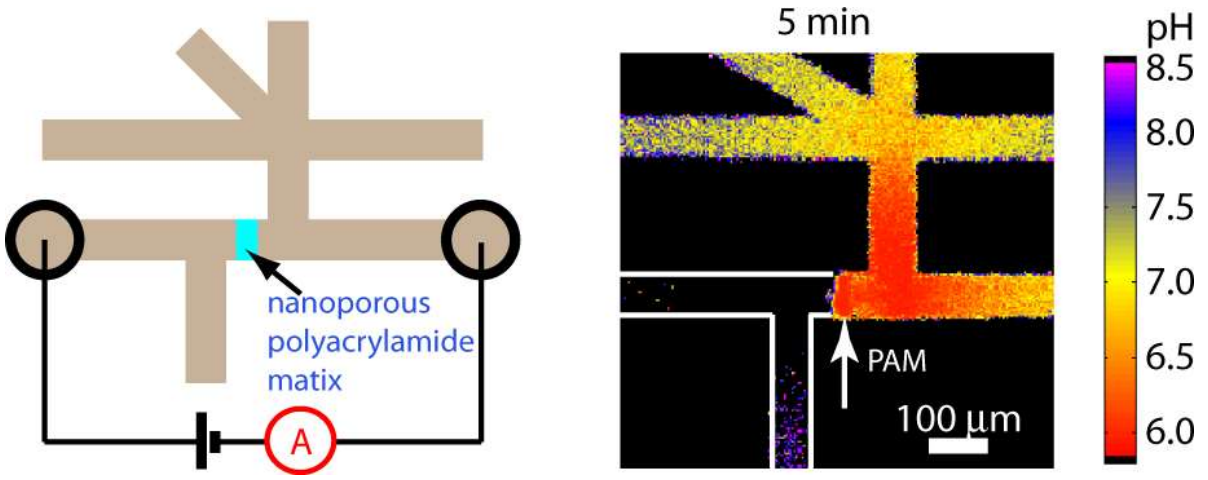

Figure 1.14 (a) Schematic illustration of nanoporous matrix clogged microfluidic device for concentration polarization induced pH distribution measurement. (b) The pH distribution of PBS buffer after the applying of electric field.

1.2.4 SM study of local acidity of mesoporous structure

The investigation of the acidity of meso or micro porous structure on the single molecular level is rare. Dr. Higgins' group investigated the acidity distribution of pure silica thin film exposed to buffer solution with various pH values.[134] Recently, this work was further extended to the acidity distribution within porous aluminosilicate thin films.[157] The calibration curve of R value versus pH was achieved by treating the silicate thin film with buffer solution at various pH values. The emission ratio of dye molecule entrapped in aluminosilicate mesoporous thin films with different Al/Si ratio is shown in Figure 8. The acidity of the films could be measured by comparing the emission ratio of C-snarf-1 in these thin films with the calibration curve. The wide distribution of emission ratios in these thin films also indicated the heterogeneity of acidity within the mesoporous aluminosilicate thin films (Figure 1.15).

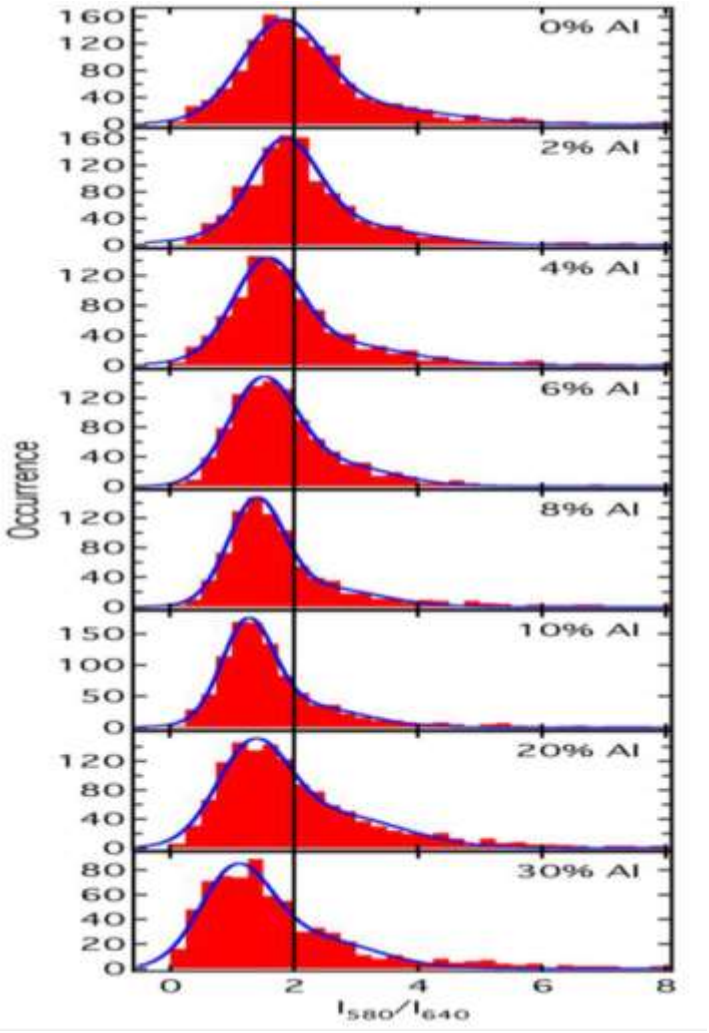

Figure 1.15 Histograms of SM emission ratios, I_{580}/I_{640}, obtained from a series of Al-Si thin films. Approximately 20 distinct images were analyzed in preparation of each histogram. The histograms were fitted to double Gaussian functions (solid blue lines). A vertical line at $I_{580}/I_{640} = 2$ has been appended to aid in visualization of the Al-dependent trend.

In addition, the acid sites in mesoporous or microporous structures can be probed via an acid catalyzed reaction. As exhibited in Figure 1.16, furfuryl alcohol, which is not fluorescent, can undergo self-condensation reaction catalyzed by the acid sites in the pores of mesoporous or microporous structure.[154, 155] The products of self-condensation are fluorescent. Consequently, the self-condensation reaction can be applied for the mapping of acidity in the pores of catalysts. Furthermore, due to the small size of furfuryl alcohol molecules, the acidity of microporous

structure such as ZSM-5 can also be analyzed with them as fluorescent probes.[156] Spatial difference of acidity and catalysis activity on the surface of ZSM-5 is mapped with assistance of furfuryl alcohol.[156]

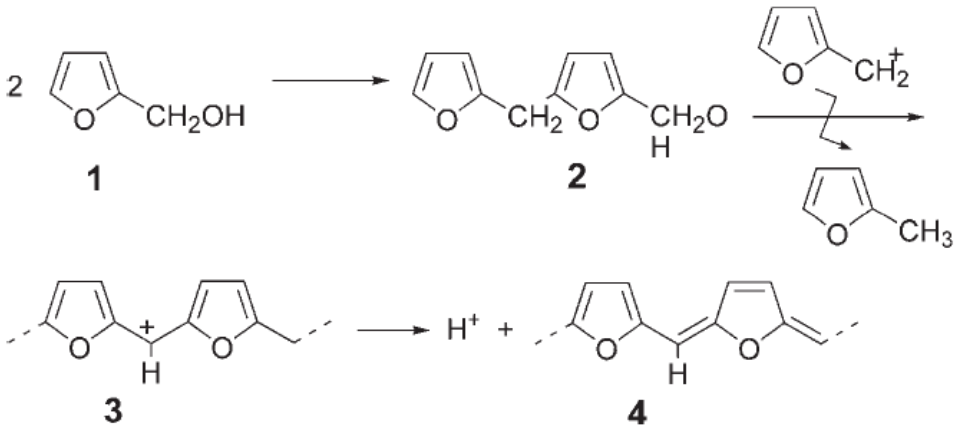

Figure 1.16 Schematic illustration of acid-catalyzed self-condensation reaction of furfuryl alcohol.

1.2.5 Summary

The heterogeneity of catalyst materials is investigated with recent developed techniques. Among all there techniques, single molecules fluorescent spectroscopy is demonstrated as a powerful strategy for the catalysts heterogeneity study. In the case of mesoporous silicate catalysts, although the pore diffusion of dye molecules is investigated with SM method, the research on the acidity on these materials as catalysts is scarce.

In this dissertation, the hydrogen production from higher hydrocarbons via bimetallic catalysts loaded on ceria based supports is first discussed in chapter 2; the acidity study of the porous structure of the mesoporous silicate thin film via single molecule spectroscopy is then

discussed in chapter 3. In chapter 4, the acidity variation through a gradient aluminosilicate thin film is investigated through single molecule spectroscopy with C-snarf-1 as a dye probe.

References

1. Navarro, R. M., Pena, M. A. & Fierro, J. L. G. Hydrogen production reactions from carbon feedstocks: Fossils fuels and biomass. *Chem. Rev.* **107**, 3952-3991 (2007).

2. Ghenciu, A. Review of fuel processing catalysts for hydrogen production in PEM fuel cell systems. *Curr. Opin. Solid State Mat. Sci.* **6**, 389-399 (2002).

3. Ni, M., Leung, M. K. H., Leung, D. Y. C. & Sumathy, K. A review and recent developments in photocatalytic water-splitting using TiO_2 for hydrogen production. *Renew. Sust. Energ. Rev.* **11**, 401-425 (2007).

4. Haryanto, A., Fernando, S., Murali, N. & Adhikari, S. Current status of hydrogen production techniques by steam reforming of ethanol: A review. *Energy Fuels* **19**, 2098-2106 (2005).

5. Navarro, R., Pena, M. & Fierro, J. Hydrogen production reactions from carbon feedstocks: fossil fuels and biomass. *Chem. Rev.* **107**, 3952-3991 (2007).

6. Uemiya, S. Brief review of steam reforming using a metal membrane reactor. *Top. Catal.* **29**, 79-84 (2004).

7. Enger, B. C., Lodeng, R. & Holmen, A. A review of catalytic partial oxidation of methane to synthesis gas with emphasis on reaction mechanisms over transition metal catalysts. *Appl. Catal. A* **346**, 1-27 (2008).

8. Rostrup-Nielsen, J. Syngas in perspective. *Catal. Today* **71**, 243-247 (2002).

9. Lenz, B. & Aicher, T. Catalytic autothermal reforming of Jet fuel. *J. Power Sources* **149**, 44-52 (2005).

10. Takeguchi, T., Furukawa, S., Inoue, M. & Eguchi, K. Autothermal reforming of methane over Ni catalysts supported over CaO-CeO_2-ZrO_2 solid solution. *Appl. Catal. A* **240**, 223-233 (2003).

11. Ming, Q., Healey, T., Allen, L. & Irving, P. Steam reforming of hydrocarbon fuels. *Catal. Today* **77**, 51-64 (2002).

12. Dauenhauer, P., Salge, J. & Schmidt, L. Renewable hydrogen by autothermal steam reforming of volatile carbohydrates. *J. Catal.* **244**, 238-247 (2006).

13. Iglesia, E., Spivey, J. J. & Fleisch, T. H. in *Natural Gas Conversion 6* (Elsevier Science, 2001).

14. Springmann, S., Friedrich, G., Himmen, M., Sommer, M. & Eigenberger, G. Isothermal kinetic measurements for hydrogen production from hydrocarbon fuels using a novel kinetic reactor concept. *Appl. Catal. A* **235**, 101-111 (2002).

15. Krummenacher, J. J., West, K. N. & Schmidt, L. D. Catalytic partial oxidation of higher hydrocarbons at millisecond contact times: decane, hexadecane, and diesel fuel. *J. Catal.* **215**, 332-343 (2003).

16. Li, B., Maruyama, K., Nurunnabi, M., Kunimori, K. & Tomishige, K. Temperature profiles of alumina-supported noble metal catalysts in autothermal reforming of methane. *Appl. Catal. A* **275**, 157-172 (2004).
17. Tonfishige, K., Kanazawa, S., ITO, S. I. & Kunimori, K. Catalyst development for direct heat supply from combustion to reforming in methane reforming with CO_2 and O_2. *Appl. catal. A* **244**, 71-82 (2003).
18. Ayabe, S. *et al*. Catalytic autothermal reforming of methane and propane over supported metal catalysts. *Appl. Catal. A* **241**, 261-269 (2003).
19. Claridge, J. B. *et al*. A study of carbon deposition on catalysts during the partial oxidation of methane to synthesis gas. *Catal. Lett.* **22**, 299-305 (1993).
20. Christensen, K. O., Chen, D., Lødeng, R. & Holmen, A. Effect of supports and Ni crystal size on carbon formation and sintering during steam methane reforming. *Appl. Catal. A* **314**, 9-22 (2006).
21. Bengaard, H. S. *et al*. Steam reforming and graphite formation on Ni catalysts. *J. Catal.* **209**, 365-384 (2002).
22. Parizotto, N. *et al*. Alumina-supported Ni catalysts modified with silver for the steam reforming of methane: Effect of Ag on the control of coke formation. *Appl. Catal. A* **330**, 12-22 (2007).
23. Laosiripojana, N. & Assabumrungrat, S. Methane steam reforming over Ni/Ce–ZrO_2 catalyst: Influences of Ce–ZrO_2 support on reactivity, resistance toward carbon formation, and intrinsic reaction kinetics. *Appl. Catal. A* **290**, 200-211 (2005).
24. Cheekatamarla, P. K. & Lane, A. M. Catalytic autothermal reforming of diesel fuel for hydrogen generation in fuel cells: II. Catalyst poisoning and characterization studies. *J. Power Sources* **154**, 223-231 (2006).
25. Hepola, J. & Simell, P. Sulphur poisoning of nickel-based hot gas cleaning catalysts in synthetic gasification gas: II. Chemisorption of hydrogen sulphide. *Appl. Catal. B* **14**, 305-321 (1997).
26. Hepola, J. & Simell, P. Sulphur poisoning of nickel-based hot gas cleaning catalysts in synthetic gasification gas: I. Effect of different process parameters. *Appl. Catal. B* **14**, 287-303 (1997).
27. Cheekatamarla, P. K. & Lane, A. M. Catalytic autothermal reforming of diesel fuel for hydrogen generation in fuel cells: I. Activity tests and sulfur poisoning. *J. Power Sources* **152**, 256-263 (2005).
28. Dias, J. A. C. & Assaf, J. M. Autothermal reforming of methane over Ni/γ-Al_2O_3 promoted with Pd: The effect of the Pd source in activity, temperature profile of reactor and in ignition. *Appl. Catal. A* **334**, 243-250 (2008).
29. Ma, L. & Trimm, D. Alternative catalyst bed configurations for the autothermic conversion of methane to hydrogen. *Appl. Catal. A* **138**, 265-273 (1996).

30. Avcı, A. K., Trimm, D. L., Aksoylu, A. E. & Önsan, Z. I. Hydrogen production by steam reforming of n-butane over supported Ni and Pt-Ni catalysts. *Appl. Catal. A* **258**, 235-240 (2004).
31. Mukainakano, Y. *et al*. Catalytic performance and characterization of Pt–Ni bimetallic catalysts for oxidative steam reforming of methane. *Chem. Eng. Sci.* **63**, 4891-4901 (2008).
32. Dias, J. A. C. & Assaf, J. M. Autothermal reforming of methane over Ni/γ-Al_2O_3 catalysts: the enhancement effect of small quantities of noble metals. *J. Power Sources* **130**, 106-110 (2004).
33. Strohm, J. J., Zheng, J. & Song, C. Low-temperature steam reforming of jet fuel in the absence and presence of sulfur over Rh and Rh–Ni catalysts for fuel cells. *J. Catal.* **238**, 309-320 (2006).
34. Kaila, R. K. *et al*. Zirconia-supported bimetallic RhPt catalysts: Characterization and testing in autothermal reforming of simulated gasoline. *Appl. Catal. B* **84**,223-232 (2008).
35. Navarro, R., Alvarez-Galvan, M., Rosa, F. & Fierro, J. Hydrogen production by oxidative reforming of hexadecane over Ni and Pt catalysts supported on Ce/La-doped Al_2O_3. *Appl. Catal. A* **297**, 60-72 (2006).
36. Tang, S., Lin, J. & Tan, K. Partial oxidation of methane to syngas over Ni/MgO, Ni/CaO and Ni/CeO_2. *Catal. Lett.* **51**, 169-175 (1998).
37. Kang, Z. & Wang, Z. L. Novel oxides for cycled hydrogen production from methane and water using a temperature swing. *Adv. Mater* **15**, 521-526 (2003).
38. Chowdhury, S. & Lin, K. S. Synthesis and characterization of 1D ceria nanomaterials for CO oxidation and steam reforming of methanol. *J. Nanomater.* 2011, **9**, 157690 (2011).
39. Hsiao, W. I., Lin, Y. S., Chen, Y. C. & Lee, C. S. The effect of the morphology of nanocrystalline CeO_2 on ethanol reforming. *Chem. Phys. Lett.* **441**, 294-299 (2007).
40. Godinho, M. *et al*. Gadolinium-doped cerium oxide nanorods: novel active catalysts for ethanol reforming. *J. Mater. Sci.* **45**, 593-598 (2010).
41. Neltner, B. *et al*. Production of hydrogen using nanocrystalline protein-templated catalysts on M13 phage. *ACS Nano* **4**, 3227-3235 (2010).
42. Chen, H. *et al*. Autothermal reforming of ethanol for hydrogen production over perovskite $LaNiO_3$. *Chem. Eng. J.* **160**, 333-339 (2010).
43. Kondakindi, R. R. *et al*. Characterization and activity of perovskite catalysts for autothermal reforming of dodecane. *Appl. Catal. A* **390**, 271-280 (2010).
44. Qi, A., Wang, S., Fu, G., Ni, C. & Wu, D. La–Ce–Ni–O monolithic perovskite catalysts potential for gasoline autothermal reforming system. *Appl. Catal. A* **281**, 233-246 (2005).
45. Erri, P., Dinka, P. & Varma, A. Novel perovskite-based catalysts for autothermal JP-8 fuel reforming. *Chem. Eng. Sci.* **61**, 5328-5333 (2006).

46. Dinka, P. & Mukasyan, A. S. Perovskite catalysts for the auto-reforming of sulfur containing fuels. *J. Power Sources* **167**, 472-481 (2007).
47. Kugai, J., Velu, S. & Song, C. Low-temperature reforming of ethanol over CeO 2-supported Ni-Rh bimetallic catalysts for hydrogen production. *Catal. Lett.***101**, 255-264 (2005).
48. Deluga, G., Salge, J., Schmidt, L. & Verykios, X. Renewable hydrogen from ethanol by autothermal reforming. *Science* **303**, 993-997 (2004).
49. Shen, J. P. & Song, C. Influence of preparation method on performance of Cu/Zn-based catalysts for low-temperature steam reforming and oxidative steam reforming of methanol for H_2 production for fuel cells. *Catal. Today* **77**, 89-98 (2002).
50. Alvarez-Galvan, M. *et al*. Performance of La, Ce-modified alumina-supported Pt and Ni catalysts for the oxidative reforming of diesel hydrocarbons. *Int. J. Hydrogen Energy* **33**, 652-663 (2008).
51. Mota, N., Alvarez-Galvan, M. C., Al-Zahrani, S. M., Navarro, R. M. & Fierro, J. L. G. Diesel fuel reforming over catalysts derived from $LaCo_{1-x}Ru_xO_3$ perovskites with high Ru loading. *Int. J. Hydrogen Energy* **37**, 7056-7066 (2012).
52. Dreyer, B., Lee, I., Krummenacher, J. & Schmidt, L. Autothermal steam reforming of higher hydrocarbons: n-Decane, n-hexadecane, and JP-8. *Appl. Catal. A* **307**, 184-194 (2006).
53. Gould, B. D., Tadd, A. R. & Schwank, J. W. Nickel-catalyzed autothermal reforming of jet fuel surrogates: n-Dodecane, tetralin, and their mixture. *J. Power Sources* **164**, 344-350 (2007).
54. Moon, D. J., Ryu, J. W., Lee, S. D., Lee, B. G. & Ahn, B. S. Ni-based catalyst for partial oxidation reforming of iso-octane. *Appl. Catal. A* **272**, 53-60 (2004).
55. Kang, I., Bae, J. & Bae, G. Performance comparison of autothermal reforming for liquid hydrocarbons, gasoline and diesel for fuel cell applications. *J. Power Sources* **163**, 538-546 (2006).
56. Xue, Q., Gao, L. & Lu, Y. Sulfur-tolerant Pt/Gd_2O_3-CeO_2-Al_2O_3 catalyst for high efficiency H_2 production from autothermal reforming of retail gasoline. *Catal. Today* **146**, 103-109 (2009).
57. Cheekatamarla, P. K. & Lane, A. M. Efficient bimetallic catalysts for hydrogen generation from diesel fuel. *Int. J. Hydrogen Energy* **30**, 1277-1285 (2005).
58. Weckhuysen, B. M. Chemical imaging of spatial heterogeneities in catalytic solids at different length and time scales. *Angew. Chem. Int. Ed.* **48**, 4910-4943 (2009).
59. Buurmans, I. L. & Weckhuysen, B. M. Heterogeneities of individual catalyst particles in space and time as monitored by spectroscopy. *Nat. Chem.* **4**, 873-886 (2012).

60. Meziani, M. *et al*. Number and strength of surface acidic sites on porous aluminosilicates of the MCM-41 type inferred from a combined microcalorimetric and adsorption study. *Langmuir* **16**, 2262-2268 (2000).

61. Rivera, D. & Harris, J. M. In situ ATR-FT-IR kinetic studies of molecular transport and surface binding in thin sol-gel films: reactions of chlorosilane reagents in porous silica materials. *Anal. Chem.* **73**, 411-423 (2001).

62. Beck, J. *et al*. A new family of mesoporous molecular sieves prepared with liquid crystal templates. *J. Am. Chem. Soc.* **114**, 10834-10843 (1992).

63. Gill, C. S., Price, B. A. & Jones, C. W. Sulfonic acid-functionalized silica-coated magnetic nanoparticle catalysts. *J. Catal.* **251,** 145-152 (2007).

64. Ertl, G. Reactions at surfaces: From atoms to complexity (Nobel lecture). *Angew. Chem. Int. Ed.* **47**, 3524-3535 (2008).

65. de Smit, E. *et al*. Nanoscale chemical imaging of a working catalyst by scanning transmission X-ray microscopy. *Nature* **456**, 222-225 (2008).

66. Higgins, S. J. & Nichols, R. J. Single-molecule imaging: Catalysts under the microscope. *Nat. Nanotechnol.* **2**, 270-271 (2007).

67. Hulsken, B. *et al*. Real-time single-molecule imaging of oxidation catalysis at a liquid–solid interface. *Nat. Nanotechnol.* **2**, 285-289 (2007).

68. van Schrojenstein Lantman, Evelien M, Deckert-Gaudig, T., Mank, A. J., Deckert, V. & Weckhuysen, B. M. Catalytic processes monitored at the nanoscale with tip-enhanced Raman spectroscopy. *Nat. Nanotechnol.* **7**, 583-586 (2012).

69. Roeffaers, M. B. *et al*. Single-molecule fluorescence spectroscopy in (bio)catalysis. *Proc. Natl. Acad. Sci. U. S. A.* **104**, 12603-12609 (2007).

70. Esfandiari, N. M. & Blum, S. A. Homogeneous vs heterogeneous polymerization catalysis revealed by single-particle fluorescence microscopy. *J. Am. Chem. Soc.* **133**, 18145-18147 (2011).

71. Roeffaers, M. B. *et al*. Spatially resolved observation of crystal-face-dependent catalysis by single turnover counting. *Nature* **439**, 572-575 (2006).

72. Andoy, N. M. *et al*. Single-molecule catalysis mapping quantifies site-specific activity and uncovers radial activity gradient on single 2D nanocrystals. *J. Am. Chem. Soc.* **135**, 1845-1852 (2013).

73. Xu, W., Kong, J. S., Yeh, Y. E. & Chen, P. Single-molecule nanocatalysis reveals heterogeneous reaction pathways and catalytic dynamics. *Nat. Mater.* **7**, 992-996 (2008).

74. Sambur, J. B. & Chen, P. Approaches to single-nanoparticle catalysis. *Annu. Rev. Phys. Chem.* **65**, 395-422 (2014).

75. Ochoa, M. A., Chen, P. & Loring, R. F. Single Turnover Measurements of Nanoparticle Catalysis Analyzed with Dwell Time Correlation Functions and Constrained Mean Dwell Times. *J. Phys. Chem. C* **117**, 19074-19081 (2013).

76. Shen, H., Zhou, X., Zou, N. & Chen, P. Single-Molecule Kinetics Reveals a Hidden Surface Reaction Intermediate in Single-Nanoparticle Catalysis. *J. Phys. Chem. C* **118**, 26902-26911 (2014).

77. Han, K. S., Liu, G., Zhou, X., Medina, R. E. & Chen, P. How does a single Pt nanocatalyst behave in two different reactions? A single-molecule study. *Nano. Lett.* **12**, 1253-1259 (2012).

78. Chen, T. *et al*. Catalytic Kinetics of Different Types of Surface Atoms on Shaped Pd Nanocrystals. *Angew. Chem.**128**, 1871-1875* (2016).

79. Zhou, X. *et al*. Quantitative super-resolution imaging uncovers reactivity patterns on single nanocatalysts. *Nat. Nanotechnol.* **7**, 237-241 (2012).

80. Shen, H., Xu, W. & Chen, P. Single-molecule nanoscale electrocatalysis. *Phys. Chem. Chem. Phys.* **12**, 6555-6563 (2010).

81. Xu, W. *et al*. Single-molecule electrocatalysis by single-walled carbon nanotubes. *Nano. Lett.* **9**, 3968-3973 (2009).

82. Naito, K., Tachikawa, T., Fujitsuka, M. & Majima, T. Single-molecule observation of photocatalytic reaction in TiO2 nanotube: importance of molecular transport through porous structures. *J. Am. Chem. Soc.* **131**, 934-936 (2008).

83. Takahara, I., Saito, M., Inaba, M. & Murata, K. Dehydration of ethanol into ethylene over solid acid catalysts. *Catal. Lett.* **105**, 249-252 (2005).

84. Onda, A., Ochi, T. & Yanagisawa, K. Selective hydrolysis of cellulose into glucose over solid acid catalysts. *Green Chem.* **10**, 1033-1037 (2008).

85. Tanabe, K. & Hölderich, W. F. Industrial application of solid acid–base catalysts. *Appl. Catal. A* **181**, 399-434 (1999).

86. Lai, D. *et al*. Hydrolysis of cellulose into glucose by magnetic solid acid. *ChemSusChem* **4**, 55-58 (2011).

87. Crisci, A. J. *et al*. Acid-functionalized SBA-15-type silica catalysts for carbohydrate dehydration. *ACS Catal.* **1**, 719-728 (2011).

88. Guo, X. *et al*. Selective dehydration of fructose to 5-hydroxymethylfurfural catalyzed by mesoporous SBA-15-SO3H in ionic liquid BmimCl. *Carbohydr. Res.* **351**, 35-41 (2012).

89. Herrera, J. E., Kwak, J. H., Hu, J. Z., Wang, Y. & Peden, C. H. Effects of novel supports on the physical and catalytic properties of tungstophosphoric acid for alcohol dehydration reactions. *Top. Catal.* **49**, 259-267 (2008).
90. Zeidan, R. K., Hwang, S. & Davis, M. E. Multifunctional heterogeneous catalysts: SBA‐15‐containing primary amines and sulfonic acids. *Angew. Chem. Int. Ed.* **45**, 6332-6335 (2006).
91. Mbaraka, I. K. & Shanks, B. H. Acid strength variation due to spatial location of organosulfonic acid groups on mesoporous silica. *J. Catal.* **244**, 78-85 (2006).
92. Martínez, A., López, C., Márquez, F. & Díaz, I. Fischer–Tropsch synthesis of hydrocarbons over mesoporous Co/SBA-15 catalysts: the influence of metal loading, cobalt precursor, and promoters. *J. Catal.* **220**, 486-499 (2003).
93. Xiong, H., Zhang, Y., Liew, K. & Li, J. Fischer–Tropsch synthesis: The role of pore size for Co/SBA-15 catalysts. *J. Mol. Catal. A: Chem.* **295**, 68-76 (2008).
94. Weisz, P. B. Molecular shape selective catalysis. *Pure Appl. Chem.* **52**, 2091-2103 (1980).
95. Verheyen, E. *et al*. Molecular shape-selectivity of MFI zeolite nanosheets in n-decane isomerization and hydrocracking. *J. Catal.* **300**, 70-80 (2013).
96. Yu, Y. *et al*. The role of shape selectivity in catalytic fast pyrolysis of lignin with zeolite catalysts. *Appl. Catal. A* **447**, 115-123 (2012).
97. Jones, C. W., Tsuji, K. & Davis, M. E. Organic-functionalized molecular sieves as shape-selective catalysts. *Nature* **393**, 52-54 (1998).
98. Dusselier, M., Van Wouwe, P., Dewaele, A., Jacobs, P. A. & Sels, B. F. Shape-selective zeolite catalysis for bioplastics production. *Science* **349**, 78-80 (2015).
99. Agirrezabal-Telleria, I., Requies, J., Güemez, M. & Arias, P. Pore size tuning of functionalized SBA-15 catalysts for the selective production of furfural from xylose. *Appl. Catal. B* **115**, 169-178 (2012).
100. Chen, Z. *et al*. Diffusion induced reactant shape selectivity inside mesoporous pores of Pd@ meso-SiO_2 nanoreactor in Suzuki coupling reactions. *J. Phys. Chem. C* **116**, 14986-14991 (2012).
101. Hoo, P. & Abdullah, A. Z. Direct synthesis of mesoporous 12-tungstophosphoric acid SBA-15 catalyst for selective esterification of glycerol and lauric acid to monolaurate. *Chem. Eng. J.* **250**, 274-287 (2014).
102. Pérez-Pariente, J., Díaz, I., Mohino, F. & Sastre, E. Selective synthesis of fatty monoglycerides by using functionalised mesoporous catalysts. *Appl. Catal. A* **254**, 173-188 (2003).
103. Jérôme, F., Pouilloux, Y. & Barrault, J. Rational design of solid catalysts for the selective use of glycerol as a natural organic building block. *ChemSusChem* **1**, 586-613 (2008).

104. Fan, R., Huh, S., Yan, R., Arnold, J. & Yang, P. Gated proton transport in aligned mesoporous silica films. *Nat. mater.* **7**, 303-307 (2008).
105. Faustini, M. *et al*. Bottom-up approach toward titanosilicate mesoporous pillared planar nanochannels for nanofluidic applications. *Chem. Mater.* **22**, 5687-5694 (2010).
106. Yamaguchi, A., Kaneda, H., Fu, W. & Teramae, N. Structural Control of Surfactant‐Templated Mesoporous Silica Formed Inside Columnar Alumina Pores. *Adv. Mater.* **20**, 1034-1037 (2008).
107. Eijkel, J. C. & Van Den Berg, A. Nanofluidics: what is it and what can we expect from it? *Microfluid Nanofluid.* **1**, 249-267 (2005).
108. Höltzel, A. & Tallarek, U. Ionic conductance of nanopores in microscale analysis systems: Where microfluidics meets nanofluidics. *J. Sep. Sci.* **30**, 1398-1419 (2007).
109. Chen, Y., Ni, Z., Wang, G., Xu, D. & Li, D. Electroosmotic flow in nanotubes with high surface charge densities. *Nano. Lett.* **8**, 42-48 (2008).
110. Daiguji, H., Yang, P., Szeri, A. J. & Majumdar, A. Electrochemomechanical energy conversion in nanofluidic channels. *Nano. Lett.* **4**, 2315-2321 (2004).
111. Yan, R., Liang, W., Fan, R. & Yang, P. Nanofluidic diodes based on nanotube heterojunctions. *Nano. Lett.* **9**, 3820-3825 (2009).
112. Daiguji, H., Yang, P. & Majumdar, A. Ion transport in nanofluidic channels. *Nano. Lett.* **4**, 137-142 (2004).
113. Wei, D. *et al*. Atomic layer deposition TiO2–Al2O3 stack: An improved gate dielectric on Ga-polar GaN metal oxide semiconductor capacitors. *J. Vac. Sci. Technol. B* **32**, 060602 (2014).
114. Wei, D. *et al*. Influence of Atomic Layer Deposition Temperatures on TiO2/n-Si MOS Capacitor. *ECS J. Solid State Sci. Technol.* **2**, N110-N114 (2013).
115. Kuo, T. *et al*. Gateable nanofluidic interconnects for multilayered microfluidic separation systems. *Anal. Chem.* **75**, 1861-1867 (2003).
116. Karnik, R., Castelino, K., Fan, R., Yang, P. & Majumdar, A. Effects of biological reactions and modifications on conductance of nanofluidic channels. *Nano. Lett.* **5**, 1638-1642 (2005).
117. Fu, Y., Ye, F., Sanders, W. G., Collinson, M. M. & Higgins, D. A. Single molecule spectroscopy studies of diffusion in mesoporous silica thin films. *J. Phys. Chem. B* **110**, 9164-9170 (2006).
118. Mahurin, S., Dai, S. & Barnes, M. Probing the diffusion of a dilute dye solution in mesoporous glass with fluorescence correlation spectroscopy. *J. Phys. Chem. B* **107**, 13336-13340 (2003).
119. Xu, H. *et al*. Imaging fluorescence correlation spectroscopy studies of dye diffusion in self-assembled organic nanotubes. *Phys. Chem. Chem. Phys.**18**, 16766-16774* (2016).

120. Kirstein, J. *et al*. Exploration of nanostructured channel systems with single-molecule probes. *Nat. Mater.* **6**, 303-310 (2007).
121. Saxton, M. J. & Jacobson, K. Single-particle tracking: applications to membrane dynamics. *Annu. Rev. Biophys. Biomol. Struct.* **26**, 373-399 (1997).
122. Saxton, M. J. Single-particle tracking: the distribution of diffusion coefficients. *Biophys. J.* **72**, 1744-1753 (1997).
123. Jung, C. *et al*. Diffusion of oriented single molecules with switchable mobility in networks of long unidimensional nanochannels. *J. Am. Chem. Soc.* **130**, 1638-1648 (2008).
124. Jung, C., Hellriegel, C., Michaelis, J. & Bräuchle, C. Single‐Molecule Traffic in Mesoporous Materials: Translational, Orientational, and Spectral Dynamics. *Adv. Mater.* **19**, 956-960 (2007).
125. Zürner, A., Kirstein, J., Döblinger, M., Bräuchle, C. & Bein, T. Visualizing single-molecule diffusion in mesoporous materials. *Nature* **450**, 705-708 (2007).
126. Ito, S. *et al*. Microscopic Structure and Mobility of Guest Molecules in Mesoporous Hybrid Organosilica: Evaluation with Single-Molecule Tracking. *J. Phys. Chem. C* **113**, 11884-11891 (2009).
127. Seebacher, C., Hellriegel, C., Bräuchle, C., Ganschow, M. & Wöhrle, D. Orientational behavior of single molecules in molecular sieves: A study of oxazine dyes in $AlPO_4$-5 crystals. *J. Phys. Chem. B* **107**, 5445-5452 (2003).
128. Kumarasinghe, R., Higgins, E. D., Ito, T. & Higgins, D. A. Spectroscopic and Polarization-Dependent Single-Molecule Tracking Reveal the One-Dimensional Diffusion Pathways in Surfactant-Templated Mesoporous Silica. *J. Phys. Chem. C* **120**, 715-723 (2015).
129. Han, J. & Burgess, K. Fluorescent indicators for intracellular pH. *Chem. Rev.* **110**, 2709-2728 (2009).
130. Ribou, A., Vigo, J. & Salmon, J. C-snarf-1 as a fluorescent probe for pH measurements in living cells: Two-wavelength-ratio method versus whole-spectral-resolution method. *J. Chem. Educ.* **79**, 1471 (2002).
131. Han, J., Loudet, A., Barhoumi, R., Burghardt, R. C. & Burgess, K. A ratiometric pH reporter for imaging protein-dye conjugates in living cells. *J. Am. Chem. Soc.* **131**, 1642-1643 (2009).
132. Van Erp, P. E., Jansen, M. J., De Jongh, G. J., Boezeman, J. & Schalkwijk, J. Ratiometric measurement of intracellular pH in cultured human keratinocytes using carboxy‐SNARF‐1 and flow cytometry. *Cytometry* **12**, 127-132 (1991).
133. Hunter, R. C. & Beveridge, T. J. Application of a pH-sensitive fluoroprobe (C-snarf-4) for pH microenvironment analysis in Pseudomonas aeruginosa biofilms. *Appl. Environ. Microbiol.* **71**, 2501-2510 (2005).

134. Fu, Y., Collinson, M. M. & Higgins, D. A. Single-molecule spectroscopy studies of microenvironmental acidity in silicate thin films. *J. Am. Chem. Soc.* **126**, 13838-13844 (2004).
135. Whitaker, J. E., Haugland, R. P. & Prendergast, F. G. Spectral and photophysical studies of benzo [c] xanthene dyes: dual emission pH sensors. *Anal. Biochem.* **194**, 330-344 (1991).
136. Brasselet, S. & Moerner, W. Fluorescence Behavior of Single-Molecule pH-Sensors. *Single Molecules* **1**, 17-23 (2000).
137. Venn, A. A. *et al*. Imaging intracellular pH in a reef coral and symbiotic anemone. *Proc. Natl. Acad. Sci. U. S. A.* **106**, 16574-16579 (2009).
138. Bassnett, S., Reinisch, L. & Beebe, D. C. Intracellular pH measurement using single excitation-dual emission fluorescence ratios. *Am. J. Physiol.* **258**, C171-8 (1990).
139. House, C. Confocal ratio-imaging of intercellular pH in unfertilised mouse oocytes. *Zygote* **2**, 37-45 (1994).
140. Seemann, K. M., Kiefersauer, R., Jacob, U. & Kuhn, B. Optical pH detection within a protein crystal. *J. Phys. Chem. B* **116**, 9873-9881 (2012).
141. Mason, M. D., Ray, K., Pohlers, G., Cameron, J. F. & Grober, R. D. Probing the local pH of polymer photoresist films using a two-color single molecule nanoprobe. *J. Phys. Chem. B* **107**, 14219-14224 (2003).
142. Srivastava, A. & Krishnamoorthy, G. Time-resolved fluorescence microscopy could correct for probe binding while estimating intracellular pH. *Anal. Biochem.* **249**, 140-146 (1997).
143. Owen, C. S., Carango, P., Grammer, S., Bobyock, S. & Leeper, D. B. pH-dependent intracellular quenching of the indicator carboxy-SNARF-1. *J. Fluoresc.* **2**, 75-80 (1992).
144. Večeř, J., Holoubek, A. & Sigler, K. Fluorescence Behavior of the pH‐Sensitive Probe Carboxy SNARF‐1 in Suspension of Liposomes. *Photochem. Photobiol.* **74**, 8-13 (2001).
145. Chen, Y., Ostafin, A. & Mizukami, H. Synthesis and characterization of pH sensitive carboxySNARF-1 nanoreactors. *Nanotechnology* **21**, 215503 (2010).
146. Salerno, M., Ajimo, J. J., Dudley, J. A., Binzel, K. & Urayama, P. Characterization of dual-wavelength seminaphthofluorescein and seminapthorhodafluor dyes for pH sensing under high hydrostatic pressures. *Anal. Biochem.* **362**, 258-267 (2007).
147. DePedro, H. M. & Urayama, P. Using LysoSensor Yellow/Blue DND-160 to sense acidic pH under high hydrostatic pressures. *Anal. Biochem.* **384**, 359-361 (2009).
148. Mason, M. D., Ray, K., Grober, R. D., Pohlers, G. & Cameron, J. Single molecule acid-base kinetics and thermodynamics. *Phys. Rev. Lett.* **93**, 073004 (2004).

149. Charier, S. *et al*. Reactant concentrations from fluorescence correlation spectroscopy with tailored fluorescent probes. An example of local calibration-free pH measurement. *J. Am. Chem. Soc.* **127**, 15491-15505 (2005).

150. Widengren, J., Terry, B. & Rigler, R. Protonation kinetics of GFP and FITC investigated by FCS—aspects of the use of fluorescent indicators for measuring pH. *Chem. Phys.* **249**, 259-271 (1999).

151. Wong, F. H., Banks, D. S., Abu-Arish, A. & Fradin, C. A molecular thermometer based on fluorescent protein blinking. *J. Am. Chem. Soc.* **129**, 10302-10303 (2007).

152. Cheng, J., Soetjipto, C., Hoffmann, M. R. & Colussi, A. Confocal fluorescence microscopy of the morphology and composition of interstitial fluids in freezing electrolyte solutions. *J. Phys. Chem. Lett.* **1**, 374-378 (2009).

153. Mai, J., Miller, H. & Hatch, A. V. Spatiotemporal mapping of concentration polarization induced pH changes at nanoconstrictions. *ACS Nano* **6**, 10206-10215 (2012).

154. Roeffaers, M. B. *et al*. Space-and time-resolved visualization of acid catalysis in ZSM-5 crystals by fluorescence microscopy. *Angew. Chem.* **119**, 1736-1739 (2007).

155. Choura, M., Belgacem, N. M. & Gandini, A. Acid-catalyzed polycondensation of furfuryl alcohol: mechanisms of chromophore formation and cross-linking. *Macromolecules* **29**, 3839-3850 (1996).

156. Ristanović, Z. *et al*. Quantitative 3D Fluorescence Imaging of Single Catalytic Turnovers Reveals Spatiotemporal Gradients in Reactivity of Zeolite H-ZSM-5 Crystals upon Steaming. *J. Am. Chem. Soc.* **137**, 6559-6568 (2015).

157. Sun, X. *et al*. Single-Molecule Studies of Acidity Distributions in Mesoporous Aluminosilicate Thin Films. *Langmuir* **31**, 5667–5675 (2015).

158. Patil, A.S. et al. Portable fuel cell systems for America's army: technology transition to the field. *J. Power Sources* **136***,* 220-225 (2004).

159. DuBois, T.G. et al. Selection and performance comparison of jet fuel surrogates for autothermal reforming. *Fuel* **90**, 1439-1448 (2011).

Chapter 2 - **Autothermal reforming and partial oxidation of n-hexadecane via Pt/Ni bimetallic catalysts on ceria-based supports**

2.1 Introduction

With the development of highly efficient proton-exchange membrane (PEM) fuel cells, hydrogen shows great promise as a clean energy carrier for future power generation. [1, 2] For the mobile application of hydrogen as an energy source in remote areas, the on-site production of hydrogen is considered more economical and safe compared to storage and transportation of hydrogen as a compressed gas. [3-5]

Auto-thermal reforming (ATR) and partial oxidation (POX) are suitable for the on-site production of hydrogen because no external heat source is necessary: [6]

$$C_{16}H_{34}+8O_2+16H_2O=16CO_2+33H_2 \text{ ATR} \quad (2.1)$$

$$C_{16}H_{34}+8O_2=16CO+17H_2 \text{ POX} \quad (2.2)$$

ATR, which can be considered as a combination of steam reforming (SR), POX and the water-gas shift (WGS) reaction, has been suggested to be the most effective for on-site hydrogen generation due to the higher hydrogen production efficiency.[7, 8]

Higher hydrocarbons, which can be transported in liquid form, feature a high volumetric and gravimetric hydrogen density, [9] and are attractive as the fuel for portable hydrogen generation. Thus, ATR of higher hydrocarbons shows great promise for the on-board hydrogen

production due to its high thermal efficiency and compact setup. Previous research has reported on ATR of higher hydrocarbons with various catalysts, including Rh, [10, 11] Pt, [9] and Ni.[12] Although precious metals show higher activity, [13] Ni-based catalysts were widely utilized due to their low cost.[14, 15] However, Ni catalysts are susceptible to deactivation. For example, in ATR of higher hydrocarbons, the production of olefin byproducts [16] and coke [17-19] [20] are problematic. In addition, Ni catalysts have a low resistance to sulfur poisoning,[21] which will be an issue if ATR is used for processing of conventional hydrocarbon fuels.[22]

A bimetallic catalyst where nickel is alloyed with a precious metal offers a potential solution to the high rates of deactivation of Ni in ATR of higher hydrocarbons. [23, 24, 25, 26] For example, Pt /Ni bimetallic catalysts have been investigated for the auto-thermal reforming of gaseous hydrocarbons.[27, 28, 29] The high activity of Pt/Ni bimetallic catalysts for the ATR process was attributed to the enhancement of microscale heat transfer [30] and the suppression of hot spot formation.[31, 32]

The choice of support can also help mitigate catalyst deactivation. Ceria based supports are often utilized to promote catalytic activity and minimize coke formation in ATR of heavy hydrocarbons due to their high oxygen storage capacity and high ionic conductivity.[12, 33, 34, 35, 36, 37] It was reported that Ni/ Ce-ZrO_2 catalysts exhibited high stability and activity for the ATR of various fuels. [38-41, 42, 26, 43] Mixed metal oxides containing cerium have been widely studied as the supports in ATR. When CeO_2 supports were doped with Gd_2O_3, the oxygen mobility was enhanced due to the creation of extrinsic oxygen vacancies in the ceria lattice.[44] Pt loaded on Gd_2O_3 doped CeO_2 (CGO) was highly active for the ATR process and showed excellent sulfur resistance. [44-46]

Prior investigations suggest that bimetallic catalysts on ceria-based supports have great promise for hydrogen production through ATR. Although previous studies have reported ATR of heavy hydrocarbons on bimetallic catalysts on ceria-based supports, studies that compare the catalytic activity of Ni and Pt/Ni catalysts on ceria or ceria-based mixed metal oxide supports are scarce. In this paper we focus on the comparative study of the activity of Pt/Ni bimetallic catalysts loaded on three different ceria base catalysts: Gd_2O_3-CeO_2, CeO_2, and CeO_2-ZrO_2. Another unique feature of this paper is the nature of the bimetallic catalysts. Rather than preparing Pt/Ni catalysts by the successive loading of the catalyst with Pt and Ni, [29, 30] bimetallic Pt/Ni nanoparticles were first prepared and then placed on the support. With this method intimate contact of Pt and Ni was assured, and it is thought that the ratio of Pt to Ni in individual particles can be better controlled.

2.2 Experimental

2.2.1 Materials

Cetyl trimethylammonium bromide (CTAB 99%) was purchased from Amresco. Nickel chloride (98%), chloroplatinic acid solution (8% in H_2O), gadolinium nitrate (99.99%), cerium nitrate (99.99%), and hydrazine monohydrate (N_2H_4 64-65 %, reagent grade, 98%) were obtained from Sigma Aldrich. Cerium oxide was purchased from Nanoscale Materials, Inc. Zirconium (IV) propoxide (23%-28% free alcohol) was obtained from Strem Chemical, INC.

2.2.2 Catalyst and support preparation

Preparation of Pt/Ni bimetallic and Ni nanoparticles

Pt/Ni particles were supplied by collaborators at Nanoscale Corporation (technology subsequently acquired by Timilon Technology Acquisitions) who used a method similar to that

reported by Wu and Chen.[47] In a typical experiment (Pt/Ni 10/90 molar ratio bimetallic nanoparticles), 1.8 g CTAB, 1.9 g $NiCl_2$ and 7 ml chloroplatinic acid solution were dissolved in 1000 mL water. The resulting solution was stirred for 10 min with the protection of nitrogen before 1.3g KOH dissolved in 15ml water was added. Then 730 µL of hydrazine was added drop wise. The final solution was further stirred under nitrogen for 2 h until it turned grey.

Preparation of CeO_2-ZrO_2 support

ZrO_2 was prepared by the sol-gel method. Typically, 126 g of Zirconium propoxide and 25 mL water were dissolved in 300 mL isopropanol and heated to 70 ^oC. The final solution was then rotary evaporated to form white powders.

To prepare the Ce-ZrO_2 support (Ce/Zr molar ratio 1/3), 9.1 g of $Ce(NO_3)_2 \cdot 6H_2O$ dissolved in 50 mL deionized water was mixed with 20 g ZrO_2. The mixture was dried at 110 ^oC under nitrogen. The resulting solid powders were heat treated at 350 ^oC with the protection of nitrogen.

Preparation of Gd_2O_3-CeO_2 support

3.7 g of gadolinium nitrate dissolved in 12 mL water was mixed with 9.2 g cerium oxide. The mixture was dried at 110 ^oC and further heat treated at 350 ^oC under nitrogen.

Loading of nanoparticles onto supports

150 mg of metal nanoparticles suspended in 20 mL chloroform was ultrasonicated for 15 min. The suspension was then mixed with 3.0 g of the support for a few minutes and rotary evaporated. The final powders were dried at 110 ^oC under nitrogen.

2.2.3 Catalytic activity experiments

As shown in Figure 2.1, the reactor consisted of a 19 mm inner diameter quartz tube. N-hexadecane (95% purity, boiling point 287 ^oC) was preheated and fed through a homemade nebulizer into the reactor. The homemade nebulizer was made of a 1/8'' Swagelok stainless steel

tube as the inner tube and one ¼'' Swagelok stainless steel tube as the outer tube. A mixture of nitrogen and oxygen flowed through the inner tube, while hexadecane flowed between the two tubes. Both the inner and outer tubes were reduced at the end of the nebulizer. A steel nozzle was also attached at the end of nebulizer to prevent the back flow of hexadecane droplets. The n-hexadecane was pumped through the nebulizer via a CP DSM pump (Valco Instruments Co.Inc). The upstream reactor walls were heated to 250 ^{o}C to prevent condensation of n-hexadecane. Water was pumped into the upstream area via a 5967 optos pump ISPM (Eldex Laboratories, Inc), evaporated into steam and preheated. Nitrogen and oxygen were fed from two high pressure cylinders, and their flow rates were controlled by two mass flow controllers (DX5 Digital Control System Unit instruments). The nitrogen flow rate was maintained at 2 standard liters per minute (SLPM). The flow rate of oxygen was changed according to the specified reaction condition. Two uncoated 1.7 cm outer diameter (o.d.), and 1.0 cm length α-alumina (91 % a-Al_2O_3, 9 % SiO_2 Ask chemicals) foam monoliths wrapped with quartz wool around the perimeter surface were placed on top of the catalyst layer to allow the evaporation and mixing of n-hexadecane with steam, nitrogen and oxygen. The reaction temperature was measured by a thermocouple placed at the bottom of catalyst layer.

In a typical catalytic activity test, 2.5 g of catalyst was loaded into the reactor to form a 5mm layer. The flow rate of n-hexadecane was fixed at 0.817 mL/min. The flow rate of nitrogen gas was fixed at 1.9 SPLM. For the ATR process the carbon to water molar ratio (C/H_2O) was maintained at 1. The carbon to oxygen molar ratio (C/O) was adjusted between 0.8 and 1.2. For a C/O ratio equal to 1 the overall flow rate was 3.46 SLPM and the gas hourly space velocity (GHSV) was 512600 h^{-1}. After start-up the whole reaction system ran autothermally without an external heat source other than the preheater upstream of the catalyst.

The product gases were analyzed via an online GC (SRI 8610C). Product gases flowed through a sample loop. When taking a sample, the contents of the sample loop were injected through two parallel lines. One line was attached to an MTX-1 capillary column and an FID for the analysis of all hydrocarbons. The other line connects to a packed silicone column followed by a molecular sieve column and TCD for the analysis of gases including hydrogen, nitrogen, oxygen, carbon monoxide, and carbon dioxide.

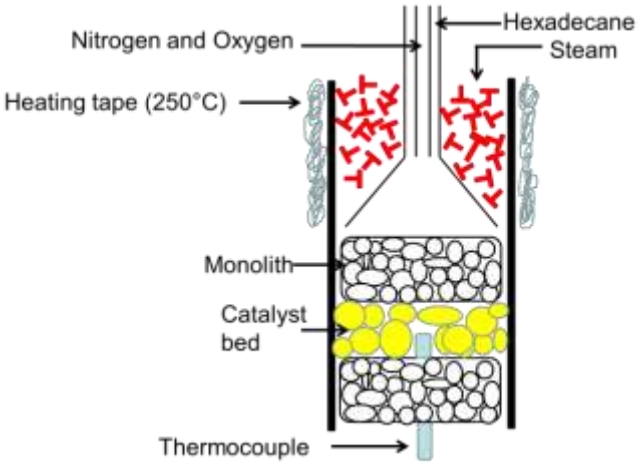

Figure 2.1 Schematic illustration of ATR and POX reaction setup.

The hexadecane used for activity tests were obtained from Alfa Aesar with the purity of 95%. Since the fuel is a complex mixture, calibration of GC responses for all possible reactants was not possible. Thus, molecules containing more than 6 carbon atoms were all assigned to hexadecane reactants arbitrarily. This may mean that conversion is under predicted if some of the hexadecane is cracked to molecules larger than C6. All the experiments were repeated three times and data with carbon error less than 20 % were collected. The carbon balance was generally within 10 % for reaction conditions where the C/O ratio is less than or equal to one. The hydrogen balance was also calculated, and was always less than 25 %, following the same

trend noted for the carbon balance, where the balance improved as the C/O ratio decreased and hexadecane conversion was high.

The conversion of hexadecane is calculated as follow:

$$Conversion = \frac{mol\ C(CO_2 + CO + hydrocarbon\ byproducts)}{mol\ C(CO_2 + CO + hydrocarbon\ byproducts) + mol\ C(hexadecane\ unreacted)} \times 100\% \quad (2.3)$$

The selectivity of product (I=CO_2, CO, or any hydrocarbon byproducts) is calculated as follows:

$$Selectivity\ of\ I = \frac{mol\ C(I)}{mol\ C(CO_2 + CO + hydrocarbon\ byproducts)} \times 100\% \quad (2.4)$$

The calculation of hydrogen yield and hydrogen selectivity of products (i=hydrogen, hydrocarbon byproducts) was done by the following equation:

$$Hydrogen\ yield = \frac{2 \times mol\ hydrogen}{34 * mol\ hexadecane\ feed\ in} \times 100\% \quad (2.5)$$

$$Hydrogen\ selectivity\ of\ i = \frac{mol\ hydrogen\ atom\ (i)}{2 \times mol\ hydrogen\ + mol\ hydrogen\ atom\ of\ all\ hydrocarbon\ byproducts} \times 100\% \quad (2.6)$$

$$Hydrogen\ selectivity\ of\ steam\ in\ ATR\ porcess = 1 - \sum hydrogen\ selectivity\ of\ all\ i\ products\ except\ steam \quad (2.7)$$

To analyze and compare the catalytic activity of pure Ni and bimetallic catalysts loaded on ceria based supports, hexadecane ATR and POX were run with carbon oxygen (C/O) molar ratios between 0.8 and 1.2. In the case of the ATR process, the C/steam ratio was fixed at 1.

2.2.4 Catalyst characterization

Temperature-programmed reduction (TPR) studies were conducted with an Altamira AMI-200 system. 0.05 g samples were loaded in a quartz U-tube reactor and treated at 550 ^{o}C for 1 h in pure argon. After cooling, the temperature was ramped from 25 ^{o}C to 900 ^{o}C at a constant rate of 5 ^{o}C/min in a flow of 10% H_2 in argon. H_2 consumption was recorded by a thermal conductivity detector (TCD). X-ray photoelectron spectroscopy (XPS) data were recorded using a PerkinElmer PHI 5400 electron spectrometer with an achromatic Al Kα X-ray source (1486.6 eV) operating at 300 W(15KV and 20mA). TEM studies were conducted on a Philips CM-10 transmission electron microscopy with an accelerating voltage of 100 kV. BET surface area of catalysts was measured via TriStar 3000 Surface Area and Porosity Analyzer. EDS measurement was carried out on EDX-700 Energy Dispersion X-ray Diffractometer. X-ray diffraction (XRD) was performed on a Bruker D8-Advance diffractometer with Cu KR radiation (40 kV, 40 mA) at 1.54 Å.

2.3 Results

2.3.1 Structural characterization

Pure Ni nanoparticles, bimetallic nanoparticles with 3/97 Pt/Ni molar ratio, and bimetallic nanoparticles with 10/90 Pt/Ni molar ratio were synthesized and loaded onto CeO_2, CeO_2-ZrO_2 and Gd_2O_3-CeO_2 supports. The size distributions of Ni and Pt/Ni bimetallic nanoparticles were investigated by TEM. By adjusting the reaction parameters such as metal salt concentration and CTAB/metal salt molar ratio, the size of nanoparticles could be adjusted. As shown by Figure 2.2, the size distribution of nanoparticles was controlled at 56±30 nm for pure Ni nanoparticles, 65± 19 nm for Pt/Ni 3/97 bimetallic nanoparticles, and 89±32 nm for Pt/Ni 10/90 bimetallic particles. The actual Pt/Ni molar ratio of bimetallic particles loaded on the

supports was measured by EDS. Table 2.1 lists the BET surface areas and Pt/Ni molar ratio of the freshly prepared catalysts. The BET surface areas of metal nanoparticles loaded on CeO_2 and CeO_2-ZrO_2 ranged from 80-120 m^2/g while the surface areas of metal nanoparticles loaded on Gd_2O_3-CeO_2 were between 11 m^2/g and 44 m^2/g.

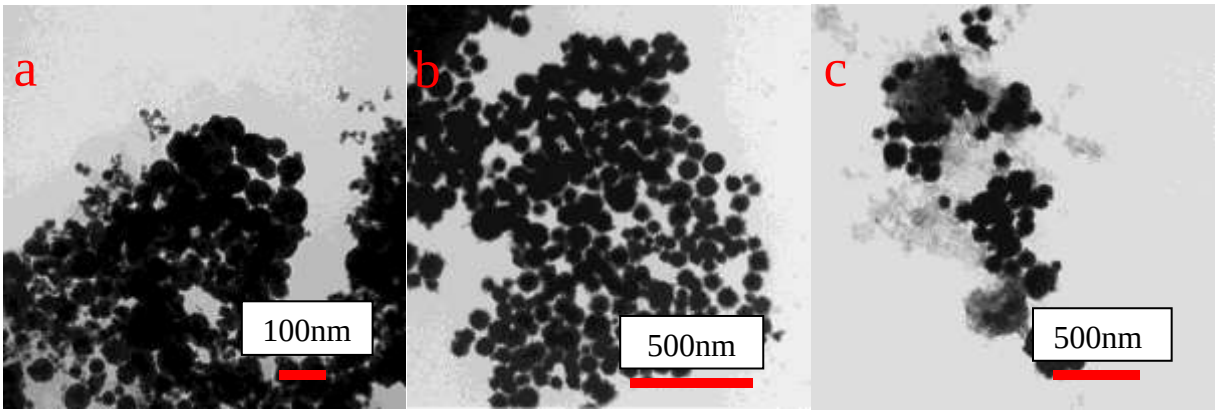

Figure 2.2 TEM image of (a) pure Ni nanoparticles, (b) 3/97 molar ratio Pt/Ni bimetallic nanoparticles, (c) 10/90 molar ratio Pt/Ni bimetallic nanoparticles.

Table 2.1 catalysts for ATR and POX of n-hexadecane

Sample	*Nanoparticle (wt. %)*	*Specific Surface Area (m^2/g)*	*AVG Pore Size (Diameter, nm)*	*Pore Volume (cm^3/g)*	*TEM (nm)*	*EDS Pt/Ni (mol/mol)*
		Nanoparticle+ Substrate			*Nanoparticle*	*Nanoparticle*
Ni-CeO_2-ZrO_2	5	88	4.1	0.102	56±30	-
Ni-CeO_2	5	123	8.5	0.270	56±30	-
Ni-Gd_2O_3-CeO_2	5	11	37.4	0.097	56±30	-
3/97 Pt/Ni-CeO_2-ZrO_2	5	108	4.2	0.13	65±19	2.23/97.77
3/97 Pt/Ni-CeO_2	5	74	6.6	0.13	65±19	2.23/97.77
3/97 Pt/Ni-Gd_2O_3-CeO_2	5	48	8.4	0.11	65±19	2.23/97.77
10/90 Pt/Ni-CeO_2-ZrO_2	5	35	8.0	0.07	89±32	8.09/91.91
10/90 Pt/Ni CeO_2	5	83	6.5	0.13	89±32	8.09/91.91
10/90 Pt/Ni-Gd_2O_3-CeO_2	5	44	9.6	0.11	89±32	8.09/91.91

2.3.2 TPR

Hydrogen TPR is applied to investigate the reducibility of catalysts and supports. In TPR, hydrogen is flowed over a catalyst as temperature is progressively raised. When a temperature is reached where the catalyst can react with hydrogen, a peak appears in the thermal conductivity detector due to the formation of water. The size and location of the reduction peak is used to infer information about the reducibility of the catalyst. For example, peaks appearing at lower temperatures indicate a more reducible catalyst.

TPR profiles of all fresh catalysts are shown in Figure 2.3. As shown in Figure 2.3a, two reduction peaks are evident at 290 and 343 °C for Ni supported on CeO_2. These peaks can be attributed to the reduction of well-dispersed and bulk phase nickel oxide species, respectively.[38, 48, 49] Similar NiO_x reduction peaks were also observed for Ni on Gd_2O_3-CeO_2. However, in the case of Ni on CeO_2-ZrO_2 catalysts there is a reduction peak for NiO_x ranging from 290 °C to 620°C, suggesting that NiO_x strongly interacted with the CeO_2-ZrO_2 support.[38] Reduction peaks around 800 °C for CeO_2 and Gd_2O_3-CeO_2 are induced by the reduction of bulk ceria from CeO_2 to Ce_2O_3. [45] The reduction peaks of surface ceria may overlap with Ni reduction peaks and cannot be observed.[50]

Figure 2.3b shows the TPR profiles of ceria-based catalysts containing Pt. The low temperature peaks near 130 °C are due to the reduction of PtO_x.[27, 45] The surface reduction peak of the CeO_2 support catalyzed by Pt is centered at 380°C with a shoulder at 460 °C.[45] In the case of Gd_2O_3-CeO_2 supports, the main peak is centered at 330°C with a shoulder at 420°C and is assigned to the reduction of surface ceria catalyzed by Pt.[45, 50] Moreover, the absence of the reduction peak of PtO_x at 130°C for Pt on Gd_2O_3-CeO_2 supports may suggest a stronger Pt-support interaction.[45]

The shift of the reduction peak to a lower temperature with the doping of Gd^{3+} into the ceria support is induced by the increase of oxygen mobility.[45] For the CeO_2-ZrO_2 support the surface reduction of ceria leads to two separate peaks centered at 300 °C and 450 °C, respectively. It is reported that the peak at the lower temperature may be ascribed to the reduction of surface CeO_2 close to Pt clusters, while the peak at the higher temperature may be induced by the reduction of surface CeO_2 not close to Pt clusters.[51] Also, the interaction between ceria and ZrO_2 enhanced the reducibility of surface ceria.[38, 52]

With the addition of trace amounts of Pt (3%) into Ni nanocatalysts (Figure 2.3 c), the peaks for Ni reduction shift to lower temperatures on Gd_2O_3-CeO_2 and CeO_2 supports because Pt catalyzes reduction of less reducible NiO_x.[31, 53, 54] The shoulder of reduction peaks at 472°C for the CeO_2 support and at 489°C for Gd_2O_3-CeO_2 support may be induced by the reduction of surface ceria. Still, the broad reduction peak for NiO_x on CeO_2-ZrO_2 centered at 418°C suggests strong interaction between NiO_x and the CeO_2-ZrO_2 support. Note that the interaction between Ni and ceria-based catalysts is due to the formation of an ideal solution between NiO_x and CeO_2 or ZrO_2, and the increasing Pt concentration in the bimetallic catalyst may increase the reducibility of the Ni phase.[38, 52] The shift of the reduction peak of NiO_x on CeO_2-ZrO_2 to a lower temperature also indicates the enhancement of reducibility of NiO_x-CeO_2-ZrO_2 by adding trace amounts of Pt.

The TPR profiles of bimetallic nanoparticles on ceria supports for catalysts where the molar percentage of Pt reaches 10% are presented in Figure 2.3d. For CeO_2 support and CeO_2-ZrO_2, the small peaks at 130°C could be assigned to the reduction of PtO_x as mentioned before. For 10/90 bimetallic nanoparticles on CeO_2, the reduction peak at 240°C is due to the reduction of NiO_x while the peak centered at 346 °C is assigned to the reduction of surface ceria. In the case of 10/90 bimetallic catalysts on Gd_2O_3-CeO_2 there is a broad peak from 212 °C to 610 °C. Due to the asymmetric feature of this peak, it may be due to overlapping peaks for the reduction of NiO_x and surface ceria. There are three different reduction peaks centered at 268 °C, 408 °C and 737 °C for Pt/Ni 10/90 bimetallic catalysts on the CeO_2-ZrO_2 support. The peak at 268 °C can be ascribed to the Pt catalyzed reduction of surface ceria. The peak at 408 °C may be considered as the overlapped peak for the reduction of NiO_x as well as the second reduction peak for the surface ceria. The final reduction peak at 737 °C is due to the reduction of bulk ceria. The

reduction peak for NiO_x of Pt/Ni 10/90 bimetallic catalysts on CeO_2-ZrO_2 is no longer as broad as that of Pure Ni and Pt/Ni 3/97 bimetallic catalysts on CeO_2-ZrO_2, suggesting that increasing Pt concentration further enhanced the reducibility of NiO_x-CeO_2-ZrO_2.

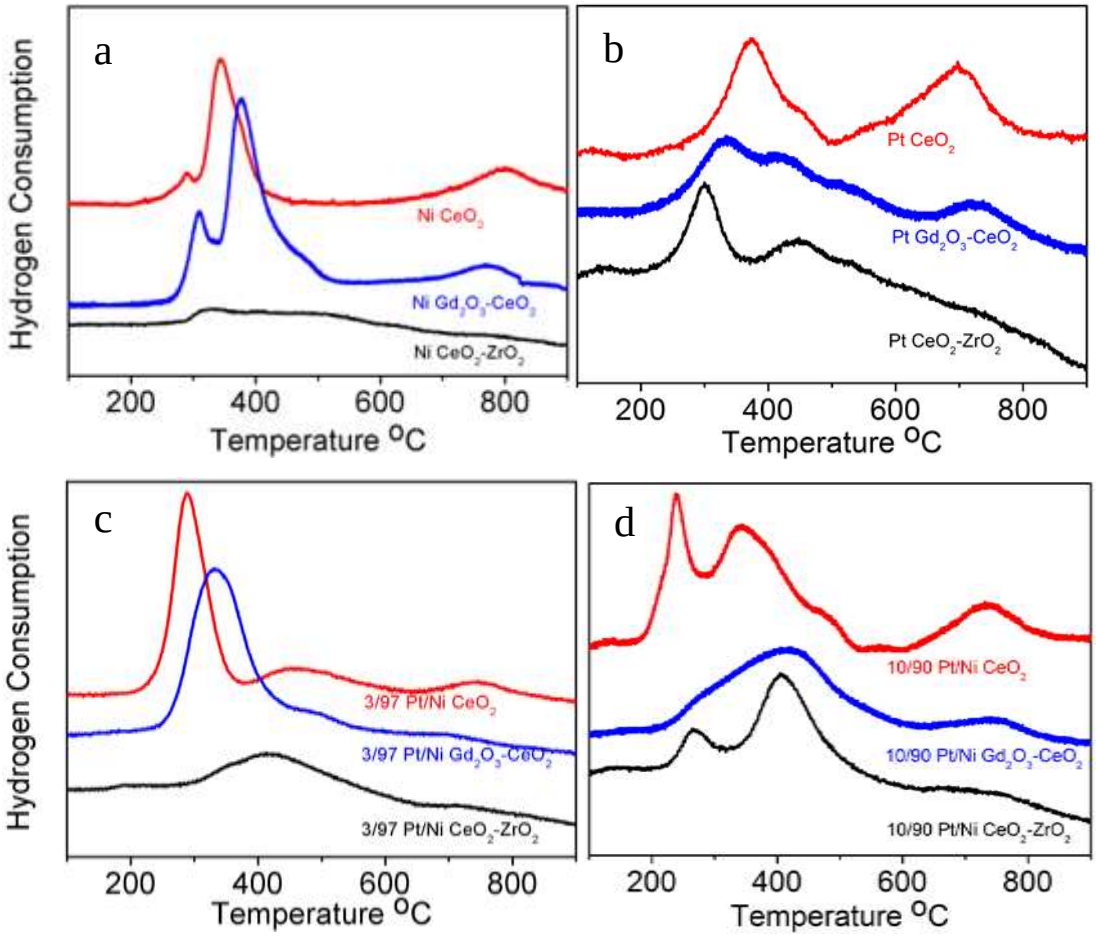

Figure 2.3 TPR profiles of (a) 5% (w/w) Ni catalysts on 3 different ceria based supports; (b) 5% (w/w) Pt catalysts on 3 different ceria based substrates; (c) 5% (w/w) 3/97 Pt/Ni catalysts on 3 different ceria based substrates; (d) 5% (w/w) 10/90 Pt/Ni catalysts on 3 different ceria based substrates.

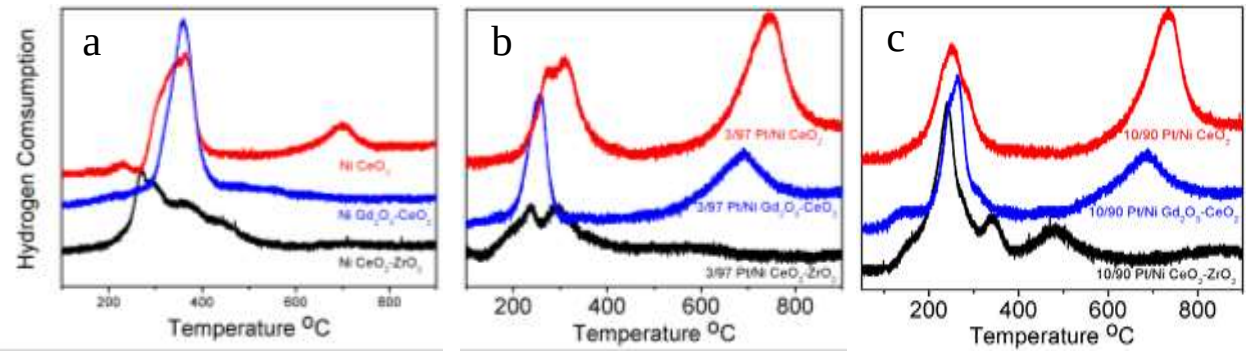

Figure 2.4 TPR profiles of used and regenerated catalysts:(a) 5% (w/w) Ni catalysts on 3 different ceria based supports; (b) 5% (w/w) 3/97 Pt/Ni catalysts on 3 different ceria based substrates; (c) 5% (w/w) 10/90 Pt/Ni catalysts on 3 different ceria based substrates.

The results in Figure 2.3 show the state of the catalyst prior to reaction. However, we wanted to understand the catalysts' properties after being run in ATR/POX, since the extreme conditions for these reactions may change the nature of the catalyst. Fig.2.4 shows the TPR profile of the same catalysts shown in Figure 2.3 after they had been used in reaction and subsequently calcined at 600 ^{o}C for 5 h to remove any carbon that may have been left on the surface from reaction. As shown in Figure 2.4 a, for Gd_2O_3-CeO_2 and CeO_2 supports, a peak at 360 ^{o}C is detected that can be ascribed to the reduction of both NiO_x and surface ceria. The overlapped reduction peaks of NiO_x and surface ceria of used catalysts did not change much compared to the NiO_x and surface ceria reduction peaks of fresh catalysts.

As Pt concentration increases (as shown in Figure 2.4 b and c), the single reduction peak that includes both NiO_x and surface ceria reduction moved to a lower temperature. This trend is similar to that of fresh catalysts. However, with the presence of Pt, the overlapped reduction peaks of NiO_x and surface ceria of used catalysts shifted to lower temperature compared to the NiO_x and surface ceria reduction peaks of fresh catalysts. The shift of reduction peak of surface ceria to lower temperature could also be observed for heat treated Pt loaded ceria based catalysts

(See Appendix A, Figure A2). These phenomena may be caused by enhanced interaction between Pt, NiO_x and surface ceria due to reaction at elevated temperatures.

In the case of used Ni CeO_2-ZrO_2 catalysts, there is a broad reduction peak from 210 ^oC to 580 ^oC as noted for the fresh catalysts, which demonstrates the strong interaction between NiO_x and CeO_2-ZrO_2. Comparing to the fresh Ni CeO_2-ZrO_2 catalysts, the broad reduction peak of used Ni CeO_2-ZrO_2 catalysts shifted to lower temperature, suggesting that changes during reaction lead to improved catalyst reducibility. With the addition of Pt, the broad reduction peak of NiO_x-CeO_2-ZrO_2 shifted to a lower temperature due to the enhancement of reducibility of NiO_x-CeO_2-ZrO_2.

2.3.3 XPS

10/90 Pt/Ni bimetallic catalysts on different ceria-based supports were characterized via XPS to investigate the interaction between NiO_x and the supports (Fig 2.5). The binding energy of Ni2p for fresh catalysts on all three different supports is around 855 eV accompanied with a satellite peak around 860 eV,[43] which is the binding energy of free NiO (Fig 2.5a).[42] Figure 2.5b shows the XPS spectra for used catalysts that have been calcined in air at 600^oC for five hours to remove surface carbon. On the regenerated catalyst Pt/Ni CeO_2-ZrO_2, the binding energy of Ni2p shifts to 858.2 eV, which indicates the strong interaction between NiO_x and CeO_2-ZrO_2 support (Fig 2.5b).[42] In contrast, the Ni2p peak position of NiO_x on Gd_2O_3-CeO_2 and CeO_2 supports is not changed. We can be sure that the shift in the binding energy in Pt/Ni CeO_2-ZrO_2 is due to changes during reaction, and not the calcination treatment, because calcination of the fresh catalysts does not change the peak position of Ni2p (See Appendix A, Figure A1). We may conclude that the solid solution of NiO_x-CeO_2-ZrO_2 is formed during the high temperature reaction process.

The formation of a NiO_x-CeO_2-ZrO_2 solid solution may also be indicated by the Pt/Ni atomic ratio before and after reaction as measured by XPS. As shown in Table 2.2, in the case of the fresh catalysts, the Pt/Ni atomic ratio ranges from 0.14-0.17, which is slightly higher than that obtained from EDS measurements (reported in Table 2.1). This may be due to the surface segregation of Pt atoms.[31, 55] The oxidation treatment at 600 ^oC for 5 h does not change the measured Pt/Ni atomic ratio appreciably (See Appendix A Figure A1). However, after reaction the Pt/Ni atomic ratio increased to 0.65 for bimetallic catalysts on CeO_2-ZrO_2 while there is no significant variation for bimetallic catalysts on other supports. The increasing of Pt/Ni atomic ratio for bimetallic catalysts on CeO_2-ZrO_2 may be induced by the migration of Ni into the CeO_2-ZrO_2 support and the formation of a NiO_x-CeO_2-ZrO_2 solid solution.

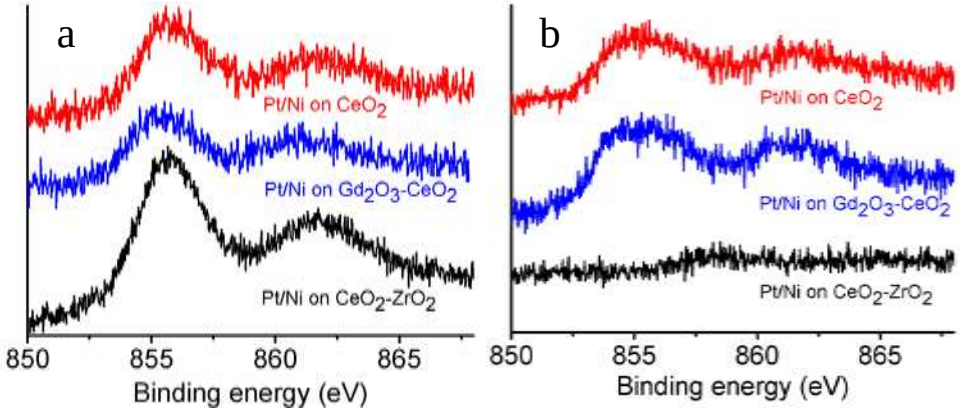

Figure 2.5 The Ni2p3/2 core spectra of 10/90 Pt/Ni on different ceria based support: (a) as prepared catalysts and (b) used and calcined catalysts.

Table 2.2 Pt/Ni molar ratio of 10/90 Pt/Ni bimetallic catalysts on different supports measured by XPS

Sample	Pt/Ni molar ratio (as prepared catalysts)	Pt/Ni molar ratio (catalysts calcined in air for 5h)	Pt/Ni molar ratio (used and calcined catalysts)
10/90 Pt/Ni Gd_2O_3-CeO_2	0.17	0.19	0.22
10/90 Pt/Ni CeO2	0.14	0.20	0.22
10/90 Pt/Ni CeO_2-ZrO_2	0.17	0.17	0.65

2.3.4 XRD

To further probe the state of the catalyst following reaction, XRD spectra were taken for used 10/90 Pt/Ni bimetallic catalysts on the three different supports. These spectra are shown in Figure 2.6. As showed in 2.6 a and b, diffraction peaks at 28.3^o, 33.0^o, 47.2^o, 56.2^o, 58.9^o, 69.2^o, 76.6^o and 78.9^o could be assigned to CeO_2, while diffraction peaks at 37.4^o, 43.5^o, 63.1^o and 75.5^o were owing to NiO.[12, 56] Due to the low loading of catalyst on the supports (~5%), the diffraction peaks of NiO are broad. However, in the case of Pt/Ni CeO_2-ZrO_2, the NiO diffraction peaks were not shown.[57] Although the diffraction peaks of NiO were not obvious in any of the spectra due to the low loading and high dispersity of NiO crystals, the lack of NiO diffraction peaks for Pt/Ni CeO_2-ZrO_2 may further indicate that Ni migrated into the CeO_2-ZrO_2 support to form a solid solution.

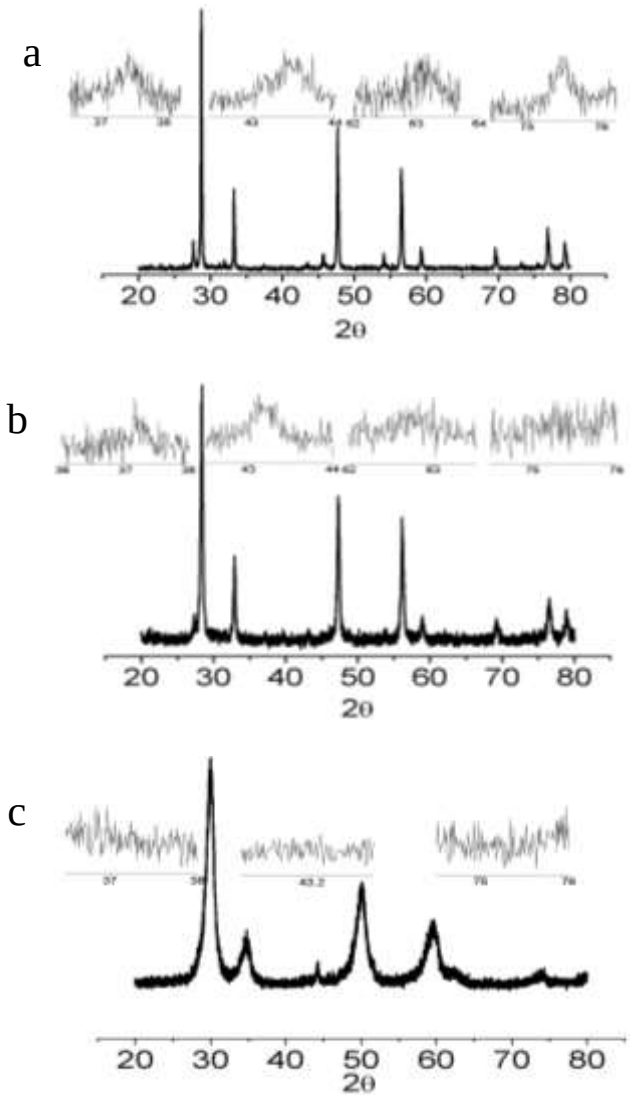

Figure 2.6 XRD pattern of used catalysts: (a) Pt/Ni bimetallic catalysts on CeO_2, (b) Pt/Ni bimetallic catalysts on Gd_2O_3-CeO_2, (c) Pt/Ni bimetallic catalysts on CeO_2-ZrO_2.

2.3.5 *n*-hexadecane ATR and POX with different C/O ratio

Figure 2.7a plots the conversion of *n*-hexadecane, as well as CO, CO_2 and overall hydrocarbon byproduct selectivity as functions of C/O ratio for the ATR process on 10/90 Pt/Ni Gd_2O_3-CeO_2 catalysts. The hydrocarbon byproducts include all C1 to C6 species. C2 to C6 are generated from the cracking reaction of hexadecane. Methane can be produced from steam and CO due to reaction equilibrium. Figure 2.7b shows the hydrogen selectivity of ATR process on

the same catalysts with respect to C/O ratio. The conversion for oxygen is almost 100 % for all C/O ratios. The hexadecane conversion and hydrogen selectivity is highest for the lowest C/O ratios. The water selectivity for all C/O ratios is negative, indicating the contribution of the SR reaction during the ATR process. The maximum conversion and hydrogen selectivity was obtained at C/O ratio equal to 0.8. As the C/O ratio increases, the hexadecane conversion and selectivity to syngas decreases dramatically, while the production of hydrocarbon byproducts increases. The hydrocarbon byproducts include methane as well as olefins from C_2 to C_6. Usually, when the C/O ratio was high, olefins dominated the hydrocarbon byproducts, while methane contributed to a large part of the hydrogen byproducts when the C/O ratio is low.

For the POX process, the trend for the hexadecane conversion, syngas selectivity and hydrocarbon byproduct selectivity are similar to that of ATR (Figure2.7 c and d). However, POX gives lower CO_2 selectivity and higher CO selectivity than ATR, likely because of an enhanced WGS reaction in ATR. Furthermore, for POX, the increase of CO_2 selectivity at high C/O ratios may be allocated to the failure of catalytic POX process when oxygen is deficient. Plots of other catalysts showed similar trends for ATR and POX (see Appendix A Figure A3 to Figure A10).

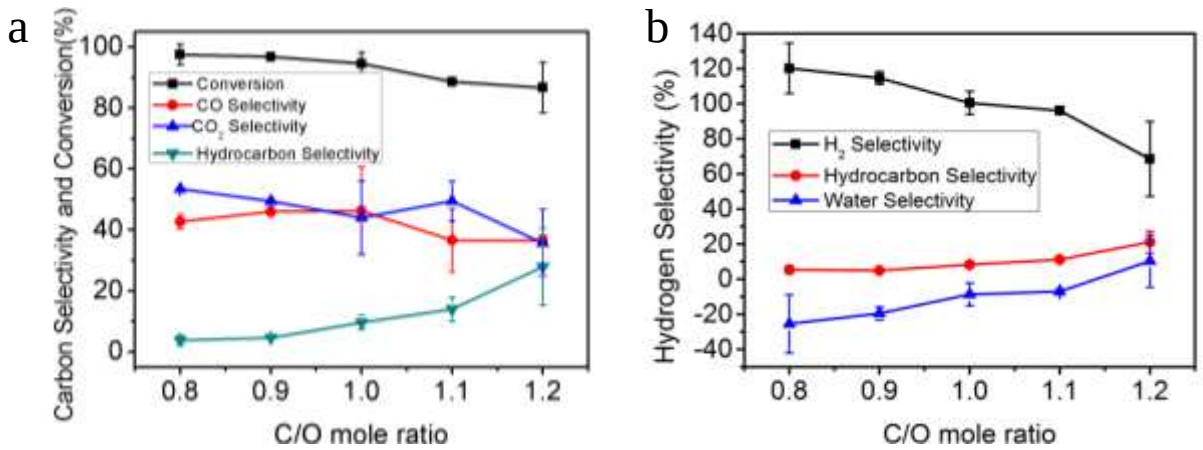

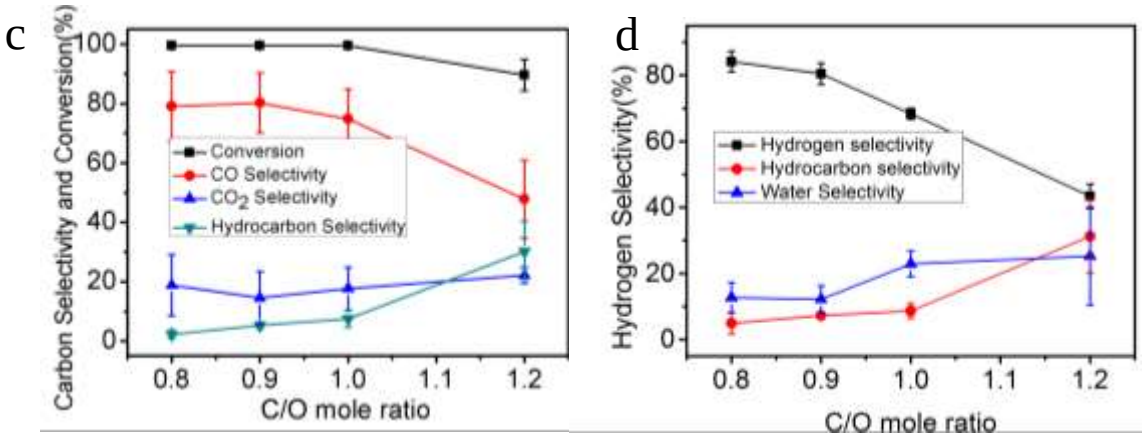

Figure 2.7 Impact of C/O molar ratio on the ATR and POX process of n-hexadecane (10/90 Pt/Ni-Gd_2O_3-CeO_2). (a) Carbon conversion and selectivity for ATR, (b) Hydrogen selectivity for ATR, (c) Carbon conversion and selectivity for POX, (d) Hydrogen selectivity for POX.

Reaction temperature is a function of the extent that endothermic and exothermic reactions occur in the catalyst bed. Figure A10 in the appendix A shows how the catalyst bed temperature changes with C/O ratio for all catalysts. In general, the bed temperature for ATR and POX process was ranging from 700 ^{o}C to 1000 ^{o}C and decreased with the increase of the C/O ratio for both ATR and POX process. The decrease of bed temperature indicated that less heat was generated via POX reaction due to the deficiency of oxygen. The trend of bed temperature corresponded well with the trend of carbon and hydrogen selectivity.

2.3.6 Comparison of catalyst performance for hydrogen generation

The performances of Ni and Pt/Ni bimetallic catalysts on ceria based support for *n*-hexadecane ATR and POX were investigated by comparing the hydrogen yield (Figure 2.8). In the case of ATR (Figure 2.8a), for all catalysts the hydrogen yield decreased with increasing C/O molar ratio. For each support, hydrogen yield generally increased as the amount of platinum in the bimetallic catalysts increased. In the case of the CeO_2-ZrO_2 support, the hydrogen yield was increased dramatically with the doping of a trace amount of platinum. For example, at a C/O

ratio of 0.8, the hydrogen yield went from 94% to 111% as the Pt/Ni molar ratio increased from 0 to 3%. However, when the Pt/Ni molar ratio further increased to 10/90, the hydrogen yield only reached 117%. For the Gd_2O_3-CeO_2 support no significant improvement in hydrogen yield was noted until the Pt/Ni ratio was 10/90. When CeO_2 was the support the hydrogen yield was generally less than that of the other two supports for all Pt/Ni molar ratios.

As shown in Figure 2.8b the trend of catalytic activity of POX with increasing platinum concentration is similar to that of ATR. In the case of CeO_2-ZrO_2 support enhancement of activity was observed when Pt/Ni molar ratio of bimetallic catalysts increased from 0 to 3/97. However, no significant enhancement of catalytic activity was observed when the Pt/Ni molar ratio increased to 10/90. For CeO_2 as the support, the hydrogen yield was generally independent of the amount of platinum added into the Ni nanocatalysts. When Gd_2O_3-CeO_2 was applied as support, the hydrogen yield for pure Ni and Pt/Ni bimetallic catalysts increased with the increasing concentration of platinum concentration.

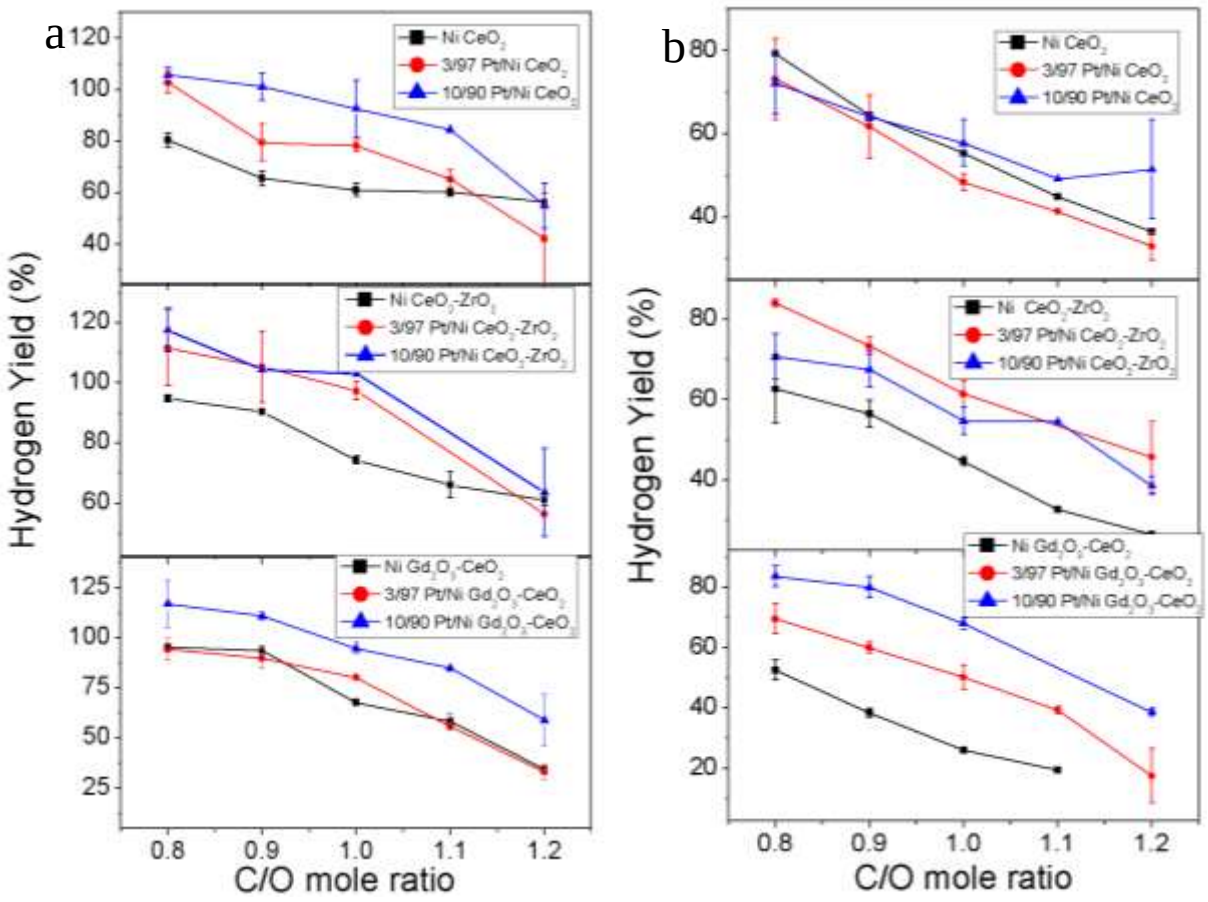

Figure 2.8 The hydrogen yield of ATR and POX process: (a) ATR(C/H_2O=1), (b) POX.

Smaller hydrocarbons were formed during ATR or POX process due to cracking reactions.[10] Figure 2.9 a and b show the selectivity of hydrocarbon products ranging from C1 to C6. It could be concluded that the production of olefin fragments were greatly suppressed for ATR (Figure 2.9a) compared to that of POX (Figure 2.9b) due to the SR reaction during ATR process. For all the catalysts, increasing the C/O molar ratio enhanced the generation of hydrocarbon byproduct selectivity for both ATR and POX.

The elimination of hydrocarbon byproducts of ATR and POX is crucial to achieve a high yield of hydrogen. The suppression of hydrocarbon byproducts with the increasing of Pt concentration for catalysts on all three supports further demonstrated that the ATR/POX of

heavy hydrocarbons to hydrogen can be enhanced via the addition of Pt. The hydrocarbon byproduct selectivity is lower when CeO_2-ZrO_2 is used as the support than for the other two supports for either pure Ni nanoparticles or Pt/Ni bimetallic particles. For example, for ATR at a C/O ratio of 1.2 the hydrocarbon byproduct selectivity equals 15 for 3/97 Pt/Ni CeO_2-ZrO_2, while the hydrocarbon selectivities are 27.9 and 29.2 for 3/97 Pt/Ni CeO_2 and 3/97 Pt/Ni Gd_2O_3-CeO_2, respectively.

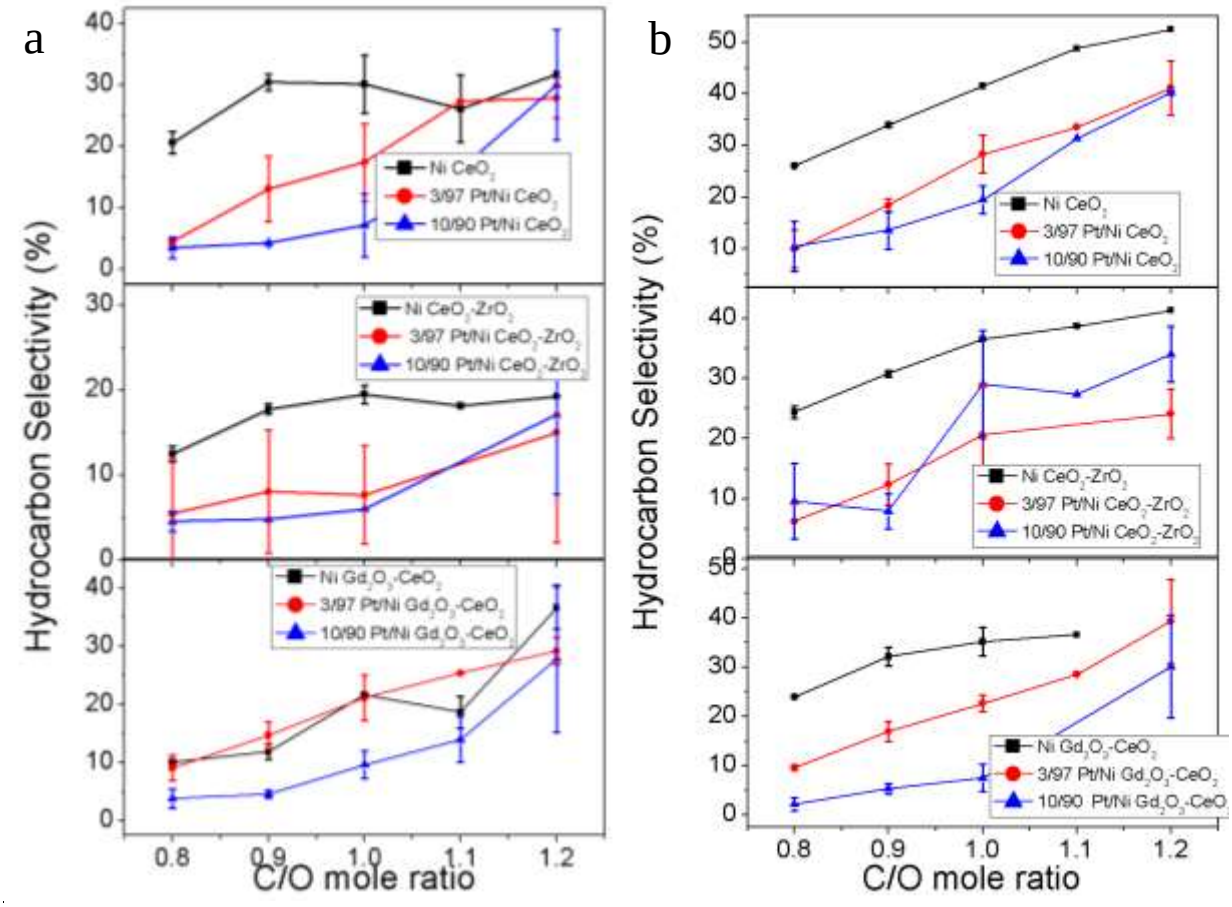

Figure 2.9 The hydrocarbon byproducts selectivity of ATR and POX process: (a) ATR(C/H_2O=1), (b) POX.

2.4 Discussion

It was reported that Ni on CeO_2-ZrO_2 shows high activity for SR, POX and ATR reaction of methane and ethanol.[38-42, 52] An explanation for the high activity of Ni-CeO_2-ZrO_2 was also proposed: over Ni-CeO_2-ZrO_2 cerium oxide is much easier to reduce due to the spillover effect of Ni. Furthermore, the high reducibility of cerium oxide will promote the oxygen mobility during a redox cycle. The enhanced oxygen storage, transport and release properties of Ni-CeO_2-ZrO_2 played a key role in the high catalytic performance of Ni-CeO_2-ZrO_2 catalysts.[38, 42, 52]

For the Pt/Ni bimetallic catalysts on CeO_2-ZrO_2 reported in this paper, Ni formed a Ni-CeO_2-ZrO_2 solid solution with the support, as shown by the XPS and TPR data. The formation of Ni-CeO_2-ZrO_2 solid solution further led to the surface enrichment of Pt (Table 2.2). Surface Pt/Ni molar ratios as high as 0.33 were achieved even for 3/97 Pt/Ni-CeO_2-ZrO_2 catalyst (Data not shown). As shown in the TPR profile (Figure 2.3c, d and Figure 2.4b, c) Pt enriched on the surface of the catalyst catalyzed the reduction of Ni-CeO_2-ZrO_2 solid solution due to the hydrogen spillover effect. Consequently, the reduction temperature of Ni-CeO_2-ZrO_2 shifted to a lower value, indicating higher reducibility of Ni-CeO_2-ZrO_2 as well as better oxygen storage, transport and release properties.[58]

The weight percentage of bimetallic catalysts loaded on ceria based supports in our work (5 %) was much less than that reported in previous works (more than 10 %). In contrast with the Ni-CeO_2-ZrO_2 catalysts reported in those papers, we conclude that the majority of Ni in our catalysts was incorporated into CeO_2-ZrO_2 to form a solid solution while a small amount of Ni may have existed as metallic Ni or free NiO during reaction.

As shown in Figure 2.10, a possible reaction mechanism for ATR or POX on Pt/Ni CeO_2-ZrO_2 can be proposed: hydrocarbons adsorbed on the surface of Pt or Ni metallic cluster

dissociate to carbon species and hydrogen, and these carbon species can be oxidized to CO or CO_2 on metallic Pt or Ni by active oxygen. Alternatively, the adsorbed carbon species may be oxidized at the boundary of metallic cluster and Ni-Ce-Zr-O_x by the support. Oxygen or steam will further react with the Ni-Ce-ZrO_x and reoxidize the support. Although it has been reported that doping Ni with small quantities of noble metals will only increase the metal surface area instead of electronically modifying the Ni sites,[24] slightly doping Ni-CeO_2-ZrO_2 with Pt in our experiments greatly enhanced its reducibility and catalytic performance. Catalyst design based on this phenomenon may open an opportunity for the preparation of cheap and high performance catalysts.

The electronic interaction of bimetallic catalysts loaded on ceria based support is complex because it involves several interaction pairs including Pt-Ni interactions, Pt-support interactions and Ni-support interactions. In the case of cerium oxide support, TPR and XPS data show that both the Ni support interaction and Pt support interaction is low compared to CeO_2-ZrO_2 and Gd_2O_3-CeO_2 supports. Consequently, Pt/Ni CeO_2 catalysts do not show high activity for both the ATR and POX reaction of hexadecane.

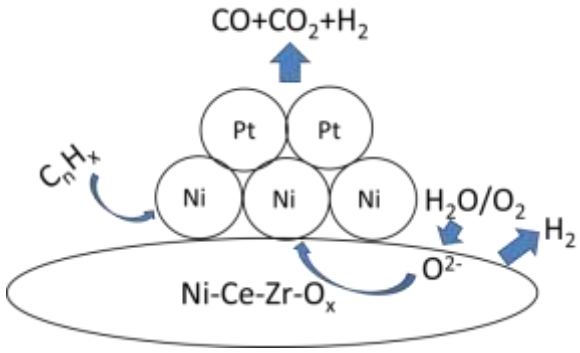

Figure 2.10 Schematic illustration of hexadecane ATR or POX mechanism via Pt/Ni-CeO_2-ZrO_2.

Doping of CeO_2 with Gd_2O_3 will generate oxygen vacancies as well as enhance the electronic interaction between Pt and ceria support.[45] For Pt/Ni Gd_2O_3-CeO_2 catalysts the

increase in Pt concentration in the bimetallic catalysts enhanced both the interaction between catalysts and supports as well as the reducibility of catalysts. Thus, the catalytic activity for ATR or POX of hexadecane will be improved with increasing Pt concentration in bimetallic catalysts. In our case, the Pt loading of Pt/Ni 10/90 Gd_2O_3-CeO_2 reaches 1.3 % (w/w). Recently Kang, *et al*. studied the autothermal reforming of higher hydrocarbons on Pt-Gd_2O_3-CeO_2 at similar conditions to our studies. [46] Their results, obtained with roughly three times less metal loading than that used in our catalysts and with space velocities four times less than our, indicated a similar hydrogen yield (~120 % with $H_2O/C = 1.25$, $O_2/C = 0.5$) to our results. These results suggest that using Pt/Ni bimetallic catalysts did not enhance activity for ATR over pure Pt, but also show that it might be possible to replace some expensive Pt with inexpensive Ni without sacrificing hydrogen yield.

By comparing the results for Pt/Ni bimetallic catalysts loaded on the three different ceria based supports, it can be seen that Pt/Ni-CeO_2-ZrO_2 showed the highest activity for ATR of high hydrocarbons with the low concentration of Pt. On the other hand, Pt/Ni bimetallic catalysts loaded on CeO_2 exhibited low activity while Pt/Ni bimetallic catalysts on Gd_2O_3-CeO_2 showed similar activity with same concentration of Pt on Gd_2O_3-CeO_2.

2.5 Conclusions

The catalytic activity of ATR and POX reaction via Pt/Ni bimetallic catalysts on three different ceria based catalysts has been studied. High catalytic activity could be achieved for Pt/Ni-CeO_2-ZrO_2 even if only a small amount of Pt was added. The high performance of Pt/Ni-CeO_2-ZrO_2 catalysts could be ascribed to the strong interaction between Ni and CeO_2-ZrO_2 support, as well as the enhancement of reducibility due to the addition of Pt. Doping the Ni-CeO_2-ZrO_2 catalyst with small quantities of noble metal will further enhance the catalytic

activity and open an opportunity for the design of cheap and high performance catalysts for ATR and POX reactions.

For ATR and POX the promotion effect of CeO_2 in Pt/Ni CeO_2 catalysts is limited because both Pt and Ni do not show a strong interaction with CeO_2. In the case of the Gd_2O_3-CeO_2 catalyst, no significant improvement of catalytic activity was achieved until Pt quantities reached a high value (1% w/w).

References

1. Ghenciu, A. Review of fuel processing catalysts for hydrogen production in PEM fuel cell systems. *Curr. Opin. Solid State Mat. Sci.* **6**, 389-399 (2002).

2. Boettner, D. D. & Moran, M. J. Proton exchange membrane (PEM) fuel cell-powered vehicle performance using direct-hydrogen fueling and on-board methanol reforming. *Energy* **29**, 2317-2330 (2004).

3. Han, J., Kim, I. & Choi, K. High purity hydrogen generator for on-site hydrogen production. *Int. J. Hydrogen Energy* **27**, 1043-1047 (2002).

4. Mitchell, M., Kim, D. & Kenis, P. Ceramic microreactors for on-site hydrogen production. *J.Catal.* **241**, 235-242 (2006).

5. Xu, X., Li, P. & Shen, Y. Small-scale reforming of diesel and jet fuels to make hydrogen and syngas for fuel cells: A review. *Appl. Energy* **108**, 202-217 (2013).

6. Ersoz, A. *et al*. Autothermal reforming as a hydrocarbon fuel processing option for PEM fuel cell. *J. Power Sources* **118**, 384-392 (2003).

7. Navarro, R., Pena, M. & Fierro, J. Hydrogen production reactions from carbon feedstocks: fossil fuels and biomass. *Chem. Rev.* **107**, 3952-3991 (2007).

8. Lenz, B. & Aicher, T. Catalytic autothermal reforming of Jet fuel. *J. Power Sources* **149**, 44-52 (2005).

9. Kang, I. & Bae, J. Autothermal reforming study of diesel for fuel cell application. *J. Power Sources* **159**, 1283-1290 (2006).

10. Dreyer, B., Lee, I., Krummenacher, J. & Schmidt, L. Autothermal steam reforming of higher hydrocarbons: n-Decane, n-hexadecane, and JP-8. *Appl. Catal. A***307**, 184-194 (2006).

11. Qi, A., Wang, S., Ni, C. & Wu, D. Autothermal reforming of gasoline on Rh-based monolithic catalysts. *Int. J. Hydrogen Energy* **32**, 981-991 (2007).

12. Navarro, R., Alvarez-Galvan, M., Rosa, F. & Fierro, J. Hydrogen production by oxidative reforming of hexadecane over Ni and Pt catalysts supported on Ce/La-doped Al_2O_3. *Appl. Catal. A* **297**, 60-72 (2006).

13. Kaila, R. & Krause, A. Autothermal reforming of simulated gasoline and diesel fuels. *Int J Hydrogen Energy* **31**, 1934-1941 (2006).

14. Ayabe, S. *et al*. Catalytic autothermal reforming of methane and propane over supported metal catalysts. *Appl. Catal. A* **241**, 261-269 (2003).

15. Dias, J. A. C. & Assaf, J. M. Autothermal reforming of methane over Ni/γ-Al_2O_3 promoted with Pd: The effect of the Pd source in activity, temperature profile of reactor and in ignition. *Appl. Catal. A* **334**, 243-250 (2008).
16. Yoon, S., Kang, I. & Bae, J. Suppression of ethylene-induced carbon deposition in diesel autothermal reforming. *Int. J. Hydrogen Energy* **34**, 1844-1851 (2009).
17. Chen, X., Tadd, A. R. & Schwank, J. W. Carbon deposited on Ni/CeZrO isooctane autothermal reforming catalysts. *J. Catal.* **251**, 374-387 (2007).
18. Chen, X., Gould, B. D. & Schwank, J. W. n-Dodecane reforming over monolith-based Ni catalysts: SEM study of axial carbon distribution profile. *Appl. Catal. A* **356**, 137-147 (2009).
19. Gould, B. D., Chen, X. & Schwank, J. W. n-Dodecane reforming over nickel-based monolith catalysts: Deactivation and carbon deposition. *Appl. Catal. A* **334**, 277-290 (2008).
20. Silvester, L. *et al*. NiO supported on Al_2O_3 and ZrO_2 oxygen carriers for chemical looping steam methane reforming. *Int. J. Hydrogen Energy* **40**, 7490-7501(2015).
21. Moon, D. J., Ryu, J. W., Lee, S. D., Lee, B. G. & Ahn, B. S. Ni-based catalyst for partial oxidation reforming of iso-octane. *Appl. Catal. A* **272**, 53-60 (2004).
22. Cheekatamarla, P. K. & Lane, A. M. Catalytic autothermal reforming of diesel fuel for hydrogen generation in fuel cells: I. Activity tests and sulfur poisoning. *J. Power Sources* **152**, 256-263 (2005).
23. Strohm, J. J., Zheng, J. & Song, C. Low-temperature steam reforming of jet fuel in the absence and presence of sulfur over Rh and Rh–Ni catalysts for fuel cells. *J. Catal.* **238**, 309-320 (2006).
24. Dias, J. A. C. & Assaf, J. M. Autothermal reforming of methane over Ni/γ-Al_2O_3 catalysts: the enhancement effect of small quantities of noble metals. *J. Power Sources* **130**, 106-110 (2004).
25. Xu, X., Zhang, S. & Li, P. Autothermal reforming of n-dodecane and desulfurized Jet-A fuel for producing hydrogen-rich syngas. *Int. J. Hydrogen Energy* **39**, 19593-19602 (2014).
26. Mondal, T., Pant, K. K. & Dalai, A. K. Catalytic oxidative steam reforming of bio-ethanol for hydrogen production over Rh promoted Ni/CeO_2–ZrO_2 catalyst. *Int. J. Hydrogen Energy* **40**,2529-2544(2015).
27. Cheekatamarla, P. K. & Lane, A. M. Efficient bimetallic catalysts for hydrogen generation from diesel fuel. *Int. J. Hydrogen Energy* **30**, 1277-1285 (2005).
28. Mukainakano, Y. *et al*. Catalytic performance and characterization of Pt–Ni bimetallic catalysts for oxidative steam reforming of methane. *Chem. Eng. Sci.* **63**, 4891-4901 (2008).
29. Çağlayan, B. S., Önsan, Z. İ. & Aksoylu, A. E. Production of hydrogen over bimetallic Pt–Ni/δ-Al_2O_3: II. Indirect partial oxidation of LPG. *Catal. Lett.* **102**, 63-67 (2005).

30. Çağlayan, B. S., Avcı, A. K., Önsan, Z. İ. & Aksoylu, A. E. Production of hydrogen over bimetallic Pt–Ni/δ-Al_2O_3: I. Indirect partial oxidation of propane. *Appl. Catal. A* **280**, 181-188 (2005).
31. Li, B. *et al*. Temperature profile of catalyst bed during oxidative steam reforming of methane over Pt-Ni bimetallic catalysts. *Appl. Catal. A* **304**, 62-71 (2006).
32. Li, B. *et al*. Surface modification of Ni catalysts with trace Pt for oxidative steam reforming of methane. *J. Catal.* **245**, 144-155 (2007).
33. Liu, L. & Hong, L. Nickel phosphide catalyst for autothermal reforming of surrogate gasoline fuel. *AIChE J.* **57**, 3143-3152 (2011).
34. Alvarez-Galvan, M. *et al*. Hydrogen production for fuel cell by oxidative reforming of diesel surrogate: Influence of ceria and/or lanthana over the activity of Pt/Al_2O_3 catalysts. *Fuel* **87**, 2502-2511 (2008).
35. Wang, Z., Huang, H., Liu, H. & Zhou, X. Self-sustained electrochemical promotion catalysts for partial oxidation reforming of heavy hydrocarbons. *Int. J. Hydrogen Energy* **37**,17928-17935(2012).
36. Mustu, H. *et al*. Effect of synthesis route of mesoporous zirconia based Ni catalysts on coke minimization in conversion of biogas to synthesis gas. *Int. J. Hydrogen Energy* **40**, 3217-3228 (2015).
37. da Silva, A. M. *et al*. Study of the performance of Rh/La_2O_3–SiO_2 and Rh/CeO_2 catalysts for SR of ethanol in a conventional fixed-bed reactor and a membrane reactor. *Int. J. Hydrogen Energy* **40**, 4154-4166 (2015).
38. Roh, H., Jun, K., Dong, W., Park, S. & Baek, Y. Highly stable Ni catalyst supported on Ce–ZrO_2 for oxy-steam reforming of methane. *Catal. Lett.* **74**, 31-36 (2001).
39. Takeguchi, T., Furukawa, S., Inoue, M. & Eguchi, K. Autothermal reforming of methane over Ni catalysts supported over CaO–CeO_2–ZrO_2 solid solution. *Appl. Catal. A* **240**, 223-233 (2003).
40. Gould, B. D., Tadd, A. R. & Schwank, J. W. Nickel-catalyzed autothermal reforming of jet fuel surrogates: n-Dodecane, tetralin, and their mixture. *J. Power Sources* **164**, 344-350 (2007).
41. Gould, B. D., Chen, X. & Schwank, J. W. Dodecane reforming over nickel-based monolith catalysts. *J. Catal.* **250**, 209-221 (2007).
42. Roh, H., Koo, K. Y. & WANG, L. Y. Combined reforming of methane over co-precipitated Ni—CeO_2, Ni—ZrO_2 and Ni—$Ce_{0.8}Zr_{0.2}O_2$ catalysts to produce synthesis gas for gas to liquid (GTL) process. *Catal. Today.* **146**, 71-75 (2009).
43. Ismagilov, I. *et al*. Hydrogen production by autothermal reforming of methane over NiPd catalysts: Effect of support composition and preparation mode. *Int. J. Hydrogen Energy* **39**, 20992-21006 (2014).

44. Kang, I. *et al*. The micro-reactor testing of catalysts and fuel delivery apparatuses for diesel autothermal reforming. *Catal. Today.* **136**, 249-257 (2008).

45. Xue, Q., Gao, L. & Lu, Y. Sulfur-tolerant $Pt/Gd_2O_3—CeO_2—Al_2O_3$ catalyst for high efficiency H_2 production from autothermal reforming of retail gasoline. *Catal. Today.* **146**, 103-109 (2009).

46. Kang, I., Bae, J. & Bae, G. Performance comparison of autothermal reforming for liquid hydrocarbons, gasoline and diesel for fuel cell applications. *J. Power Sources* **163**, 538-546 (2006).

47. Wu, S. & Chen, D. Synthesis and stabilization of Ni nanoparticles in a pure aqueous CTAB solution. *Chem. Lett.* **33**, 406-407 (2004).

48. Kugai, J., Subramani, V., Song, C., Engelhard, M. H. & Chin, Y. Effects of nanocrystalline CeO_2 supports on the properties and performance of Ni–Rh bimetallic catalyst for oxidative steam reforming of ethanol. *J. Catal.* **238**, 430-440 (2006).

49. Kugai, J., Velu, S. & Song, C. Low-temperature reforming of ethanol over CeO_2-supported Ni-Rh bimetallic catalysts for hydrogen production. *Catal. Lett.* **101**, 255-264 (2005).

50. Lu, Y., Chen, J., Liu, Y., Xue, Q. & He, M. Highly sulfur-tolerant $Pt/Ce_{0.8}Gd_{0.2}O_{1.9}$ catalyst for steam reforming of liquid hydrocarbons in fuel cell applications. *J. Catal.* **254**, 39-48 (2008).

51. Reddy, B. M., Rao, K. N. & Reddy, G. K. Controlled Hydrogenation of Acetophenone Over $Pt/CeO_2–MO_x$ (M= Si, Ti, Al, and Zr) Catalysts. *Catal. Lett.* **131**, 328-336 (2009).

52. Dong, W., Jun, K., Roh, H., Liu, Z. & Park, S. Comparative study on partial oxidation of methane over Ni/ZrO_2, Ni/CeO_2 and $Ni/Ce–ZrO_2$ catalysts. *Catal. Lett.* **78**, 215-222 (2002).

53. Rynkowski, J., Rajski, D., Szyszka, I. & Grzechowiak, J. R. Effect of platinum on the hydrogenation activity of nickel catalysts. *Catal. Today.* **90**, 159-166 (2004).

54. Rynkowski, J., Paryjczak, T., Lenik, M., Farbotko, M. & Goralski, J. Temperature-programmed reduction of alumina-supported Ni–Pt systems. *J. Chem. Soc. Faraday Trans.* **91**, 3481-3484 (1995).

55. Wang, G., Van Hove, M., Ross, P. & Baskes, M. Monte Carlo simulations of segregation in Pt-Ni catalyst nanoparticles. *J. Chem. Phys.* **122**, 024706 (2005).

56. Ghelich, R., Rad, M. K., Yuzbashi, A. A. & Khakpour, Z. Preparation and characterisation of $NiO–Ce_{0.8}Gd_{0.2}O_{1.9}$ composite nanofibres via electrospinning. *Micro. Nano. Lett.* **7**, 1316-1319 (2012).

57. Zhang, Y. *et al*. Effects of Ce/Zr composition on nickel based $Ce_{(1-x)}Zr_xO_2$ catalysts for hydrogen production in sulfur–iodine cycle. *Int. J. Hydrogen Energy* **39**, 10853-10860 (2014).

58. Dantas, S. C., Escritori, J. C., Soares, R. R. & Hori, C. E. Effect of different promoters on $Ni/CeZrO_2$ catalyst for autothermal reforming and partial oxidation of methane. *Chem. Eng. J.* 1**56**, 380-387 (2010).

Chapter 3 - **Single molecule study of microenvironment acidity in the pore structure of silicate thin films**

3.1 Introduction

Silica based mesoporous structures have attracted great attention recently due to their wide application in catalysis,[1, 2] nanofluidic devices[3, 4]and gas sensors.[5] It is well known that the acidic sites in the pores are important in the application of silica based mesostructures in various areas. For instance, silica based porous structures showed high activity in various reactions including dehydration,[6] hydrolysis[7] and cracking.[8] Moreover, shape-selectivity can be achieved with mesoporous catalysts due to a combination of acidity and nanoconfinement.[1, 9, 10] For example, SBA-15 and MCM-41 supported sulfonic acid catalysts showed high selectivity for monoglyceride synthesis from glycerol and fatty acids.[9] Also, the surface of mesopores could be negatively charged due to deprotonation of the incorporated acid sites. The negatively charged surface combined with the nanoconfinement of the pore structure make silica based mesoporous structures ideal candidates for nanofluidic device applications.[11, 12]

The ensemble average properties of silica-based mesoporous structures have been studied via various characterization methods. For instance, temperature-programmed desorption (TPD), FTIR, and NMR spectroscopy are applied for the acidity measurement of mesoporous catalysts.[13-16] Recently, single molecule spectroscopy was also applied for local property measurements in mesoporous structures. The diffusion of dye molecules in hexagonal and laminar mesostructures was investigated both via single molecule fluorescence correlation spectroscopy (FCS)[17-19] and single-molecule tracking (SMT).[20-25] Studies of the acidity of silica-based mesostructures are still rare.[26, 27]

C-snarf-1 and other pH sensitive dual emission dye molecules are widely used as fluorescent pH indicators in biological systems[28-30] and for material characterization.[26, 31-33] For example, Mai et al. investigated the impact of concentration polarization on pH distribution in microfluidics via the assistance of C-snarf-1.[33] These dye molecules can be used to study local acidity because the ratio of intensities at two different emission wavelengths is known to vary with pH. Usually, a calibration curve of emission ratio at different pH values is necessary to use these dye molecules to study the pH of a particular environment. Although the calibration curve of C-snarf-1 in aqueous solution is easy to achieve, it has been reported that the absorption of C-snarf dye molecules onto the surfaces of biosystems may lead to a change in the dye response.[34-36] Thus, errors may occur when C-snarf-1 is applied for the measurement of pH in complex systems such as living cells[36] and much more precise calibration is needed for measurements made in such systems. Due to the large specific surface area of mesoporous structures, it is possible that many dye molecules will be absorbed on the material surface, altering their behavior through interactions with the surfaces.

Another complicating factor for using fluorescent probes to study mesoporous structures is how to incorporate them into the material. Dye molecules are often incorporated directly with the precursor sol-gel solution containing surfactants without further calcination.[20, 21, 24, 27] However, for catalysis and device applications, removal of the surfactant from the mesoporous structure is important, which can damage the fluorescent probe. On the other hand, if calcined silica thin films are applied for single molecule spectroscopy study by loading dye molecules into the mesopores through spin coating or diffusion, it is a challenge to differentiate whether the signals of dye molecules are from the surface of the films or from the pores.[17, 26]

In this work, a microfluidic device with two parallel channels was fabricated by sealing a PDMS block on top of a mesoporous silicate thin film. Aqueous solutions of different pH and concentrations of C-snarf-1 dye molecules were flowed through the two channels in these experiments. The fluorescence emission from C-snarf-1 dye molecules diffusing into the mesopores of the silicate thin film between the two channels was measured and analyzed via single molecule spectroscopy. Since the surface of the mesoporous silicate thin film is sealed by the PDMS block, signals from dye molecules on top of the silicate film could be eliminated and pore structures of materials could be guaranteed in a solvent immersion condition, which is close to the condition of their potential application. Furthermore, the pH value within the pore structures could be adjusted externally via flowing solutions of different pH through the two channels. The calibration curve of emission ratio in mesopores as a function of pH was achieved through this method and the impact of interaction between silicate walls and dye molecules on the emission ratio was investigated.

3.2 Experimental section

3.2.1 Materials

C-snarf-1 was purchased from Invitrogen and was used as received. Both Tetraethyl orthosilicate (TEOS, 99 %) and Pluronic P-123 were obtained from Sigma-Aldrich. Zipcone UA (PP1-ZPUA) was obtained from Gelest Inc. (Morrisville, PA, USA). Norland Optical Adhesive 74 was obtained from Norland Products (Cranbury, NJ, USA).

3.2.2 Sample preparation

The mesoporous silica (SBA-15) thin films were prepared on glass microscope coverslips via a dip-coating method followed by temperature programmed calcination as described in previous papers[3, 37]. The coverslips were cleaned by rinsing with acetone and nanopure water and dried under nitrogen flow, followed by plasma treatment for 5 min. To prepare the silica sol for dip coating, P123 (0.1337 g 0.0231 mmol) and TEOS (0.45 g 2.16 mmol) were dissolved in 17.4 g of ethanol with vigorous stirring. After that, water (0.234 g, 13 mmol) and 0.1M HCl (0.045 g, 0.0045 mmol) were added and the solution was stirred for 2 h at room temperature. During the dip coating process, the coverslip was immersed into the silica sol and withdrawn vertically at a speed of 0.025 mm/s at room temperature with the moisture controlled at 40 %. The as-prepared thin films were then aged for 48 h and calcined at 350 ^{o}C for 6 h. The calcined thin films were finally hydrothermally treated in 0.1 M HCl solution at 120 ^{o}C for 3 h.

The microfluidic device was prepared by a replica molding method (See Figure B1 Appendix B). The positive reliefs for PDMS molding were prepared on glass slides by a photolithography method with a 40 %:60 % mixture of Zipcone UA, an acryloxy-terminated siloxane polymer, and Norland Optical Adhesive 74 (NOA 74), an acrylate based polymer as photoresist. PDMS prepolymer and hardener were mixed in a 10/1 ratio and cast on the positive reliefs. The PDMS stamp could be peeled off from the relief after curing at 80 ^{o}C for 48 h so that the PDMS stamp was fully crosslinked.

Both the PDMS stamp and fresh hydrothermally treated meso thin film-coated glass coverslip were then plasma treated for 5min and sealed together under certain pressure for 4 h.

3.2.3 Instrumentation and methods

Before SM measurements, solutions with different pH values and 10 nM C-snarf-1 dye molecules were flowed through the two channels of the microfluidic device for 48 h. The behavior of dye molecules diffusing into the sealed mesopores between the two channels was studied via SM measurement while the solutions continued to flow through the microchannels to maintain the pH value of the mesopores.

All SM studies were carried out on a wide-field fluorescence microscope as described previously (See Figure B2 Appendix B). [26] This system is built on an inverted epi-illumination microscope (Nikon TiE). Light from a Nd:YVO_4 laser (Coherent, Verdi, 532 nm) source was applied to excite the C-snarf-1 dye molecules. It was first focused into a spinning optical diffuser and then collected and passed through a polarization scrambler before being directed into the epi-illumination port of the microscope. The light was then reflected from a dichroic beam splitter (Chroma Q555LP) and focused into the back aperture of an oil immersion objective (Nikon Apo TIRF 100X, 1.49 N.A.). The incident laser power was maintained between 1.5 and 2.0 mW. The total internal reflection fluorescence (TIRF) mode was applied for data collection to reduce background fluorescence from the PDMS. Fluorescence from the sample was collected with the same objective and separated from the incident laser light by passing back through the beam splitter and a 542 nm long-pass filter. The fluorescence was subsequently directed into an image splitter (Cairn Research, OptoSplit II), where it was further split by a second dichroic beam splitter (Chroma, 610dcxr). The two signal beams were individually directed through two band-pass filters: one centered at 580 nm, the other at 640 nm, both with 40 nm passbands. Images at these two wavelengths were then simultaneously recorded on a back-illuminated EM-CCD camera (Andor iXon DU-897). The individual, well-separated dye molecules appeared as

well-defined pairs of spots in the two images. Software written in house (based on the National Instruments Labview platform) was used to extract the side-by-side images, correct for any distortion of these images, locate the individual spot pairs, and finally, to fit their profiles to Gaussian functions. Image distortion consisted only of translational offsets in X and Y and a slight rotation of the images. The rotation was always $< 2^{o}$ and was easily removed. The amplitudes of the Gaussian fits were used to determine the emission ratio (I_{580}/I_{640}) for each molecule.

The ensemble averaged emission ratio from C-snarf-1 aqueous solution at different pH was acquired on the same instrument used in the single molecule spectroscopy studies. During these measurements, 1 μM C-snarf-1 aqueous buffer solution was dropped into a homebuilt microcell that was mounted on top of a glass cover slide and positioned on the microscope. Fluorescence signals collected from both channels were analyzed with Image J to obtain the ensemble averaged intensity ratio. For this purpose, the average signal in each channel was measured by selecting 122 x 100 pixel regions and then subtracting the background, as measured under dark conditions, from these values.

A Rigaku three-pinhole S-MAX3000 SAXS instrument with a microfocus Cuκ (λ=1.54 nm) sealed tube source was used for mesoporous structure characterization. Samples were encapsulated between two pieces of polyimide tape. The size of the beam at the sample was ~ 0.4 mm. Pixel-to-angle conversion was determined via scattering from a silver behenate sample.

3.3 Results and discussion

3.3.1 Characterization of mesoporous silicate thin films

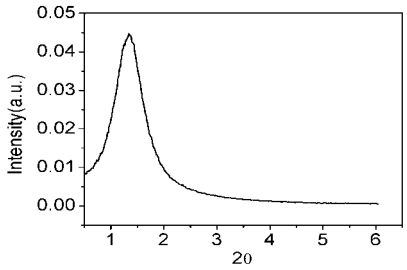

Figure 3.1 Small angle X-ray diffraction pattern of SBA-15 mesoporous structure.

The small angle X-ray diffraction pattern was obtained from powder samples, which were prepared via solvent evaporation of exactly the same silica sol for dip coating followed with calcination with the same temperature program as thin film samples. As shown in Figure 3.1, strong diffraction pattern correspond to (100) lattice plane is located at $2\Theta=1.33^{o}$, giving a d space of 6.6 nm. Thus, the center-to-center distance of mesopores is calculated as 7.6 nm. The thickness of the mesoporous thin films after calcination is measured as 96nm via ellipsometry.

3.3.2 Experiment design for SM study of local acidity of pore structure

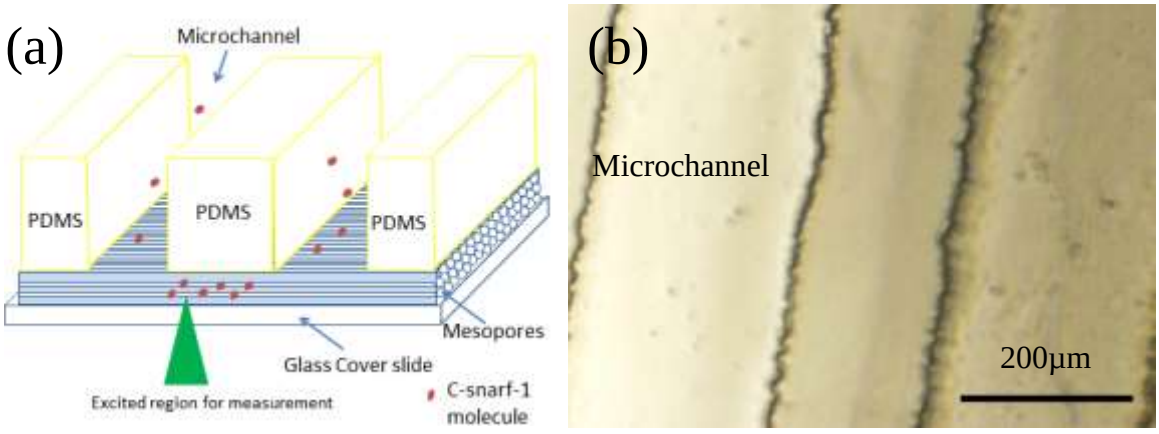

Figure 3.2 (a) Schematic illustration of microfluidic device for single molecule spectroscopy measurements. (b) Microscope image of microfluidic channels and sealed region between 2 channels.

As shown in Figure 3.2 a, to ensure the fluorescent signals of C-snarf-1 dye molecules are from those molecule embedded in the mesopores of the silicate thin film, a PDMS stamp is applied to seal the surface of mesoporous thin film. A solution of dye molecules flows through the micro channels. These molecules can be adsorbed into the meso-structure under the micro channels and diffuse laterally into the pores of the silica thin film under the PDMS stamp-sealed region in between the two channels. The molecules that have diffused into the pores of the mesoporous thin film under the PDMS stamp sealed region are measured with a wide-field fluorescence microscope.

Figure 3.2 b shows that the width of the PDMS stamp sealed region is measured as 175 μm, which is slightly less that the size of microscopic field of view. One crucial point for the experiment setup is to ensure that fluorescent signals during measurement are from dye molecules trapped in the mesopores of the silicate thin film. Figure 3.3 a shows the wide-field fluorescence image (580 nm detection channel) of C-snarf-1 dye molecules under the PDMS covered region when a glass cover slide with no mesoporous silicate thin film was applied as the substrate of microfluidic device. Due to the lack of mesopores for dye molecules to diffuse in, few fluorescent spots can be observed from the image. The observed dye molecules probably come from the cracking of PDMS stamp or the contamination of the microfluidic device. When a glass cover slide coated with a disordered mesoporous silicate thin film with an average pore size of 6.8 nm (Figure 3.3 b) or thinner layer (10 nm) of hexagonal SBA-15 thin film (Figure 3.3 c) is applied for SM study, more fluorescent spots can be observed. However, the density of the dye molecules is still low. With further increasing of the SBA-15 layer thickness to roughly 100 nm (Figure 3.3 d), a suitable density of dye molecules for SM study is achieved. The hexagonal structure showed higher efficiency than a disordered structure for the loading of dye molecules.

This phenomenon can be ascribed to the slightly larger pore size and less tortuosity. From Figures 3.3 a, b and d, it can be concluded that the PDMS stamp sealed the surface mesoporous structure and dye molecules mainly diffused into the observed region through the mesoporous silicate thin film. Furthermore, the thickness dependence of the dye molecule density indicates that the majority of dye molecules are trapped in the mesopores instead of being adsorbed on the surface of the PDMS stamp or glass substrate.

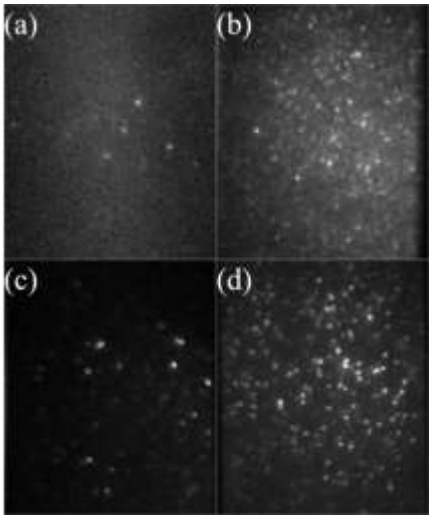

Figure 3.3 Wide field image of a PDMS stamp-covered area with different substrates: (a) glass cover slide with no mesoporous silicate thin film;(b) glass cover slide coated with a disordered mesoporous silicate thin film (c) 10nm thick SBA-15 coated cover slide; (d) 100nm thick SBA-15 coated cover slide.

A key objective of the proposed research is to be able to measure fluorescence as a function of position in the mesoporous silicate films. To help meet this objective, experiments were run to measure the position of a specific fluorescent molecule. To locate the illuminated position for wide field fluorescence measurement, the dimmed laser light was reflected via a Chroma Q505LP dichroic beam splitter into the back aperture of an oil immersion objective with the microscope illuminator on (See Figure B3 Appendix B). The illuminator was applied to illuminate the whole field of view. Because a Chroma Q505LP dichroic beam splitter instead of

a Chroma Q555LP dichroic beam splitter is applied, the 532 nm laser light spot reflected from sample was not filtered by the dichroic beam splitter and could be recorded via a canon EOS rebel T3 camera (Figure 3.4). The position of the laser light spot slightly deviated from the position where it should be when a Chroma Q555LP dichroic beam splitter was used during SM study. The deviation was corrected via comparison between the fluorescent image of fluorescence microspheres casted thin film with Q555LP dichroic beam splitter and the image of laser spot with Q505LP dichroic beam splitter.

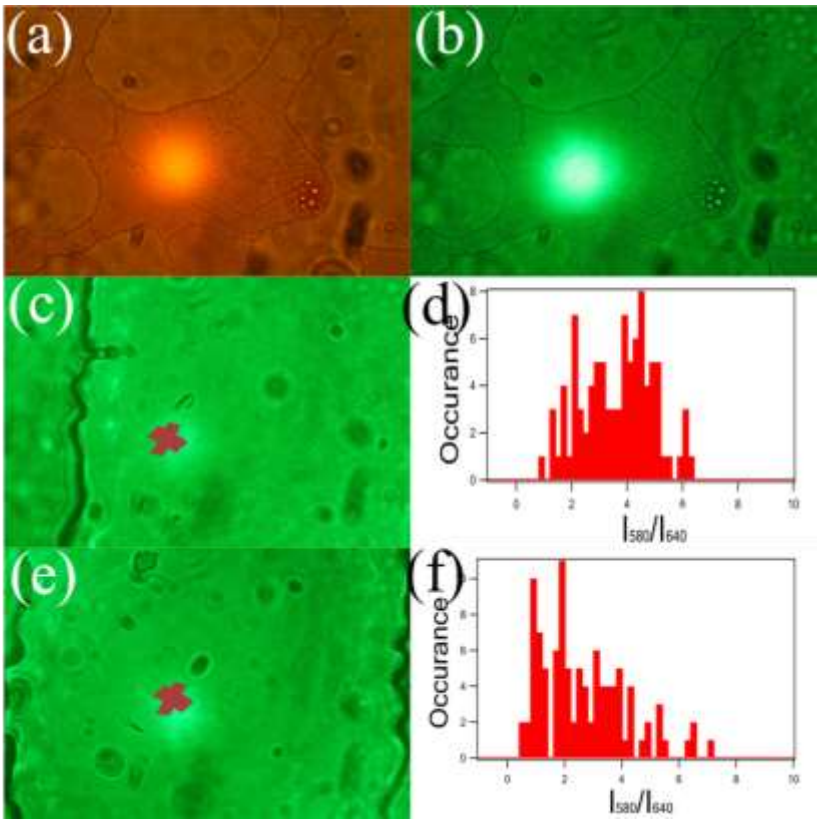

Figure 3.4 (a) Emission from fluorescent spheres with a Chroma Q555LP dichroic beam splitter for reflection and filtering of incident laser light. (b) Reflected incident laser light spot from the same fluorescent sphere thin film with a Chroma Q505LP dichroic beam splitter utilized to replace the ChromaQ555LP dichroic beam splitter. (c,e) Reflected incident laser light spot with a Chroma Q505LP dichroic beam splitter utilized to show the location for SM measurement. The marked spot is the calibrated position for SM

measurement when Q555LP dichroic beam splitter is applied. (d, f) The emission ratio histogram obtained from the SM study from the position showed in c and e.

3.3.3 SM study of acidity of silicate pore structure

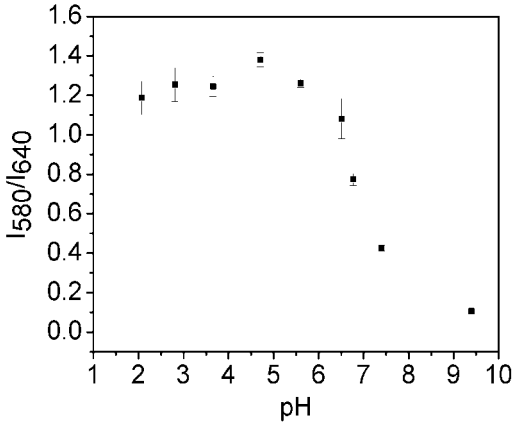

Figure 3.5 Emission ratio I_{580}/I_{640} versus pH value in bulk aqueous solution.

C-snarf-1, a pH indicator widely applied in various systems, was selected for local pH measurements in mesoporous silicate thin films. As a ratiometric dual emission fluorescent probe, the ratio of two different fluorescence emission bands centered at 580 nm and 640 nm (I_{580}/I_{640}) vary with changes in the pH of the surrounding environment. The ensemble average emission ratio of C-snarf-1 dye molecules in aqueous buffer solution with different pH was acquired using the same instrument and method as the SM study. Buffer solution with 1μM C-snarf-1 was applied for the ensemble average emission ratio study. The intensity from 580 nm and 640 nm channels are used directly for ensemble average emission ratio calculation. Figure 3.5 is a plot of ensemble average emission ratio versus pH in aqueous buffer solution obtained from the microscope when C-snarf-1 was used as a fluorescent probe. Due to the triprotic acid nature of C-snarf-1[26], the emission ratio increases with increasing pH until it reaches a maximum

at around pH 5. With further increases in pH value, the emission ratio drops dramatically to a value of 0.1 at pH 9.4.

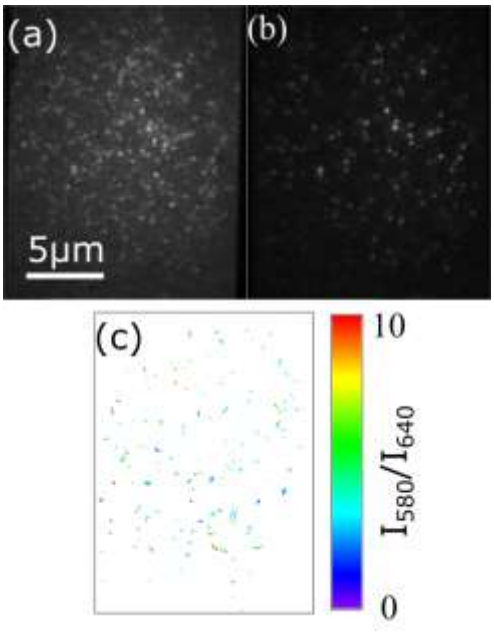

Figure 3.6 (a,b) Z-projection images of C-snarf-1 dye molecules in mesoporous silica thin films for the 640 and 580 nm detection channels. The pH value of HCl solutions flowing in the adjacent microchannel is 4.7. (c) Single molecule trajectories obtained from the same videos. The emission ratio I_{580}/I_{640} of C-snarf-1 dye molecules are reflected via the color of the trajectory.

Figure 3.6 a and b show the stacked images of dispersed individual C-snarf-1 molecules for the 640 nm and 580 nm detection channels in the PDMS sealed region after 48 h diffusion. The bright spots are from the fluorescent emission of C-snarf-1 dye molecules detected through the corresponding channel. The fluorescent spots from Figures 3.6 a and b were fitted to Gaussian functions. The intensity of single fluorescent probes for emission ratio measurement were obtained from the amplitude of each Gaussian function while the precise local position of single fluorescent probes were provided via the fitting process as the center of the Gaussian. The local position of C-snarf-1 probes was further linked by the trajectories as shown in Figure 3.6 c. Note that only trajectories with lengths great than 6 frames were collected for data analysis. The trajectories showed that most of the dye molecules are immobile and likely entrapped in the

pores of the silicate structure, which agrees with the previous SMT study of dye molecules in mesoporous silicate thin films.[21] However, a small fraction of C-snarf-1 dye molecules in the mesoporous thin film are mobile and suitable for SMT study.

The trajectories were also color coded for the description of emission ratio of single dye molecules from two different channels every frame. As shown in Figure 3.6 c, the color of the trajectory segments changes from deep blue, which indicates a emission ratio of less than 1, to red, which represents a emission ratio of 10. The fluorescence emission ratio varies significantly between different dye molecules, which may indicate heterogeneity within the pore structure of the silicate thin film.

In order to measure the response of C-snarf-1 dye molecules inside the pores of the silicate thin films to different pH, solutions with different pH values were flowed through the microchannels adjacent to the observed region. The acid solution used to adjust the pore pH was an aqueous HCl solution, while the base solution used to adjust the pore pH was an aqueous NaOH solution. Buffer solution was not used to prevent ionic strength from impacting the emission ratio of dye molecules. Histograms of the SM emission ratios are used to describe the response of C-snarf-1 dye molecules in the mesopores to different pH values. Note that the SM emission ratio for one molecule is achieved via averaging the emission ratio measured in each frame through the whole trajectory length of that molecule. Data acquired from five different spots with similar conditions is plotted in one histogram to guarantee that enough single molecules signals are collected. For convenience, the emission ratio calculated via averaging through the whole trajectory of one molecule is denoted as R_{traj}.

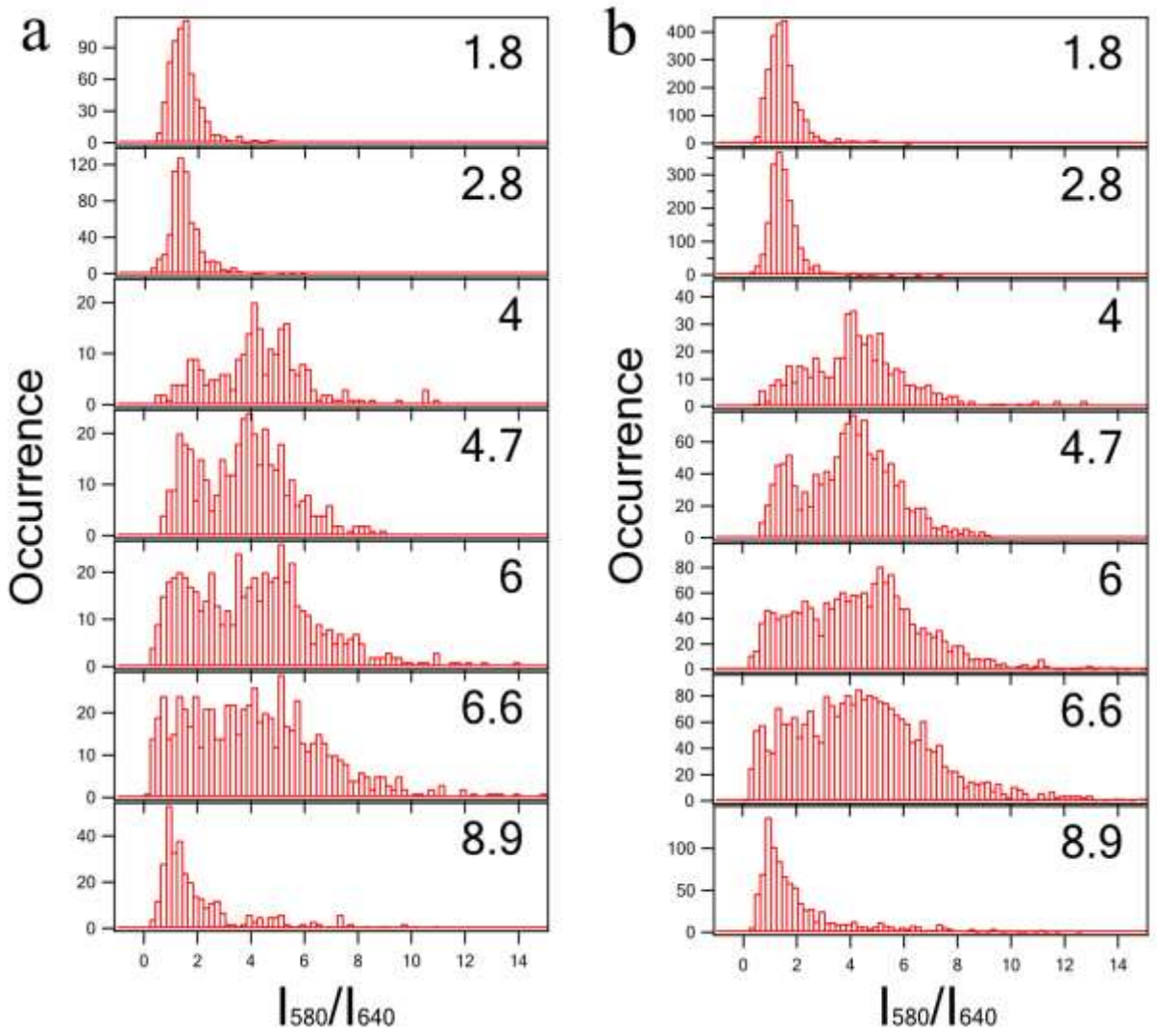

Figure 3.7 The SM emission ratio (I_{580}/I_{640}) histogram of C-snarf-1 diffused in the pores of a SBA-15 thin film. The pH value of aqueous solution in the pores could be calibrated by flowing solutions with specific pH value through the micro channels adjacent to the region for measurement: (a) emission ratios calculated via averaging through the whole trajectory of single molecule, (b) emission ratios calculated by averaging through trajectory segments at unique position.

As shown in Figure 3.7 a, at very low pH (pH 1.8 and 2.8), the histograms of SM dye molecules show both low emission ratio and a narrow distribution. For example, at pH 1.8, the average R_{traj} is 1.5 with a standard deviation of 0.67. Similar data also can be observed for pH 2.8. With an increase in pH, both the average R_{traj} and standard deviation increase. From pH 4 to

pH 6.6, the average R_{traj} are all around 4 while the standard deviation of R_{traj} increases from 1.8 for pH 4 to 2.7 for pH 6.6. Further increases in the solution pH in the silicate thin films by flowing a base solution in the micro-channels leads to a decrease in R_{traj}. The trend of SM R_{traj} versus pH is similar to what was observed in previous studies of uncalcined silicate films and calcined films with dye molecules loaded both in the pores and on the surface of the films. For instance, both Fu et al. and Sun et al. reported that the standard deviation or width of the emission ratio distribution always reached its maximum at pH 6 or 7. Also, the average emission ratio of the dye molecules loaded into the silicate films in both this work and Sun's paper decreased at very low pH. However, as shown in Figure 3.7 a and Table 3.1, the average and standard deviation of R_{traj} in this work are much larger than those reported in the previous work. Consequently, Gaussian fitting is not suitable to depict the distribution of R_{traj} in this work. The larger average R_{traj} may be induced by the interaction between C-snarf-1 dye molecules and the pore wall of silicate thin films while the broad distribution of R_{traj} could be ascribed to both the heterogeneity in acidity of the silicate thin films and different kinds of interactions between the silicate thin film and C-snarf-1 dye molecules.

As shown in Figure 3.6 c, even for one mobile single molecule trajectory, the emission ratio varies with the change of position which further indicates the local variation of environment in silicate mesopores. Considering the possibility of mobile molecules traveling through spots with varying local acidity and environment, R_{traj} reflected the average emission ratio of different environments for mobile molecules which is not accurate enough to reveal the real local acidity. Thus, instead of averaging the emission ratio through the whole trajectory, the emission ratio of C-snarf-1 dye molecules from trajectory segments at the same position is averaged. In this work, spots with displacements less than 2.15 times of mean local precision along the same trajectory

were allocated to a unique position. The mean local precision is calculated to be 22.5 nm as described in previous work.[38] The emission ratio from each trajectory segment at a unique position is denoted as R_{reg}. Figure 3.7 b shows the histogram of R_{reg} from the same SM videos of Figure 3.7 a. However, not much difference could be found between Figure 3.7 a and b. For all pH, both the average value and standard deviation of R_{traj} or R_{reg} show similar values (Table 3.1).

Interestingly, if R_{reg} is calculated from single molecules with R_{traj} in a short interval, a much broader distribution of emission ratio could be observed. Figure 3.8 a shows the histogram of R_{traj} in a short interval centered at average R_{traj}. The span of the emission ratio interval for pH 4 to pH 6.6 is 1 while the span for pH 1.8, 2.8 and 8.9 is 0.6. Figure 3.8 b exhibits the R_{reg} histogram of the same molecules from Figure 3.8 a. A Gaussian-like distribution of R_{reg} is observed.

To further understand the impact of interactions between C-snarf-1 dye molecules and the pore walls of silicate thin films, the SM emission ratio of mobile molecules versus their diffusion coefficient is plotted (Figure 3.9). The sorting of mobile molecules from all the single molecules is based on our previous work.[18] Mean square displacement (MSD) and mean localization variation (σ^2) of dye molecules are compared to determine the mobility of the molecules. If MSD>4.6 σ^2, the molecule is considered to be mobile. Otherwise, the molecule is classified as immobile. The diffusion coefficient of mobile molecules is also calculated through the Einstein-Smoluchowski relation.

$$\langle MSD \rangle = 2dDt \tag{3.1}$$

where d=1, 2 or 3 corresponding to one-, two- or three-dimensional diffusion, and D is the diffusion coefficient. Since the pores within the mesoporous silicate thin film are not aligned, self-diffusion of the dye molecules in the silicate matrix is isotropic in the film plane. Thus, d is

selected as 2 in this work. The mobile molecules for analysis in Figure 3.9 are from the same videos used for the histogram study in Figure 3.7. The red lines in Figure 3.9 are the average R_{traj} of all the dye molecules. At all pH values, for dye molecules with low diffusion coefficients, a broad distribution of emission ratios is observed. With the increase in diffusion coefficient, the emission ratio converges to a value slightly less than the average value of all molecules. This trend is clearer if the emission ratios of molecules with diffusion coefficients greater than the median diffusion coefficient of all mobile molecules at certain pH are sorted out and analyzed. As shown in Figure 3.10 and Table 3.1, the R_{traj} of fast moving molecules showed a narrower distribution and a smaller average emission ratio. In the case of the average emission ratio, note the standard error of the average emission value could be calculated form the standard deviation of emission ratio and the number of molecules measured. The standard deviation of average R_{traj} for both mobile and immobile molecules were 0.02, 0.03, 0.12, 0.09, 0.10, 0.10 and 0.10 for pH 1.8, 2.8, 4, 4.7, 6, 6.6 and 8.9. Also, the standard deviation of average R_{traj} for fast moving molecules were calculated as 0.04, 0.09, 0.21, 0.18, 0.27, 0.27 and 0.33 for pH 1.8, 2.8, 4, 4.7, 6, 6.6 and 8.9. For pH 1.8 to pH 6.6, the difference between the average R_{traj} of all measured molecules and the R_{traj} of fast moving molecules are greater than or close to the sum of their standard deviations. Thus, the credential for the small R_{traj} for fast moving molecules could be proved. Also, the R_{reg} of fast moving molecules showed a similar distribution and average value as the R_{traj} of the same molecules.

For fast moving molecules, the narrow distribution of R_{traj} has two possible origins. First, note that the moving molecules within the mesopores may be adsorbed on or otherwise interact with mesopores of different microenvironments during diffusion. Hence, the averaging of emission ratio of C-snarf-1 dye molecule from varying microenvironments may give an overall

emission ratio that is close to the average emission ratio of all molecules. Second, regions in the mesoporous silicate structure through which fast moving molecules diffuse may show less heterogeneity. The narrow distribution of R_{reg} demonstrated the lower heterogeneity of mesoporous silicate structures through which the fast moving molecules diffuse. Considering that the fast moving molecules are more likely to be found in ordered pores with less tortuosity, the emission ratio of fast moving molecules may represent the response of C-snarf-1 dye molecules in these more homogeneous structures. On the other hand, molecules entrapped in dead ends and defective structures are more likely to exhibit a broad emission ratio distribution with very large or small emission ratios.

Table 3.1 Average values and standard deviations of C-snarf-1 emission ratios in the pore structure of silicate thin films. (ave indicates the average emission ratio, sdev is the standard deviation of emission ratio.)

pH	R_{traj} (ave)	R_{traj} (sdev)	R_{reg} (ave)	R_{reg} (sdev)	R_{traj} (ave) (fast mobile)	R_{traj} (sdev) (fast mobile)	R_{reg} (ave) (fast mobile)	R_{reg} (Sdev) (fast mobile)
1.8	1.50	0.67	1.52	0.70	1.39	0.43	1.36	0.46
2.8	1.52	0.69	1.49	0.61	1.39	0.51	1.35	0.38
4	4.22	1.84	4.28	1.93	3.58	1.78	3.48	1.52
4.7	3.71	1.73	3.95	1.73	3.48	1.34	3.55	1.31
6	4.06	2.38	4.46	2.44	4.70	2.15	4.77	2.17
6.6	4.16	2.71	4.48	2.60	3.44	2.51	3.73	2.65
8.9	2.20	1.94	2.29	2.11	2.11	1.22	2.56	1.83

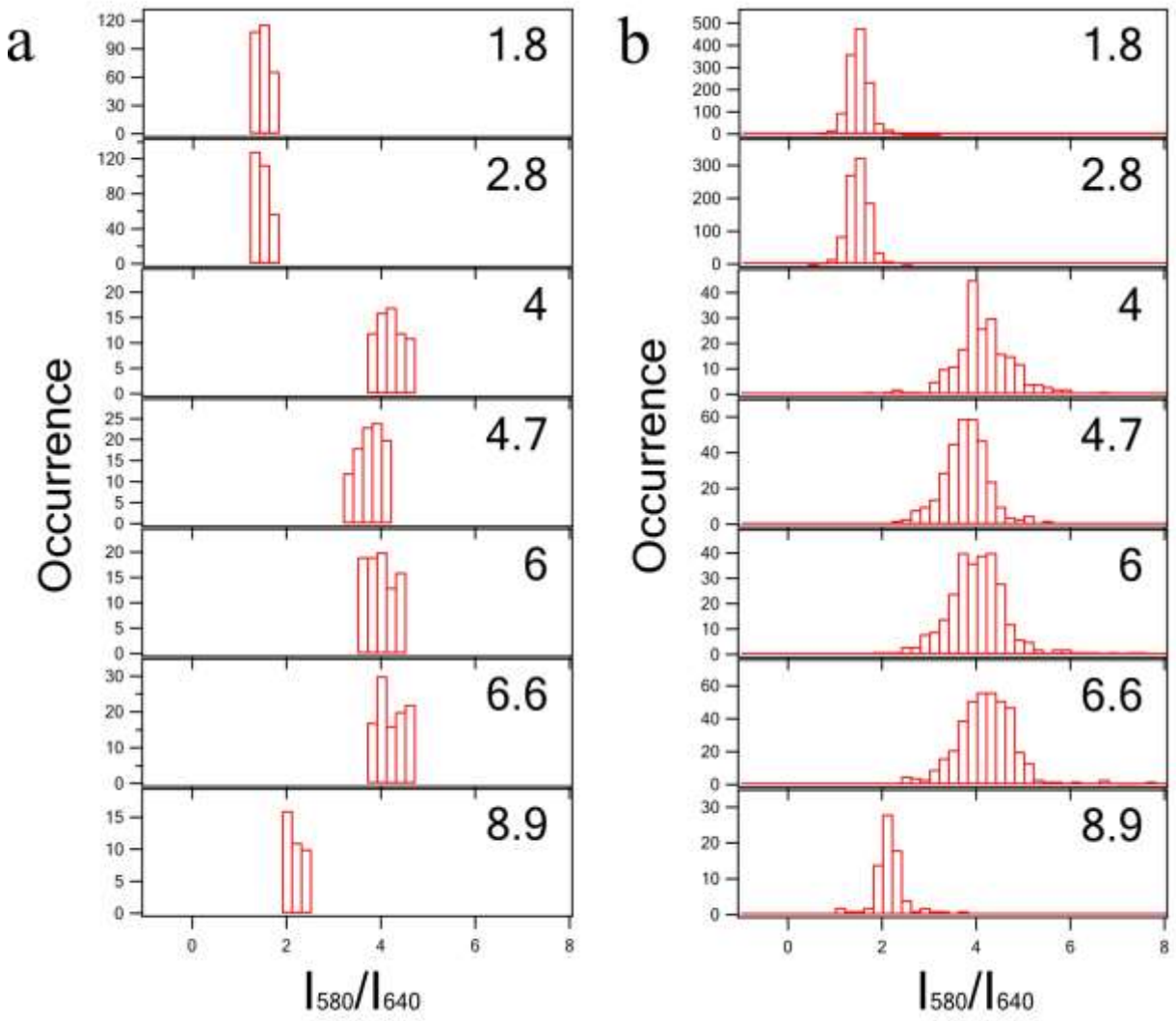

Figure 3.8 The SM emission ratio (I_{580}/I_{640}) histogram of C-snarf-1 with R_{traj} in a short interval; (a) emission ratio calculated by averaging through the whole trajectory of single molecule, (b) emission ratio calculated by averaging through the trajectory segments at unique position from the same molecules of Figure 3.8 a.

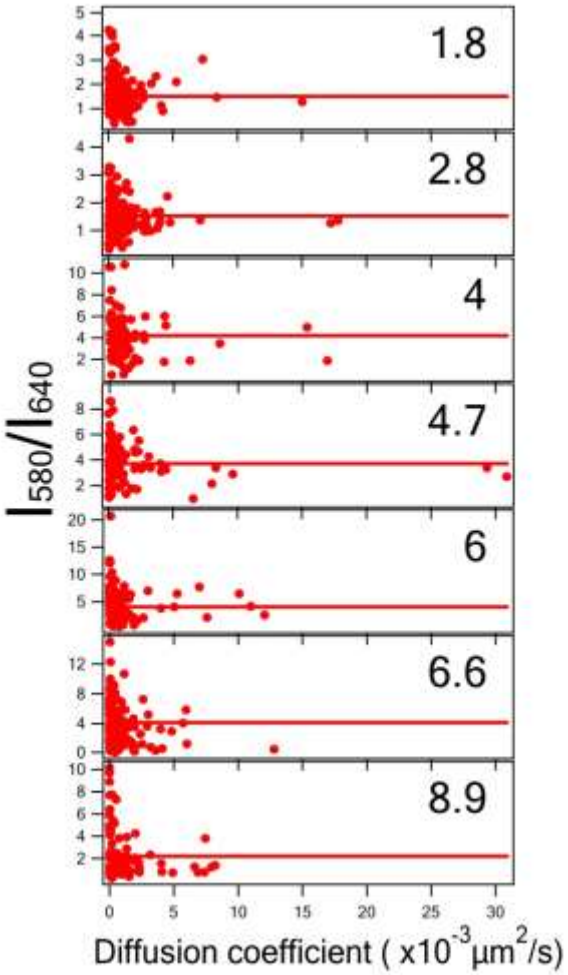

Figure 3.9 Plot of emission ratio vs diffusion coefficient of mobile molecules in the silicate thin films at different pH value.

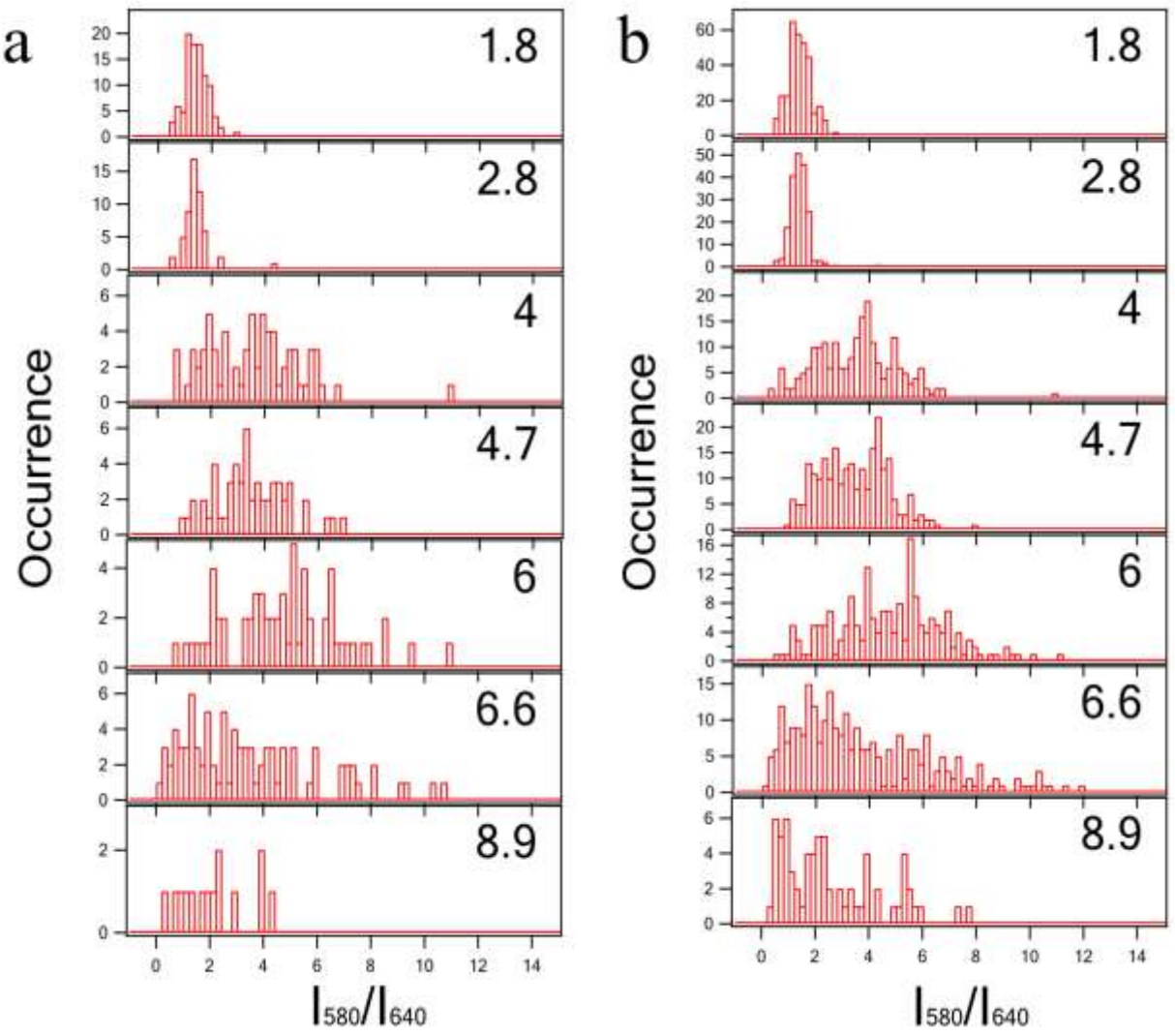

Figure 3.10 The SM emission ratio (I_{580}/I_{640}) histogram of fast moving C-snarf-1 dye molecules in the pore structure of a silicate film; (a) emission ratio calculated via averaging through the whole trajectory of single molecule, (b) emission ratio calculated via averaging through trajectory segments at a unique position from the same molecules of Figure 3.10 a.

3.3.4 Impact of ionic strength on the emission ratio of dye probe

Note that the emission ratio of C-snarf-1 in mesopores at low pH showed a similar average value to that observed at the same pH in bulk solution. The distribution also appeared to be Gaussian, with a narrow width (Figure 3.7a and b). The deprotonation of the silicate surface will be fully suppressed at low pH with a reported isoelectric point at pH 2.6.[3] The interaction between C-snarf-1 dye molecules and the solid surface is complex and the mechanism for variation of emission ratio induced by the interaction between C-snarf-1 and biosurface still ambiguous.[34-36] Here, we also observed the variation of emission ratio of C-snarf-1 due to the interaction between dye molecules and silicate pores. Moreover, the silicate pore structure is featured with surface charging, hydrogen bonding, and nanoconfinement. Exploration the impact of these characteristics on the emission ratio of C-snarf-1 would be helpful for the future research and application. By flowing solutions with different concentration of NaCl but similar pH value through the microchannels, the ionic strength of the solution in the mesopores is adjustable. It has been reported that the emission ratio of C-snarf-1 dye molecules[39] is largely independent of ionic strength in aqueous solution for biological system. Hence, adding certain concentration of NaCl solution may not vary the emission property of C-snarf-1 dye molecules (Figure B4 Appendix B), however, the interaction between dye molecules and pore surface could be changed.

Figure 3.11 displays the emission ratio histogram of dye molecules at pH 5 with different NaCl concentrations while Figure 3.12 plots the emission ratio versus diffusion coefficient for mobile molecules from the same videos used in Figure 3.11. A drop in the average emission ratio to a low value can be observed with an increase in ionic strength. When the concentration of NaCl is 100 mM, the average R_{traj} is 3.04 while the average R_{traj} decreases to 2.76 when the

concentration of NaCl reaches 1M. Interestingly, the emission ratios of mobile dye molecules never converge to the average value of all molecules (Figure 3.12). Instead, they converge to a value around 2.

The shift in the emission ratio could reflect a decrease in pK_a due to the high concentration of NaCl. However, the ensemble average fluorescent emission ratio in aqueous solution doesn't change for NaCl concentrations up to 100 mM. The shift of the emission ratio is attributed to reduced interactions between the dye and silica pore surfaces as discussed above. Thus, the emission ratio shifts to a lower value, which is close to the behavior of C-snarf-1 in solution. Further experiments would be necessary to distinguish the two effects.

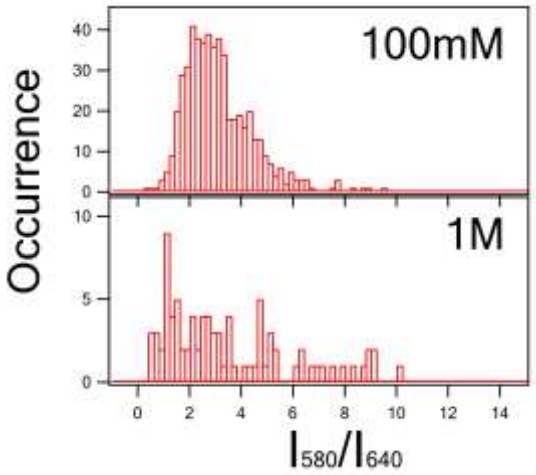

Figure 3.11 SM emission ratio (I_{580}/I_{640}) histograms of C-snarf-1 diffused into the pores of a SBA-15 thin film. The pH value of the aqueous solution is fixed at around 5 while the ionic strength of the solution was adjusted by varying the concentration of NaCl.

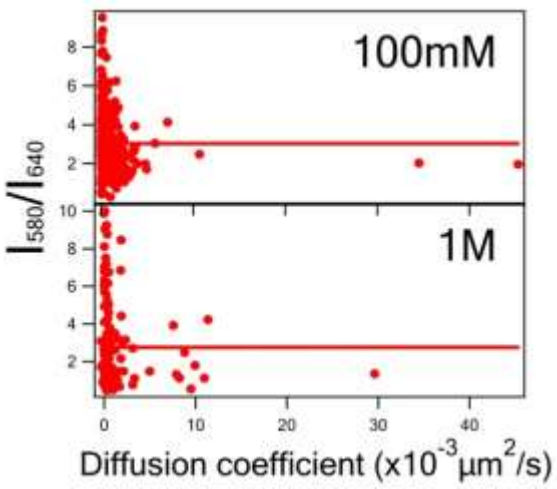

Figure 3.12 Plot of emission ratio vs diffusion coefficient of mobile molecules in the silicate thin films at pH 5 with different NaCl concentration

3.4 Conclusion

In this work, the local acidity within the pores of mesoporous silicate films was studied via single-molecule fluorescence spectroscopic methods. The ratiometric pH-sensitive dye C-snarf-1 was applied as the fluorescent probe. A microfluidic device was utilized to seal the surface of the mesoporous silicate film and help to ensure that the dye molecules are embedded into the pores of the film. The SM data showed a wide distribution and high average emission ratio comparing to previous work. The average emission ratio increased with increasing pH until pH 6 to 7 where it peaked and subsequently decreased with further increases in pH. Mobile and immobile molecules displayed differences in both averages and standard deviations of the emission ratio, which indicated that interactions between C-snarf-1 and the pore walls affected the emission ratio. The reduction in emission ratio of mobile molecules caused by an increase in ionic strength also implies a role for the interactions between the silica pore surface and dye molecules in determining the emission ratio of C-snarf-1.

References

1. Weisz, P. B. Molecular shape selective catalysis. *Pure Appl. Chem.* **52**, 2091-2103 (1980).

2. Martínez, A., López, C., Márquez, F. & Díaz, I. Fischer–Tropsch synthesis of hydrocarbons over mesoporous Co/SBA-15 catalysts: the influence of metal loading, cobalt precursor, and promoters. *J. Catal.* **220**, 486-499 (2003).

3. Fan, R., Huh, S., Yan, R., Arnold, J. & Yang, P. Gated proton transport in aligned mesoporous silica films. *Nat. Mater.* **7**, 303-307 (2008).

4. Kuo, T. *et al*. Gateable nanofluidic interconnects for multilayered microfluidic separation systems. *Anal. Chem.* **75**, 1861-1867 (2003).

5. Wagner, T., Haffer, S., Weinberger, C., Klaus, D. & Tiemann, M. Mesoporous materials as gas sensors. *Chem. Soc. Rev.* **42**, 4036-4053 (2013).

6. Takahara, I., Saito, M., Inaba, M. & Murata, K. Dehydration of ethanol into ethylene over solid acid catalysts. *Catal. Lett.* **105**, 249-252 (2005).

7. Onda, A., Ochi, T. & Yanagisawa, K. Selective hydrolysis of cellulose into glucose over solid acid catalysts. *Green Chem.* **10**, 1033-1037 (2008).

8. Verheyen, E. *et al*. Molecular shape-selectivity of MFI zeolite nanosheets in n-decane isomerization and hydrocracking. *J. Catal.* **300**, 70-80 (2013).

9. Pérez-Pariente, J., Díaz, I., Mohino, F. & Sastre, E. Selective synthesis of fatty monoglycerides by using functionalised mesoporous catalysts. *Appl. Catal. A* **254**, 173-188 (2003).

10. Hoo, P. & Abdullah, A. Z. Direct synthesis of mesoporous 12-tungstophosphoric acid SBA-15 catalyst for selective esterification of glycerol and lauric acid to monolaurate. *Chem. Eng. J.* **250**, 274-287 (2014).

11. Faustini, M. *et al*. Bottom-up approach toward titanosilicate mesoporous pillared planar nanochannels for nanofluidic applications. *Chem. Mater.* **22**, 5687-5694 (2010).

12. Eijkel, J. C. & Van Den Berg, A. Nanofluidics: what is it and what can we expect from it? *Microfluid Nanofluid.* **1**, 249-267 (2005).

13. Meziani, M. *et al*. Number and strength of surface acidic sites on porous aluminosilicates of the MCM-41 type inferred from a combined microcalorimetric and adsorption study. *Langmuir* **16**, 2262-2268 (2000).

14. Beck, J. *et al*. A new family of mesoporous molecular sieves prepared with liquid crystal templates. *J. Am. Chem. Soc.* **114**, 10834-10843 (1992).

15. Mokaya, R. & Jones, W. Acidity and catalytic activity of aluminosilicate mesoporous molecular sieves prepared using primary amines. *Chem. Commun.* 983-984 (1996).
16. Zheng, A., Liu, S. & Deng, F. Acidity characterization of heterogeneous catalysts by solid-state NMR spectroscopy using probe molecules. *Solid State Nucl. Magn. Reson.* **55**, 12-27 (2013).
17. Fu, Y., Ye, F., Sanders, W. G., Collinson, M. M. & Higgins, D. A. Single molecule spectroscopy studies of diffusion in mesoporous silica thin films. *J. Phys. Chem. B* **110**, 9164-9170 (2006).
18. Park, S. C., Ito, T. & Higgins, D. A. Dimensionality of Diffusion in Flow-Aligned Surfactant-Templated Mesoporous Silica: A Single Molecule Tracking Study of Pore Wall Permeability. *J. Phys. Chem. C* **119**, 26101-26110 (2015).
19. Mahurin, S., Dai, S. & Barnes, M. Probing the diffusion of a dilute dye solution in mesoporous glass with fluorescence correlation spectroscopy. *J. Phys. Chem. B* **107**, 13336-13340 (2003).
20. Zürner, A., Kirstein, J., Döblinger, M., Bräuchle, C. & Bein, T. Visualizing single-molecule diffusion in mesoporous materials. *Nature* **450**, 705-708 (2007).
21. Kirstein, J. *et al*. Exploration of nanostructured channel systems with single-molecule probes. *Nat. Mater.* **6**, 303-310 (2007).
22. Jung, C., Hellriegel, C., Michaelis, J. & Bräuchle, C. Single-Molecule Traffic in Mesoporous Materials: Translational, Orientational, and Spectral Dynamics. *Adv. Mater.* **19**, 956-960 (2007).
23. Jung, C. *et al*. Diffusion of oriented single molecules with switchable mobility in networks of long unidimensional nanochannels. *J. Am. Chem. Soc.* **130**, 1638-1648 (2008).
24. Kumarasinghe, R., Higgins, E. D., Ito, T. & Higgins, D. A. Spectroscopic and Polarization-Dependent Single-Molecule Tracking Reveal the One-Dimensional Diffusion Pathways in Surfactant-Templated Mesoporous Silica. *J. Phys. Chem. C* **120**, 715-723 (2015).
25. Ito, S. *et al*. Microscopic Structure and Mobility of Guest Molecules in Mesoporous Hybrid Organosilica: Evaluation with Single-Molecule Tracking. *J. Phys. Chem. C* **113**, 11884-11891 (2009).
26. Sun, X. Single molecule studies of acidity in heterogeneous catalysts. (2013).
27. Fu, Y., Collinson, M. M. & Higgins, D. A. Single-molecule spectroscopy studies of microenvironmental acidity in silicate thin films. *J. Am. Chem. Soc.* **126**, 13838-13844 (2004).
28. Venn, A. A. *et al*. Imaging intracellular pH in a reef coral and symbiotic anemone. *Proc. Natl. Acad. Sci. U. S. A.* **106**, 16574-16579 (2009).
29. House, C. Confocal ratio-imaging of intercellular pH in unfertilised mouse oocytes. *Zygote* **2**, 37-45 (1994).

30. Bassnett, S., Reinisch, L. & Beebe, D. C. Intracellular pH measurement using single excitation-dual emission fluorescence ratios. *Am. J. Physiol.* **258**, C171-8 (1990).
31. Mason, M. D., Ray, K., Grober, R. D., Pohlers, G. & Cameron, J. Single molecule acid-base kinetics and thermodynamics. *Phys. Rev. Lett.* **93**, 073004 (2004).
32. Mason, M. D., Ray, K., Pohlers, G., Cameron, J. F. & Grober, R. D. Probing the local pH of polymer photoresist films using a two-color single molecule nanoprobe. *J. Phys. Chem. B* **107**, 14219-14224 (2003).
33. Mai, J., Miller, H. & Hatch, A. V. Spatiotemporal mapping of concentration polarization induced pH changes at nanoconstrictions. *ACS Nano* **6**, 10206-10215 (2012).
34. Owen, C. S., Carango, P., Grammer, S., Bobyock, S. & Leeper, D. B. pH-dependent intracellular quenching of the indicator carboxy-SNARF-1. *J. Fluoresc.* **2**, 75-80 (1992).
35. Večeř, J., Holoubek, A. & Sigler, K. Fluorescence Behavior of the pH-Sensitive Probe Carboxy SNARF-1 in Suspension of Liposomes. *Photochem. Photobiol.* **74**, 8-13 (2001).
36. Srivastava, A. & Krishnamoorthy, G. Time-resolved fluorescence microscopy could correct for probe binding while estimating intracellular pH. *Anal. Biochem.* **249**, 140-146 (1997).
37. Zhao, D. *et al*. Continuous mesoporous silica films with highly ordered large pore structures. *Adv. Mater.* **10**, 1380-1385 (1998).
38. Giri, D., Hanks, C. N., Collinson, M. M. & Higgins, D. A. Single-molecule spectroscopic imaging studies of polarity gradients prepared by infusion-withdrawal dip-coating. *J. Phys. Chem. C* **118**, 6423-6432 (2014).
39. Han, J. & Burgess, K. Fluorescent indicators for intracellular pH. *Chem. Rev.* **110**, 2709-2728 (2009).

Chapter 4 - **Probing the local acidity of gradient aluminosilicate thin films with C-snarf-1 as the fluorescent indicator**

4.1 Introduction

Aluminosilicate materials are widely applied as solid acid catalysts in the petrochemical [1, 2] and biomass industries.[3] For instance, higher hydrocarbons could be cracked to smaller molecules with the assistance of aluminosilicate catalysts at higher temperature.[4, 5] Cellulose, which is abundant in biomass could also be hydrolyzed into glucose with mesoporous aluminosilicate materials as catalysts.[6 7-9]Aluminosilicate materials are also applied as catalysts in other reactions including dehydration,[10, 11] transesterification,[12] fast pyrolysis[13-15] and adol condensation.[16, 17]

The acidity of solid acid catalysts are determined both by the amount of acid sites and acid strength of these materials. Usually, two different kinds of acid sites, Lewis acid sites and Brønsted acid sites, exist on the surface of solid acid catalysts.[1, 2] In the case of aluminosilicate materials, the Brønsted acid sites are introduced via doping Al^{3+} into the SiO_2 lattice. Because Si^{4+} cations in the lattice are replaced by Al^{3+} cations, protons attached on the surface of the materials are necessary to maintain the charge balance. Thus, the concentration of Al^{3+} in the SiO_2 lattice plays a pivotal role in the acidity of aluminosilicate materials.[1, 2] As mentioned in Chapter 3, the acidity of aluminosilicate materials could be characterized via various ensemble average methods such as titration[18] and TPD.[19]

With C-snarf-1 as the fluorescent probe, the local acidity of the aluminosilicate film could be studied.[20, 21] In this chapter, aluminosilicate thin films incorporating gradients in alumina concentration are prepared and investigated. The gradient films are loaded with C-snarf-

1 dye molecules through spin coating. The emission ratio of C-snarf-1 dye molecules along the alumina concentration gradient is studied through single molecule methods. With an increase in alumina concentration along the gradient, the median value of emission decreases, which agrees with prior research.

4.2 Experimental section

4.2.1 Preparation of gradient films via a dip coating method

The silica and alumina sols were prepared according to a previous paper, with minor modifications.[20,22] The silica sol was prepared by mixing 1.193 g of tetramethyl orthosilicate (TMOS), 45.5 mL absolute ethanol, 1.85 mL water, 1.50 mL of 0.1 M HCl. The mixture was stirred at room temperature for 1 h. In the alumina sol preparation, 0.20 mL of EAA was first added to 0.32 g aluminum isopropoxide in ~ 7 mL of isopropanol and sonicated for 15 min followed with stirring at room temperature for 2 h until a translucent solution was achieved. After that, 150 μL of concentrated nitric acid was added dropwise to achieve a totally clear solution. More isopropanol was then added to bring the final sol volume to 10 mL. The mixture was further stirred at room temperature for 1 h. The molar concentrations of both the silica and alumina sols were 0.157 M.

Figure 4.1 is a schematic illustration of the dip coating apparatus. A glass cover slide is immersed in the silicate/alumina sol and then pulled out of the solution vertically at a certain rate. Before dip coating, 10 mL of the silica sol was added to the vessel as solution A. Solution B, which was a mixture of silica and alumina sols in a 1 to 4 ratio, was then pumped into the vessel at a rate of 1.4 mL/h when the dip coating process started. Meanwhile, another pump is utilized to pump the mixed solution out of the vessel at the same rate. A magnetic stirrer was employed to ensure the mixture of solutions during dip coating. The rate at which the glass slide

was pulled out of solution was 0.05 mm/s. The dip coated thin film was further calcined as described in chapter 3.

4.2.2 Instruments and methods

C-snarf-1dye molecules were loaded on the surface of each aluminosilicate gradient thin film by spin coating 0.3 nM dye solution onto the film at a speed of 2500 rpm. The SM measurement of emission ratio was carried out using the same apparatus and procedures described in chapter 3.

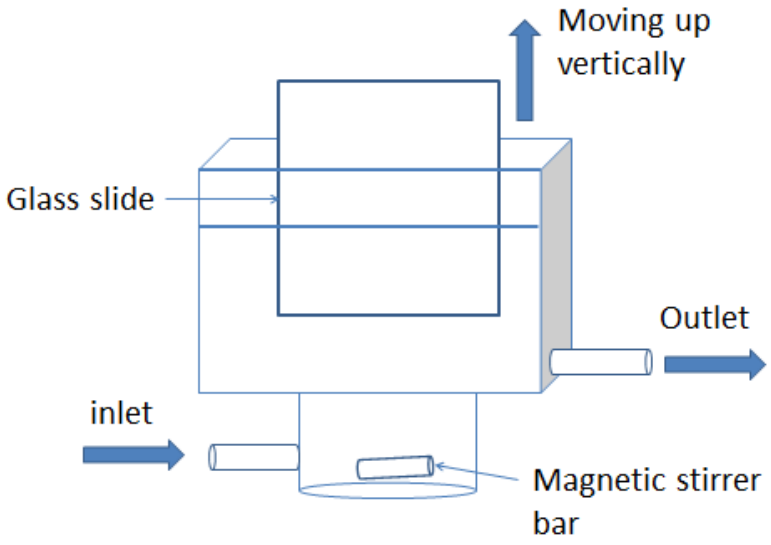

Figure 4.1 Schematic illustration of dip coating apparatus for aluminosilicate gradient film preparation.

4.3 Results and discussion

Figure 4.2 shows the stacked image of C-snarf-1 dye molecules collected at the 12 mm position along the gradient from the point dip coating started. The stacked images from the 640

nm and 580 nm channels are shown in Figure 4.2 a and b, respectively. The positions of the individual dye molecules are determined by the same method as in chapter 3. The trajectories obtained are displayed in Figure 4.2 c.

From both the stacked images and trajectories, it can be concluded that the molecules deposited on the surface of the aluminosilicate gradient films are immobile. Thus, only emission ratios of every single molecule are applied as an indicator of the acidity of the aluminosilicate film at each measured position. Again, note that the single molecule emission ratios are calculated by averaging the emission ratio of each dye molecule across its entire trajectory. The lack of an aqueous phase on the surface of the aluminosilicate gradient film may explain the immobility of dye molecules.

During the dip coating process, as the glass cover slide was withdrawn out of the sol solution, silicate or alumina/silicate mixed sol will dry and deposit on the surface of the glass cover slide to form a continuous film. The position where the dip coating film started is denoted as 0 mm. Since there is no alumina sol in the solution when the film is first deposited at 0 mm, the Al/Si ratio should be 0 at this position. As the length of the dip coating film rose, the Al/Si ratio of mixed sol increased. Consequently, the local Al/Si ratio increased as the slide was pulled out of the sol (i.e., down the gradient). The blue solid line in Figure 4.4 plots the calculated Al/Si molar ratio in the dip coating solution with respect to position along the film, assuming ideal mixing. For a dip coating rate of 0.05 mm/s, the local Al/Si ratio varies from 0, where the film started, to 0.116, at positions 15 mm away. The equation for the calculation of the Al/Si ratio is given below;

$$\frac{dC_{Al}}{dl} = \frac{\upsilon_0}{V \times u}(C_{Al0} - C_{Al}) \tag{4.1}$$

$$R_{Al/Si} = \frac{C_{Al}}{C_t - C_{Al}} \tag{4.2}$$

where C_{Al0} is the concentration of the alumina sol in solution B, C_{Al} is the concentration of the alumina sol in the vessel, l is the length of the dip coated film, υ_0 is the volumetric speed of feed pumped into the vessel, which is 1.46 ml/min, V is the volume of solution in the vessel, which is 10 ml, C_t is the total concentration of alumina and silica sol. $R_{Al/Si}$ is the estimated Al/Si molar ratio.

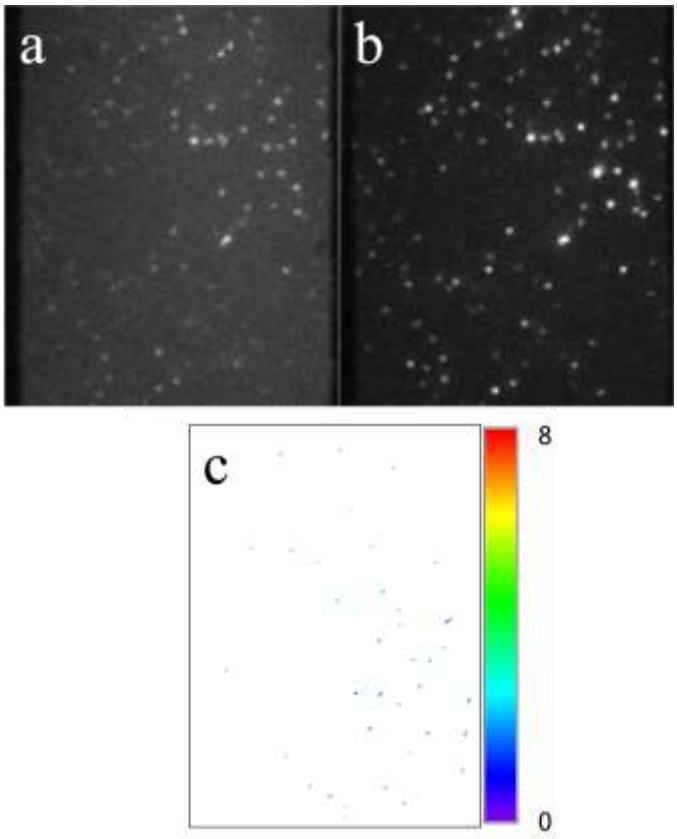

Figure 4.2(a,b) Z-projection images of C-snarf-1 dye molecules in mesoporous silica thin films for the 640 and 580 nm detection channels. The video is taken at a position 12 mm along the gradient. The dip coating speed is 0.05 mm/s. (c) Single molecule trajectories obtained from the same videos. The emission ratio I_{580}/I_{640} of C-snarf-1 dye molecules are reflected via the color of the trajectory.

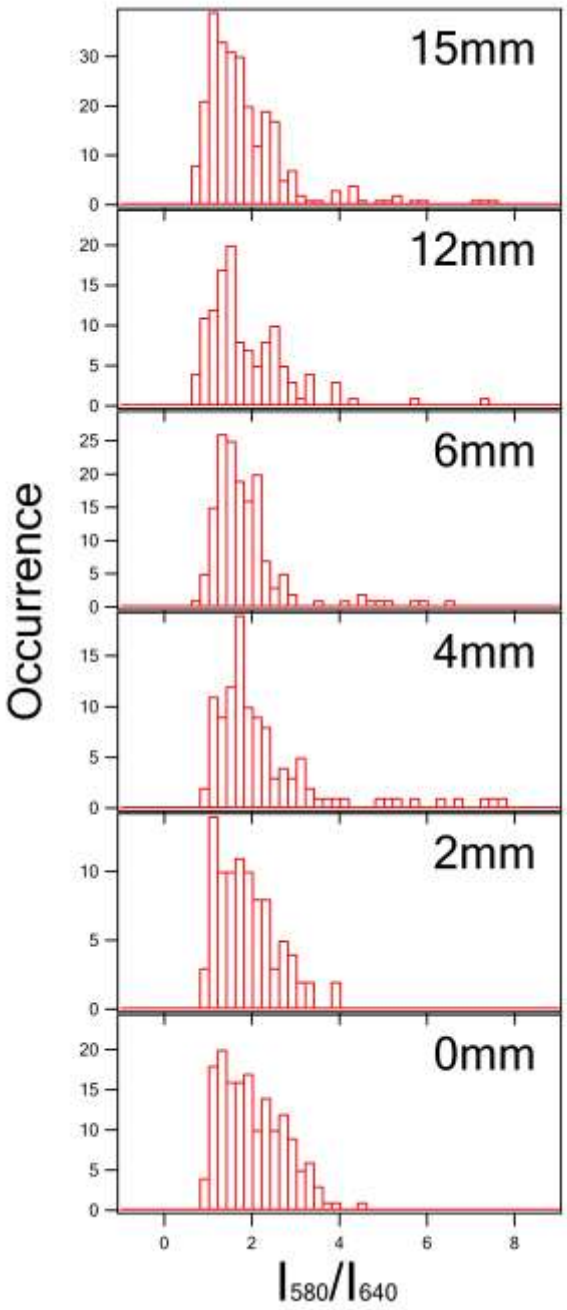

Figure 4.3 SM emission ratio (I_{580}/I_{640}) histograms for C-snarf-1 on the surface of an aluminosilicate thin film at different positions along the dip coated gradient. The dip coating speed was 0.05 mm/s.

Histograms showing the emission ratio from C-snarf-1 dye molecules measured at different position along the Al/Si gradient are exhibited in Figure 4.3. The broad variation of

emission ratios between different molecules at different position is indicative of microscale heterogeneity in the acidity of the aluminosilicate thin film. The average and median emission ratios of C-snarf-1 dye molecules excited at different spots along the gradient are plotted in Figure 4.4. Note that molecules with very large emission ratios will show significant impact on the average emission ratio but less impact on the median emission ratio. Note that the average emission ratio at 4 mm does not follow the trend noted for the other positions (i.e. a decreasing trend in emission ratio with position). This is due to several molecules with very large emission ratios that significantly increase the calculated average. As seen in Figure 4.4, the median emission ratio for this position is more in line with the values for other positions.

The decrease in emission ratio with the increase in Al concentration is similar to the trend observed in our previous work on disordered mesoporous aluminosilicate films.[20] The emission ratio from C-snarf-1 dye molecules in bulk aqueous solutions of different pH showed that the protonation of the carboxyl groups of C-snarf-1 dye molecules at low pH may induce the decrease in emission ratio (Figure 3.5).[20] Thus, the decrease in emission ratio with the increase in Al/Si ratio along the gradient could be ascribe to a rise in acidity with the increase in Al/Si ratio.

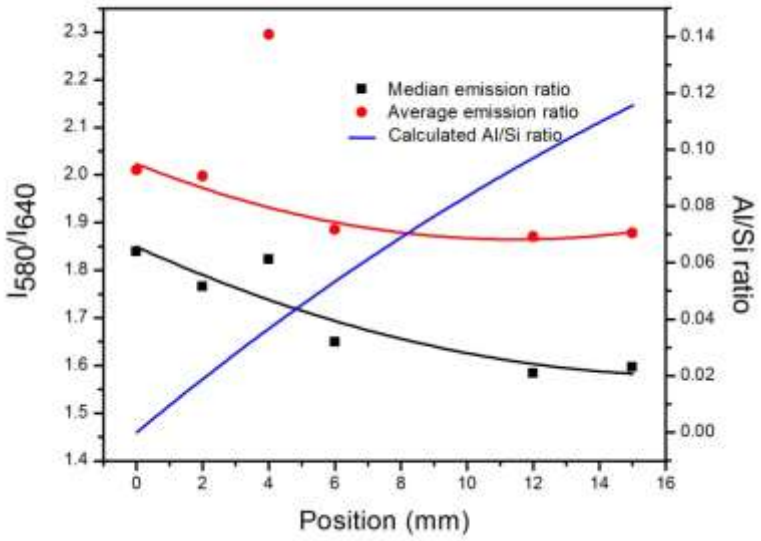

Figure 4.4(▪,•) Median and average emission ratio of C-snarf-1 fluorescent dye molecules measured at different position along the Aluminosilicate gradient film; (-) calculated Al/Si ratio versus the length of dip coating film along gradient. The dip coating rate is 0.05 mm/s.

4.4 Conclusion

Aluminosilicate gradient thin films with varying Al/Si ratios were prepared via a dip coating method. The impact of Al/Si on the acidity of the film was analyzed with C-snarf-1 dye molecules as a fluorescent indicator. The microscale heterogeneity in acidity of the thin films was reflected by the broad distribution of emission ratios observed from the dye molecules. The decrease in average and median emission ratios along the gradient with the rise of Al/Si ratio indicates that the acidity of aluminosilicate thin film increases with the increase in Al/Si ratio.

References

1. Hattori, H. & Ono, Y. in *Solid Acid Catalysis: From Fundamentals to Applications* (CRC Press, 2015).

2. Tanabe, K., Misono, M., Hattori, H. & Ono, Y. in *New solid acids and bases: their catalytic properties* (Elsevier, 1990).

3. Chen, Y., Ostafin, A. & Mizukami, H. Synthesis and characterization of pH sensitive carboxySNARF-1 nanoreactors. *Nanotechnology* **21**, 215503 (2010).

4. Nace, D. M. Catalytic cracking over crystalline aluminosilicates. I. Instantaneous rate measurements for hexadecane cracking. *Ind. Eng. Chem. Prod. Res. Dev.* **8**, 24-31 (1969).

5. Nace, D. M. Catalytic cracking over crystalline aluminosilicates. microreactor study of gas oil cracking. *Ind.Eng. Chem. Prod. Res. Dev.* **9**, 203-209 (1970).

6. Lai, D. *et al*. Hydrolysis of cellulose into glucose by magnetic solid acid. *ChemSusChem* **4**, 55-58 (2011).

7. Lai, D. *et al*. Hydrolysis of cellulose into glucose by magnetic solid acid. *ChemSusChem* **4**, 55-58 (2011).

8. Rinaldi, R., Palkovits, R. & Schüth, F. Depolymerization of cellulose using solid catalysts in ionic liquids. *Angew. Chem. Int. Ed.* **47**, 8047-8050 (2008).

9. Huang, Y. & Fu, Y. Hydrolysis of cellulose to glucose by solid acid catalysts. *Green Chem.* **15**, 1095-1111 (2013).

10. Ichikawa, N., Sato, S., Takahashi, R. & Sodesawa, T. Catalytic reaction of 1, 3-butanediol over solid acids. *J. Mol. Catal. A: Chem.* **256**, 106-112 (2006).

11. Zhang, W., Yu, D., Ji, X. & Huang, H. Efficient dehydration of bio-based 2, 3-butanediol to butanone over boric acid modified HZSM-5 zeolites. *Green Chem.* **14**, 3441-3450 (2012).

12. Leung, D. Y., Wu, X. & Leung, M. A review on biodiesel production using catalyzed transesterification. *Appl. Energy* **87**, 1083-1095 (2010).

13. Adjaye, J. & Bakhshi, N. Production of hydrocarbons by catalytic upgrading of a fast pyrolysis bio-oil. Part II: Comparative catalyst performance and reaction pathways. *Fuel Process Technol* **45**, 185-202 (1995).

14. Adjaye, J. D. & Bakhshi, N. Production of hydrocarbons by catalytic upgrading of a fast pyrolysis bio-oil. Part I: Conversion over various catalysts. *Fuel Process Technol* **45**, 161-183 (1995).

15. Custodis, V. B., Karakoulia, S. A., Triantafyllidis, K. S. & van Bokhoven, J. A. Catalytic Fast Pyrolysis of Lignin over High-Surface-Area Mesoporous Aluminosilicates: Effect of Porosity and Acidity. *ChemSusChem* **9**, 1134-1145 (2016).

16. Inegbenebor, A. I., Mordi, R. C. & Ogunwole, O. M. Zeolite Catalyzed Aldol Condensation Reactions. *Int. J. Appl. Sci. Biotechnol.* **3**, 1-8 (2015).

17. Hu, J. *et al*. Aldol condensation of acetic acid with formaldehyde to acrylic acid over SiO 2-, SBA-15-, and HZSM-5-supported VPO catalysts. *J. Ind. Eng. Chem.**40**, 145-151* (2016).

18. Ikenberry, M. *et al*. Acid monolayer functionalized iron oxide nanoparticles as catalysts for carbohydrate hydrolysis. *Green Chem.* **16**, 836-843 (2014).

19. Mardkhe, M. K. *et al*. Acid site properties of thermally stable, silica-doped alumina as a function of silica/alumina ratio and calcination temperature. *Appl. Catal. A* **482**, 16-23 (2014).

20. Sun, X. Single molecule studies of acidity in heterogeneous catalysts. (2013).

21. Fu, Y., Collinson, M. M. & Higgins, D. A. Single-molecule spectroscopy studies of microenvironmental acidity in silicate thin films. *J. Am. Chem. Soc.* **126**, 13838-13844 (2004).

22. Sun, X. *et al*. Single-Molecule Studies of Acidity Distributions in Mesoporous Aluminosilicate Thin Films. *Langmuir* **31**, 5667–5675(2015).

Chapter 5 - **Conclusion and future work**

5.1 Conclusion

(1) In the hydrogen production from heavy hydrocarbon work, we investigated the autothermal reforming (ATR) and partial oxidation (POX) of hexadecane by Pt/Ni bimetallic nanoparticles loaded on three different ceria- based supports including cerium oxide, gadolinium-doped cerium oxide and cerium-doped zirconium oxide. The Pt/Ni molar ratios for nanocatalyst particles ranged from 0 to 10/90. Instead of preparing Pt/Ni catalysts by successive loading of the catalyst with Pt and Ni, in this work, bimetallic Pt/Ni nanoparticles were first prepared and then loaded on the support. Thus, intimate contact of Pt and Ni was assured, and it is thought that the ratio of Pt to Ni in individual particles can be better controlled.

Strong interaction between Ni and CeO_2-ZrO_2 could be revealed by TPR and XPS analysis. Slightly doping Ni-CeO_2-ZrO_2 with Pt in our experiments greatly enhanced the reducibility of catalysts as well as catalytic performance during ATR or POX experiments. The promotion effect of CeO_2 in Pt/Ni CeO_2 catalysts for ATR or POX was limited because both Pt and Ni did not show a strong interaction with CeO_2. For bimetallic catalysts loaded on the Gd_2O_3-CeO_2 support, although Pt showed a strong interaction with the Gd_2O_3-CeO_2 support, no significant improvement of catalytic activity was achieved until Pt/Ni ratio reached 10/90.

(2) The local acidity of the surface of a gradient aluminosilicate thin film and the pore structure of silicate mesoporous film was explored by using C-snarf-1 as a fluorescent probe. The emission ratio of the 580 nm and 640 nm channels from the same C-snarf-1 molecule was

applied as an indicator for local pH value. In the case of the gradient aluminosilicate thin film, the local pH was measured in a dry state. A similar result as our previous work on aluminosilicate porous film was observed. Both the average and median emission ratios decrease with the rise of Al/Si ratio. The heterogeneity of acidity on the surface of gradient film was reflected by the broad distribution of emission ratio in the micrometer scale.

A microfluidic device was designed that allowed diffusion of fluorescent dye molecules only through the pores of a mesoporous silicate film in order to allow the acidity within the pores to be studied. A much wider distribution and higher average emission ratio was measured as compared to previous work or to the gradient aluminosilicate film experiments. The average emission ratio increased with the increasing pH value until pH 6 to 7. Further increase of pH to a basic environment led to a decline in the average emission ratio. Mobile and immobile molecules displayed differences in both averages and standard deviations of the C-snarf-1 dye molecule emission ratio, which indicated that interactions between pore walls and C-snarf-1 affected the emission ratio. The interaction between dye molecules and pore surface may decrease as the ionic strength increases. The suppression of the emission ratio of mobile molecules could then be achieved via increasing ionic strength of aqueous solution.

5.2 Future Work

(1) Sulfur, which is inherently contained in commercial fuels, decreases the activity of catalysts in ATR and POX severely. The field application of ATR or POX for hydrogen production from commercial fuels requires sulfur tolerant catalysts. Further study on the sulfur resistance of bimetallic catalysts loaded on ceria based supports is of significance for the real application of these catalysts.

(2) The emission ratio of C-snarf-1 probes on the gradient film and in the pores of silicate mesoporous film shows significant difference. The difference in emission ratio is possibly induced by the difference in the structure of silicate film or by whether water is present during measurement. If the local acidity study of gradient film can be carried out at different relative moisture, then the impact of water on the behavior of C-snarf-1 dye molecules or the silicate structure will be revealed. Furthermore, for catalysis application, modified SBA-15 structure with higher acidity could be prepared. Studying the local acidity in the pore structure of modified SBA-15 structure may offer helpful information for the application of these materials as catalysts. In addition, on one hand, mesoporous or microporous silicate structure plays an important role as acid catalysis; on the other, current dual emission fluorescent pH indicator such as C-snarf-1 can only diffuse into the structures with relatively larger pore sizes. In this case, it is promising to apply fluorescent molecules with smaller size into much smaller mesoporous structure. Both dual emission fluorescent pH indicator such as Coumarin 6, LysoSensor Yellow/Blue DND-160 and nondual emission fluorescent pH indicator such as 4-PYMPO combined with fluorescence correlation spectroscopy method(FCS) show potential value for the exploration of local acidity in much smaller pore structures.

Appendix A - Supplementary data for chapter 2

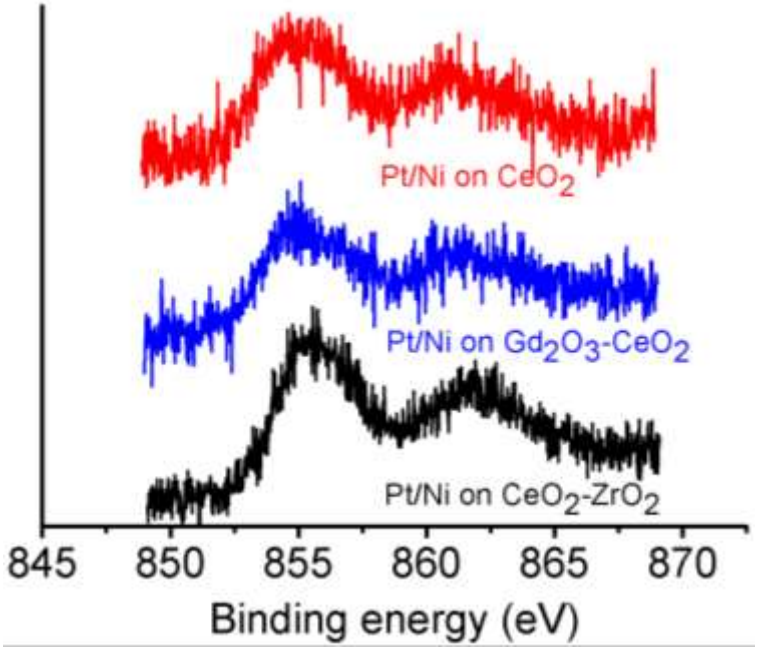

Figure A.1 The Ni2p3/2 core spectra of Pt/Ni 10/90 on different ceria based support after calcination in air for 5 h at 600 ^{o}C.

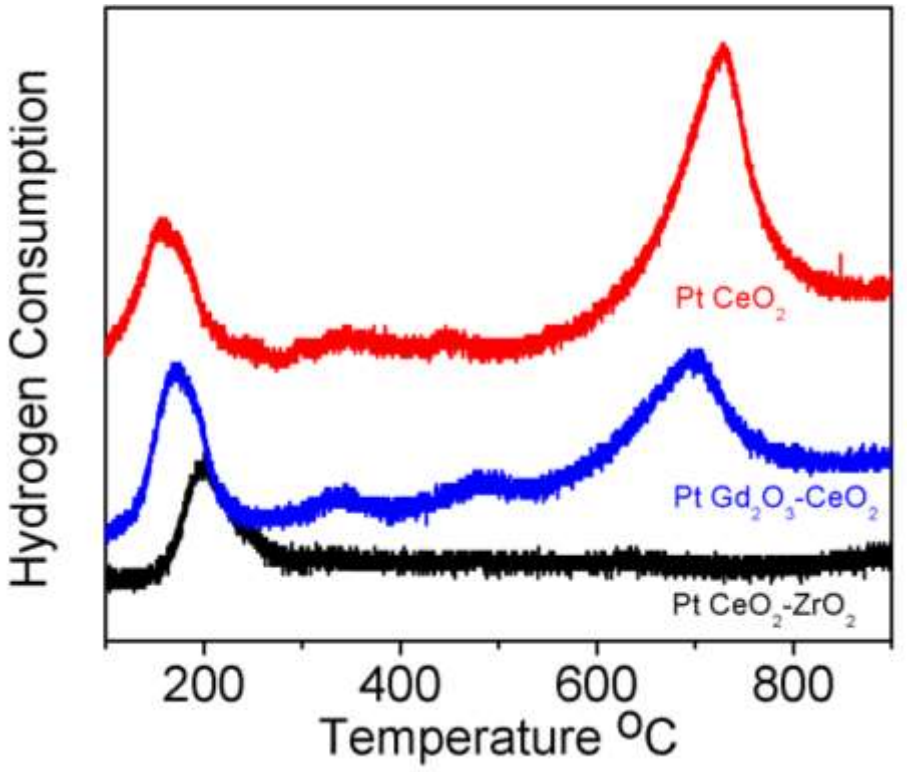

Figure A.2 TPR profiles of Pt nanoparticle catalysts loaded on various ceria based supports treated at 850 ^{o}C in air for 24 h.

Figure A2 shows the TPR profiles of Pt catalysts loaded on various ceria based supports treated at 850 ^{o}C in air for 24 h. The purpose of heat treatment is to mimic the sintering process during reaction. As showed in Figure A2, the reduction peak of surface ceria shifts to a much lower temperature comparing to the Pt nanoparticles loaded ceria based supports without heat treatment. The Pt catalyzed reduction peaks of surface ceria are 160 ^{o}C for CeO_2 supports, 171 ^{o}C for Gd_2O_3-CeO_2 supports and 200 ^{o}C for CeO_2-ZrO_2 supports. The decreasing of reduction temperature of surface ceria may induced by the migration of Pt onto ceria based supports due to sintering during the heat treatment.

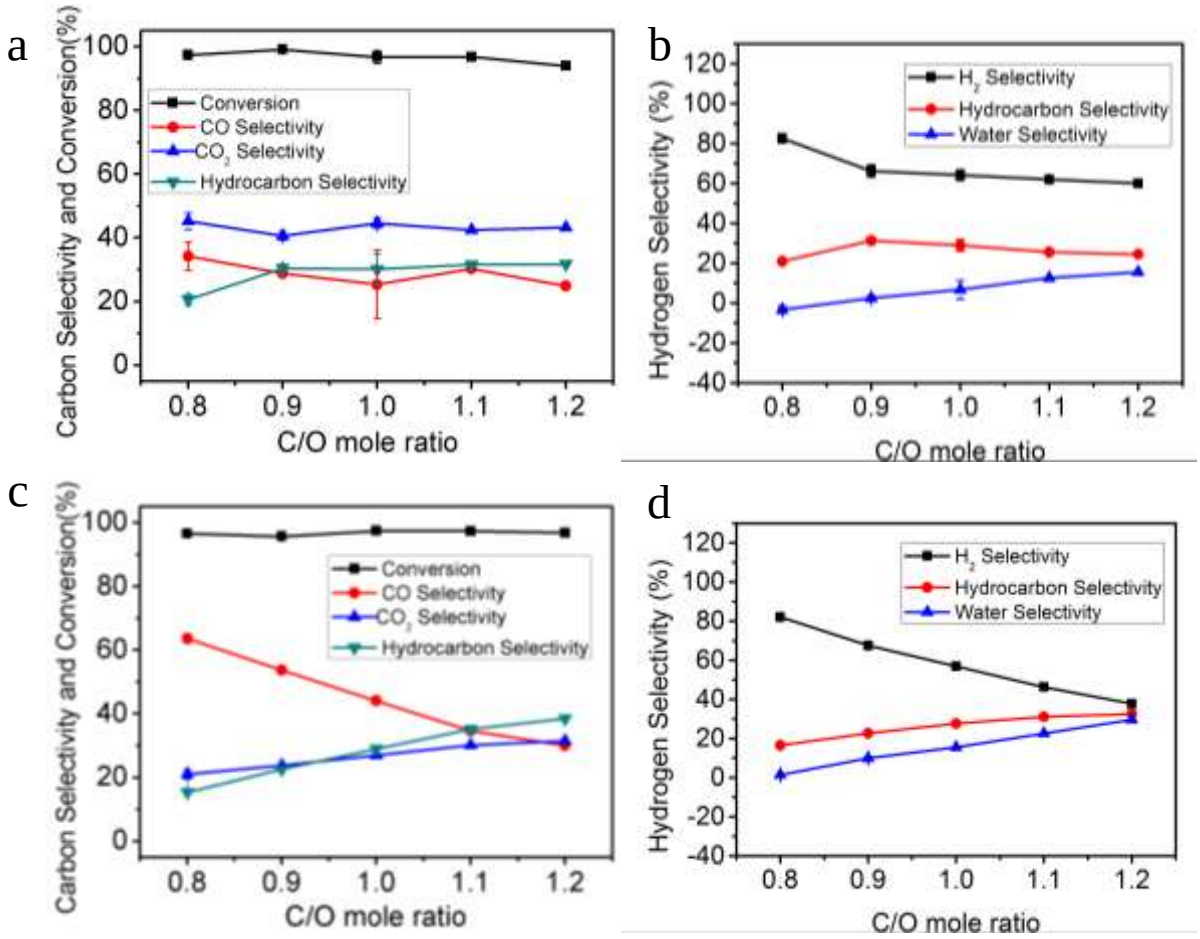

Figure A.3 Impact of C/O molar ratio on the ATR and POX process of n-hexadecane (Ni CeO_2). (a) Carbon conversion and selectivity for ATR, (b) Hydrogen selectivity for ATR, (c) Carbon conversion and selectivity for POX, (d) Hydrogen selectivity for POX.

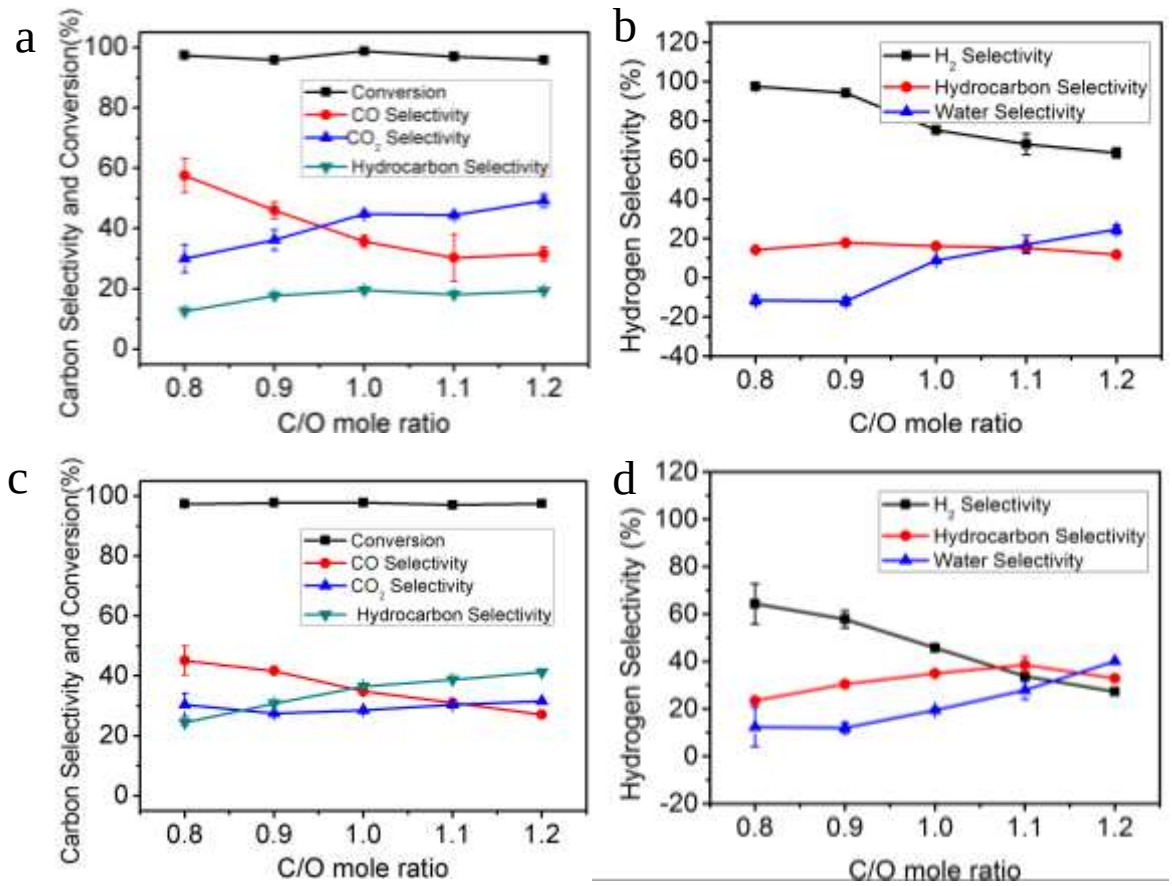

Figure A.4 Impact of C/O molar ratio on the ATR and POX process of n-hexadecane (Ni-CeO_2-ZrO_2). (a) Carbon conversion and selectivity for ATR, (b) Hydrogen selectivity for ATR, (c) Carbon conversion and selectivity for POX, (d) Hydrogen selectivity for POX.

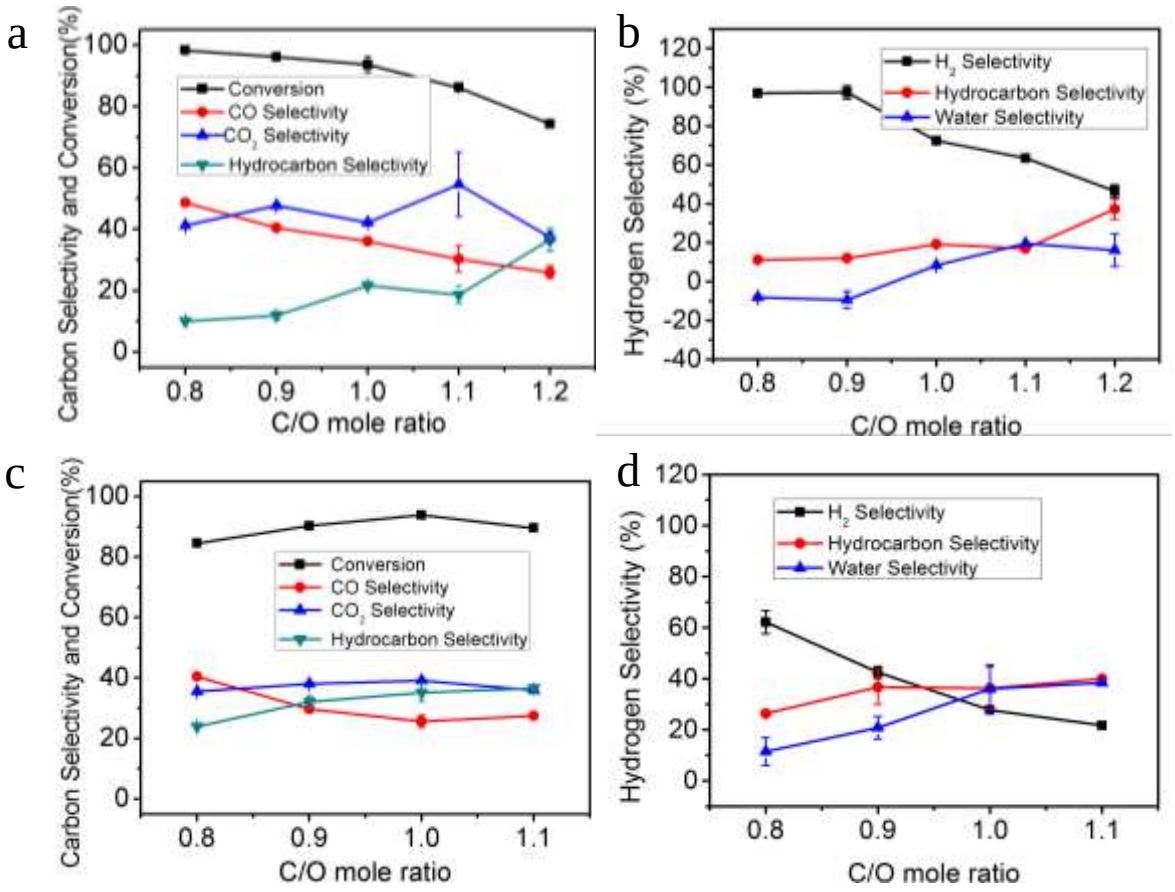

Figure A.5 Impact of C/O molar ratio on the ATR and POX process of n-hexadecane (Ni-Gd_2O_3-CeO_2). (a) Carbon conversion and selectivity for ATR, (b) Hydrogen selectivity for ATR, (c) Carbon conversion and selectivity for POX, (d) Hydrogen selectivity for POX.

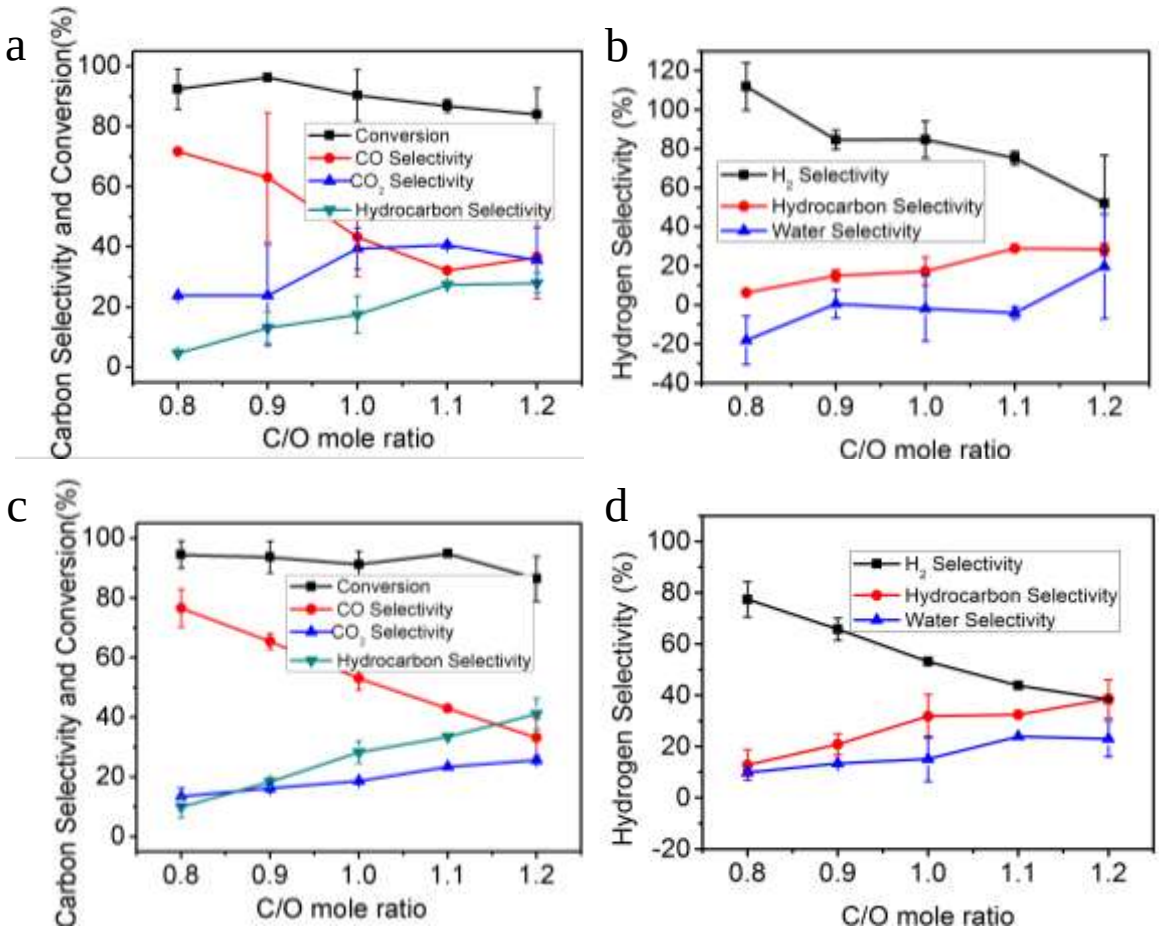

Figure A.6 Impact of C/O molar ratio on the ATR and POX process of n-hexadecane (Pt/Ni 3/97 CeO_2). (a) Carbon conversion and selectivity for ATR, (b) Hydrogen selectivity for ATR, (c) Carbon conversion and selectivity for POX, (d) Hydrogen selectivity for POX.

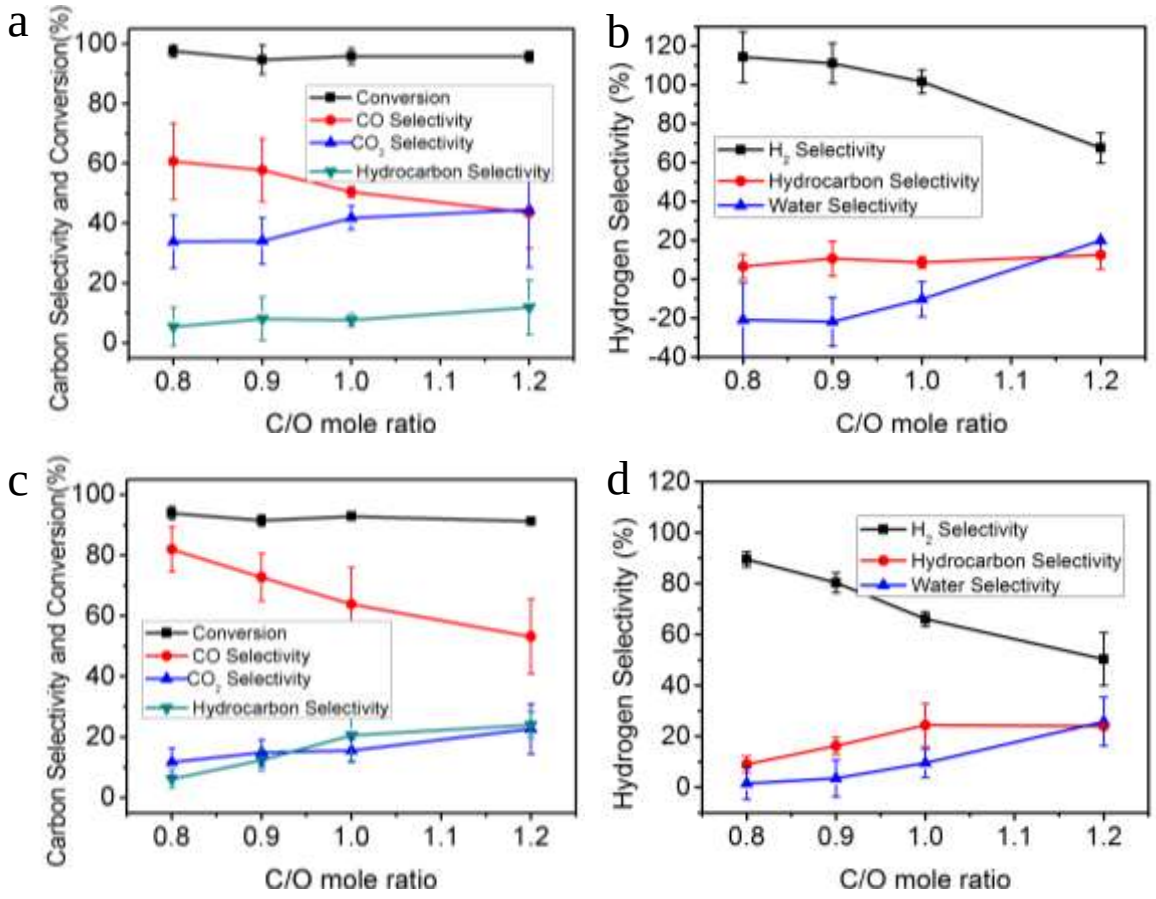

Figure A.7 Impact of C/O molar ratio on the ATR and POX process of n-hexadecane (Pt/Ni 3/97 CeO_2-ZrO_2). (a) Carbon conversion and selectivity for ATR, (b) Hydrogen selectivity for ATR, (c) Carbon conversion and selectivity for POX, (d) Hydrogen selectivity for POX.

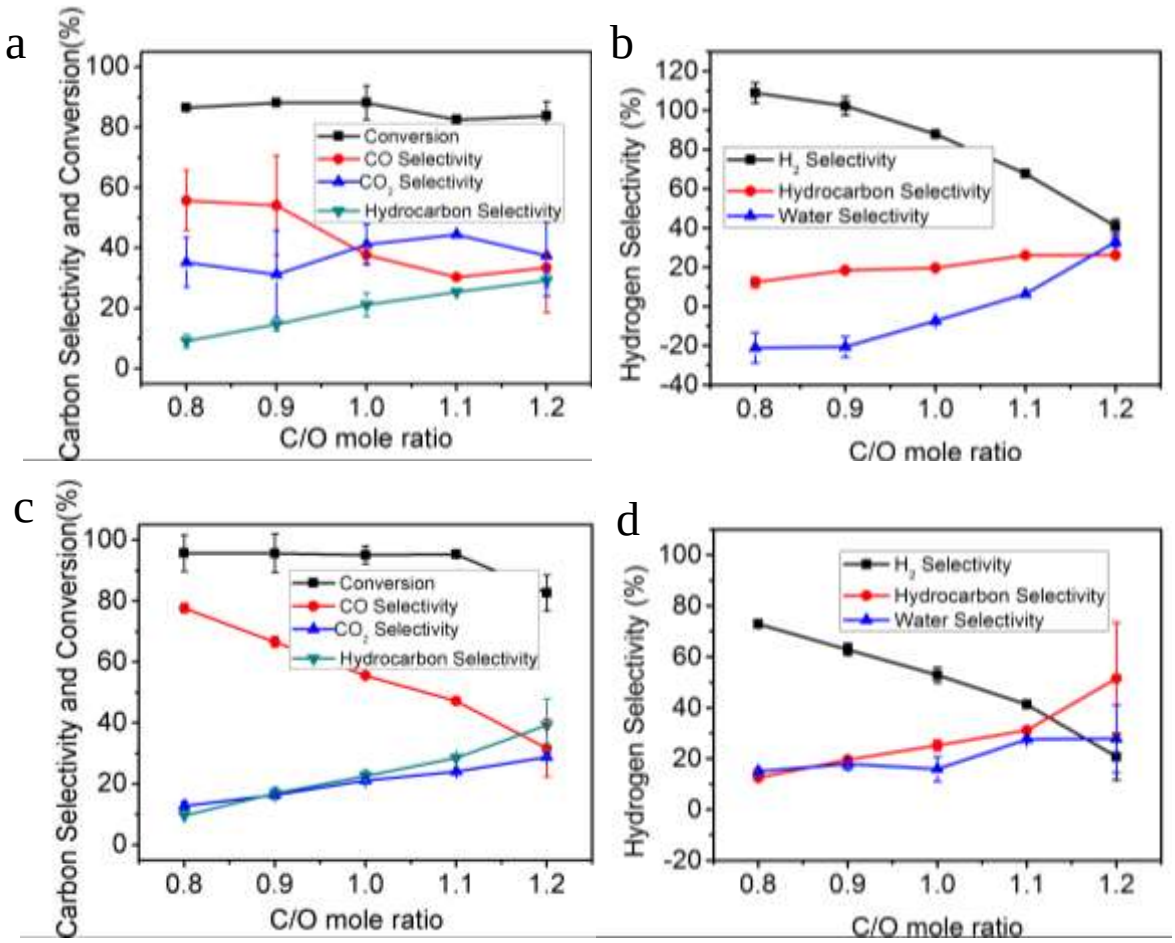

Figure A.8 Impact of C/O molar ratio on the ATR and POX process of n-hexadecane (Pt/Ni 3/97 Gd_2O_3-CeO_2). (a) Carbon conversion and selectivity for ATR, (b) Hydrogen selectivity for ATR, (c) Carbon conversion and selectivity for POX, (d) Hydrogen selectivity for POX.

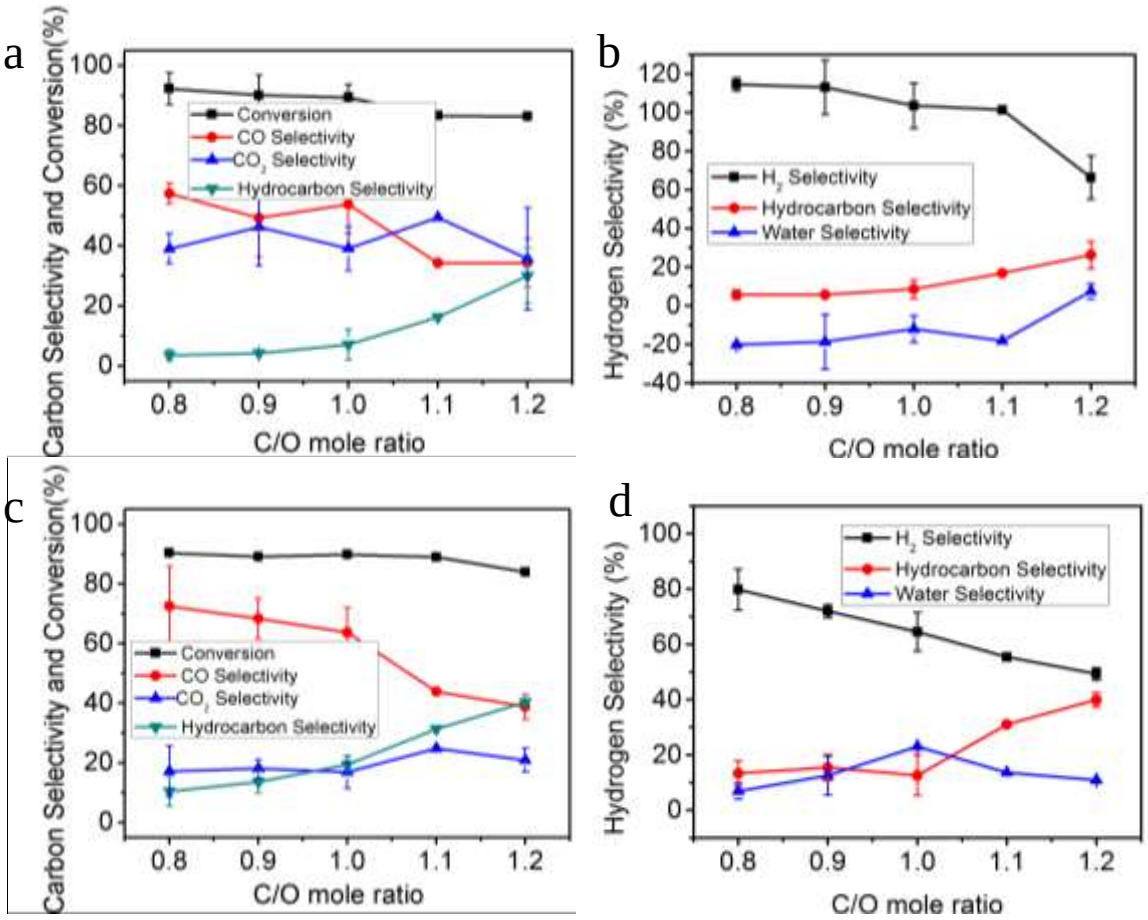

Figure A.9 Impact of C/O molar ratio on the ATR and POX process of n-hexadecane (Pt/Ni 10/90 CeO_2). (a) Carbon conversion and selectivity for ATR, (b) Hydrogen selectivity for ATR, (c) Carbon conversion and selectivity for POX, (d) Hydrogen selectivity for POX.

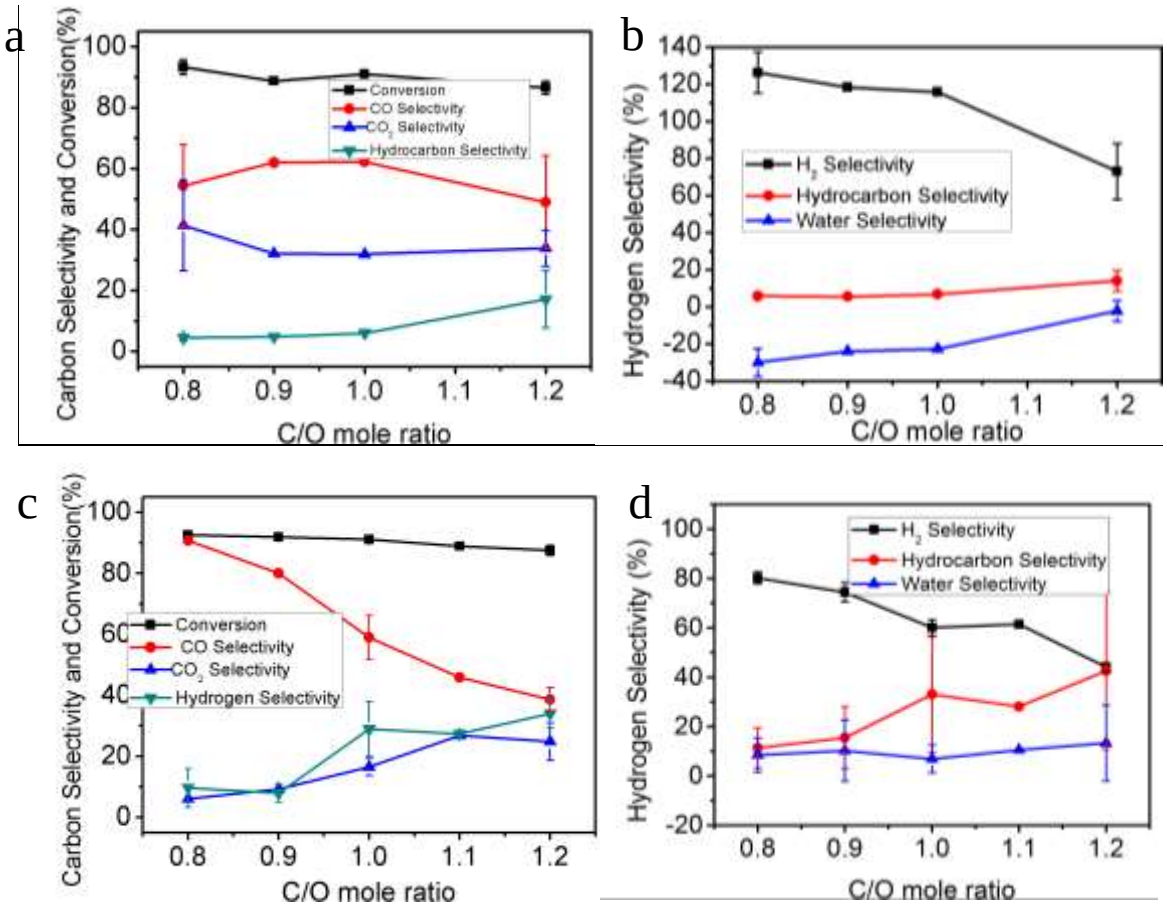

Figure A.10 Impact of C/O molar ratio on the ATR and POX process of n-hexadecane (Pt/Ni 10/90 CeO_2-ZrO_2). (a) Carbon conversion and selectivity for ATR, (b) Hydrogen selectivity for ATR, (c) Carbon conversion and selectivity for POX, (d) Hydrogen selectivity for POX.

The comparison of bed temperature during reaction for different catalysts

As shown in figure 2.1, bed temperatures were measured by a thermocouple placed at the bottom of catalyst bed. On one hand, POX reaction is known as a highly exothermic reaction; on the other hand, ATR is a combination of POX and SR, while SR is a high endothermic reaction. Consequently, the bed temperature of ATR should be less than that of POX. However, the reaction rate of POX is faster than that of SR. For POX, oxygen may completely consume at the very beginning of catalyst bed, where a hot spot is formed. In contrast, for ATR, the addition of

steam may inhibit the hot spot formation and lead to higher temperature at the bottom of catalysts bed.

Figure A11 plots the bed temperature of ATR and POX for all pure Ni and Pt/Ni bimetallic catalysts on ceria based supports. The bed temperature of POX is slightly less than that of ATR, possibly because of inhibition of hot spot formation for ATR.

In the case of ATR, with increasing platinum concentration, the bed temperature generally decreases for ceria and Gd_2O_3-ZrO_2 support. The possible explanation for this phenomenon is that SR reaction is enhanced as the platinum concentration increased so that more heat generated during POX is consumed. ATR by catalysts loaded on CeO_2-ZrO_2 supports shows lower bed temperature than that by catalysts loaded on other supports (Figure A11 a). Considering the higher hydrogen yield of ATR reaction by catalysts loaded on CeO_2-ZrO_2 supports, the lower bed temperature may indicate higher catalytic activity of catalysts on CeO_2-ZrO_2 supports for SR.

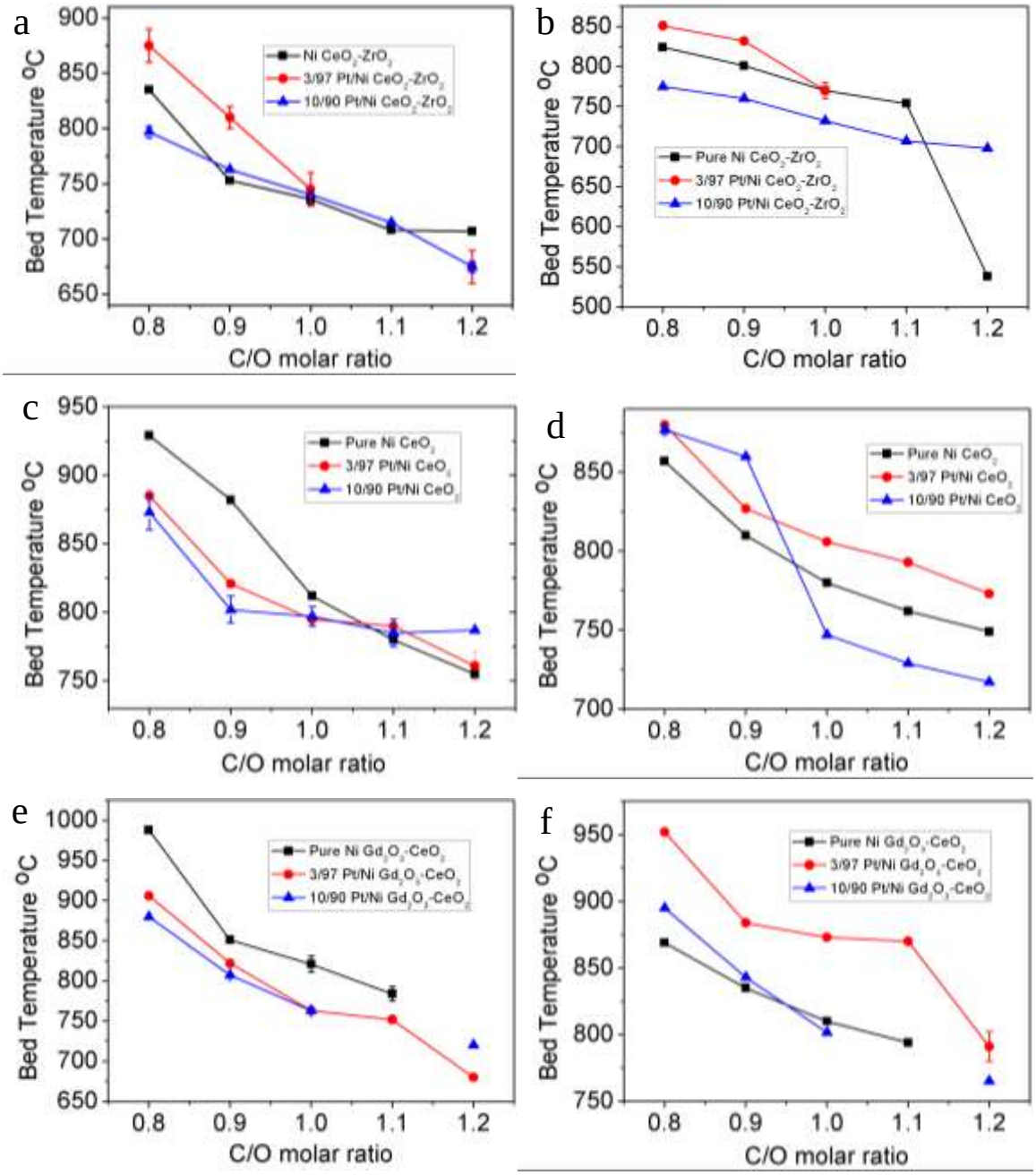

Figure A.11 Bed temperature of ATR and POX by pure Ni and Pt/Ni bimetallic catalysts loaded on ceria based supports: (a) ATR by pure Ni and Pt/Ni bimetallic catalysts on CeO_2-ZrO_2, (b) POX by pure Ni and Pt/Ni bimetallic catalysts on CeO_2-ZrO_2, (c) ATR by pure Ni and Pt/Ni bimetallic catalysts on CeO_2, (d) POX by pure Ni and Pt/Ni bimetallic catalysts on CeO_2, (e) ATR by pure Ni and Pt/Ni bimetallic catalysts on Gd_2O_3-CeO_2, (f) POX by pure Ni and Pt/Ni bimetallic catalysts on Gd_2O_3-CeO_2.

Appendix B - Supplementary data for chapter 3

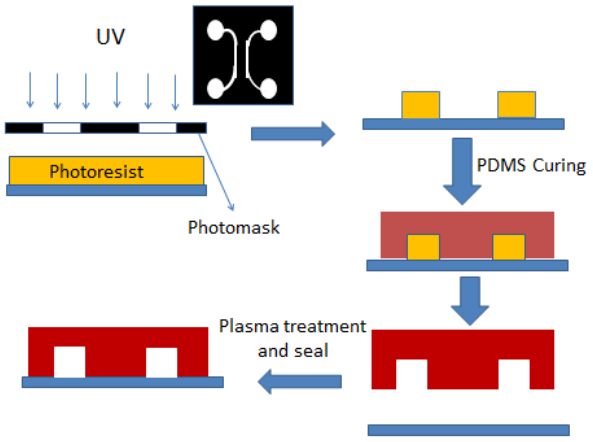

Figure B.1 Schematic illustration of the fabrication of microfluidic device for single molecule spectroscopy study.

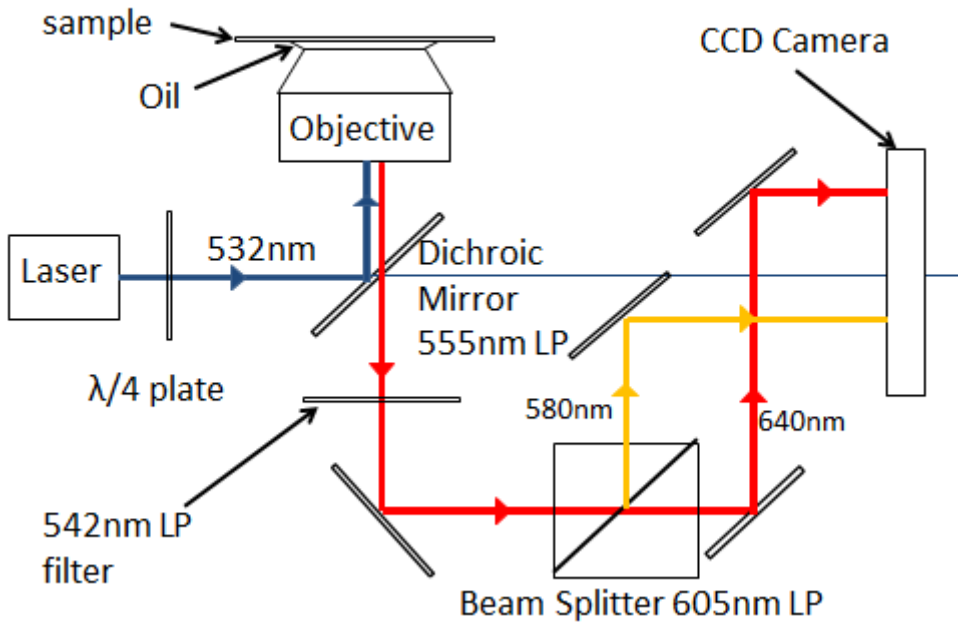

Figure B.2 Schematic illustration of the single molecule spectroscopy.

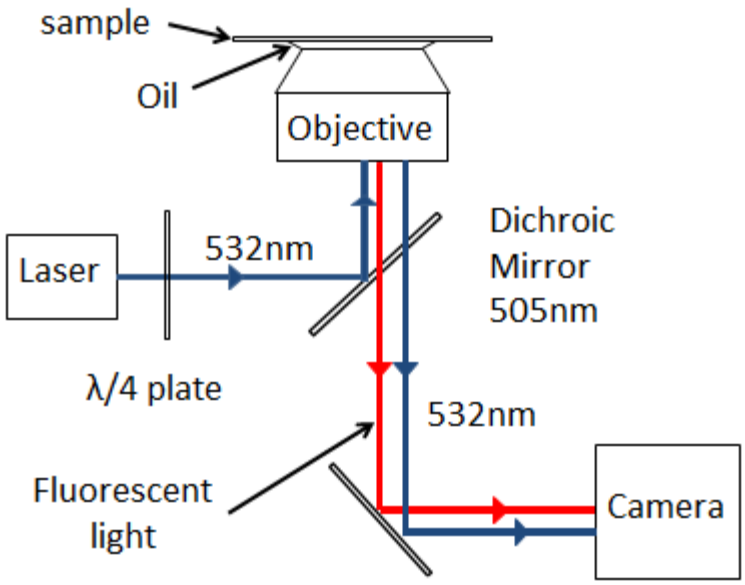

Figure B.3 Schematic illustration of the instrument for the estimation of illuminated position.

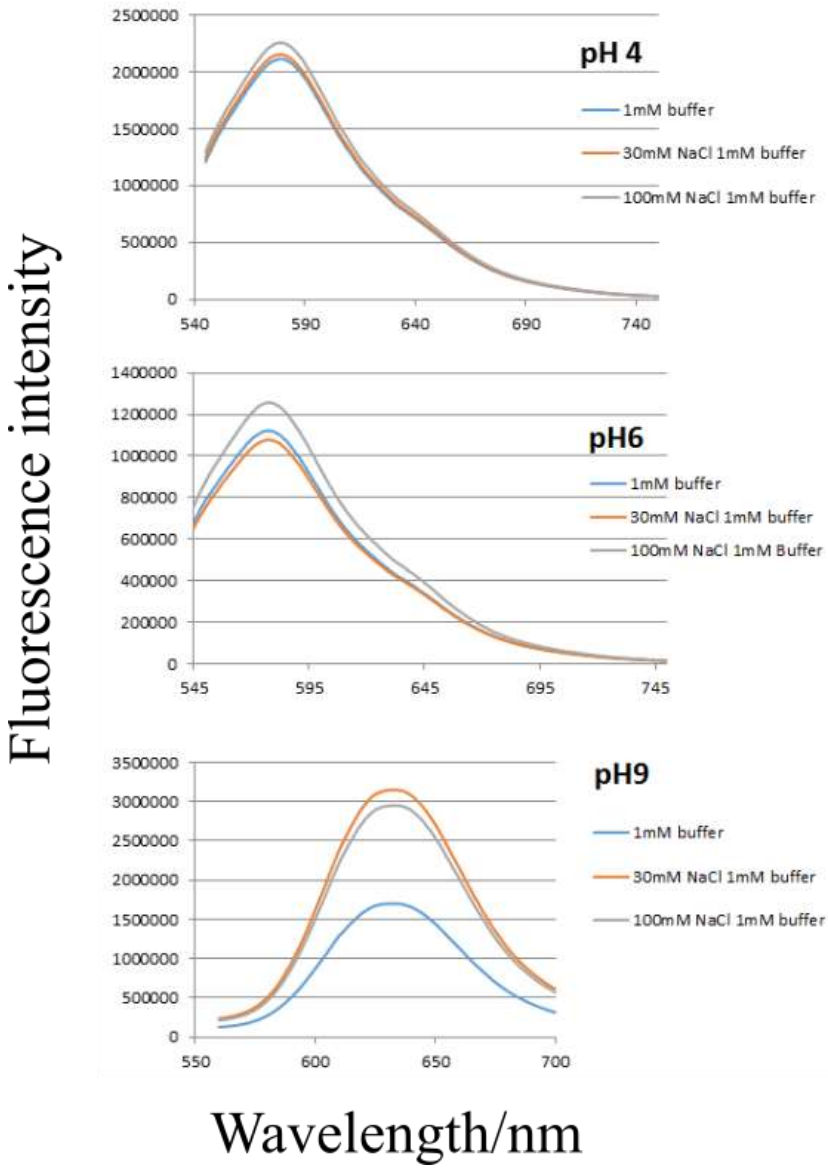

Figure B.4 C-snarf-1 emission ration in aqueous buffer solution as a function of pH and NaCl concentration.